DESIGN AND IMPLEMENTATION OF AN ANNULAR ACOUSTIC
LEVITATION SYSTEM

A THESIS SUBMITTED TO
THE GRADUATE SCHOOL OF NATURAL AND APPLIED SCIENCES
OF
MIDDLE EAST TECHNICAL UNIVERSITY

BY

MEHMET HAKAN KANDEMİR

IN PARTIAL FULFILLMENT OF THE REQUIREMENTS
FOR
THE DEGREE OF MASTER OF SCIENCE
IN
MECHANICAL ENGINEERING

AUGUST 2014

Approval of the thesis:

**DESIGN AND IMPLEMENTATION OF AN ANNULAR ACOUSTIC
LEVITATION SYSTEM**

submitted by **MEHMET HAKAN KANDEMİR** in partial fulfillment of the
requirements for the degree of **Master of Science in Mechanical Engineering
Department, Middle East Technical University** by,

Prof. Dr. Canan Özgen
Dean, Graduate School of **Natural and Applied Sciences**   _____

Prof. Dr. Süha Oral
Head of the Department, **Mechanical Engineering**   _____

Prof. Dr. Mehmet Çalışkan
Supervisor, **Mechanical Engineering Dept., METU**   _____

Examining Committee Members:

Assist. Prof. Dr. Gökhan Osman Özgen
Mechanical Engineering Dept., METU   _____

Prof. Dr. Mehmet Çalışkan
Mechanical Engineering Dept., METU   _____

Prof. Dr. Yusuf Özyörük
Aerospace Engineering Dept., METU   _____

Assoc. Prof. Dr. Barış Bayram
Electrical and Electronics Engineering Dept., METU   _____

Assist. Prof. Dr. Kıvanç Azgın
Mechanical Engineering Dept., METU   _____

Date: 20.08.2014

I hereby declare that all information in this document has been obtained and presented in accordance with academic rules and ethical conduct. I also declare that, as required by these rules and conduct, I have fully cited and referenced all material and results that are not original to this work.

Name, Last Name : Mehmet Hakan Kandemir

Signature :

ABSTRACT

DESIGN AND IMPLEMENTATION OF AN ANNULAR ACOUSTIC LEVITATION SYSTEM

Kandemir, Mehmet Hakan

M.S., Department of Mechanical Engineering

Supervisor: Prof. Dr. Mehmet Çalışkan

August 2014, 153 pages

In standing wave acoustic levitation technique, a standing wave is obtained between a source and a reflector. Particles can be attracted towards pressure nodes in standing waves owing to the spring action. Hence, particles can be suspended in air. This operation can be performed on continuous structures as well as in several numbers of axes. In this study an annular acoustic levitation set-up is designed and built. The set-up consists of two langevin type piezoelectric transducers, two waveguides, an annular plate, an annular concave reflector, supporting structures, a signal generator and a power amplifier. The transducers are activated by harmonic signals generated by a signal generator and amplified by an amplifier to excite the waveguides. The waveguides amplify the vibration amplitude and in turn, excite the annular plate to a bending mode at a certain frequency. As the plate vibrates in bending mode, it excites the air and generates sound waves. Several types of bending modes of the plate are simulated and evaluated. With the right positioning of the reflector plate, standing waves are formed between the annular vibrating plate and the reflector plate. At the pressure nodes of the standing wave, it is demonstrated that small particles can be suspended in air.

Keywords: Acoustic Levitation, Standing Wave Acoustic Levitation.

ÖZ

HALKA ŞEKLİNDE BİR AKUSTİK LEVİTASYON SİSTEMİNİN TASARIMI VE UYGULANMASI

Kandemir, Mehmet Hakan

Yüksek Lisans, Makina Mühendisliği Bölümü

Tez Yöneticisi: Prof. Dr. Mehmet Çalışkan

Ağustos 2014, 153 sayfa

Durağan dalga ile akustik levitasyon tekniğinde bir ses kaynağı ile bir yansıtıcı arasında durağan dalga elde edilir. Akustik ses basıncı elde edilen durağan dalga formunun düğüm noktaları etrafında doğrusal bir yay gibi davranarak parçacıkları bu düğüm noktalarına çeker ve bu şekilde parçacıklar havada tutulabilir. Bu operasyon çeşitli sayıdaki eksenlerde olduğu gibi sürekli yapılar üzerinde de gerçekleştirilebilir. Bu çalışmada halka şeklinde bir durağan dalga akustik levitasyon düzeneği tasarlanıp üretilmiştir. Bu düzenekte iki adet Langevin tipi piezoelektrik transdüser, iki adet dalga kılavuzu, bir adet halka şeklinde plaka, bir adet halka şeklinde içbükey yansıtıcı, bir sinyal üreteci, bir yükseltici ve diğer yapısal elemanlar mevcuttur. Transdüserler sinyal üreteci tarafından üretilen ve yükseltici ile genliği artırılan harmonic sinyallerle uyarılır ve bu şekilde dalga kılavuzlarını uyarır. Dalga kılavuzları titreşimin genliğini artırarak halka şeklindeki plakayı bir eğilme titreşim biçiminde uyarır. Eğilme titreşim biçiminde uyarılan plaka havayı titreterek ses dalgaları oluşturur. Halka şeklindeki plakanın çeşitli eğilme titreşim biçimleri benzetim çalışmaları ile elde edilmiş ve değerlendirilmiştir. Yansıtıcının doğru konumlandırılması ile halka şeklindeki plaka ve yansıtıcı arasında durağan dalga elde edilmiştir. Bu durağan dalga formunun düğüm noktalarında parçacıkların havada tutulabileceği gösterilmiştir.

Anahtar Kelimeler: Akustik Levitasyon, Durağan Dalga Akustik Levitasyon.

To My Family

ACKNOWLEDGEMENTS

I would like to express literally the deepest of gratitudes to my supervisor Prof. Dr. Mehmet Çalışkan for his guidance, advice, encouragement and support throughout the research. Furthermore, I am very thankful for the pleasant working environment he had brought to me.

I would also like to send my apologies to the students and personnel in METU Mechanical Engineering Building B for the unpleasant noise that sounds in the building during my experimental studies.

I also want to thank to all the posers around that serve the very best of examples of how-not-to-be.

Finally and most importantly, I am grateful to my family for their support, love and encouragement throughout my life.

TABLE OF CONTENTS

LIST OF TABLES

TABLES

LIST OF FIGURES

FIGURES

LIST OF SYMBOLS

ρ_i density, density of ith medium

t time

x_j generalized coordinate, jth generalized coordinate

u_j velocity in jth generalized coordinate

P_i pressure at medium i

p Acoustic pressure

P_0 Ambient pressure

P Total pressure

Φ Velocity potential

∇ Gradient operator

$\bar{w}$ Enthalpy per unit mass

c Speed of sound

c_0 Bar velocity of sound

U Potential energy

K Kinetic energy

P^L Lagrangian pressure

P^E	Eulerian pressure
ξ	Displacement of a fluid particle from its equilibrium position
S_{ij}	Acoustic radiation stress tensor
δ_{ij}	Kronecker delta
p_i	Incident sound pressure
p_r	Reflected sound pressure
p_t	Transmitted sound pressure
r	Distance, radial distance in spherical coordinates
ω	Angular frequency
k_x	Reciprocal of characteristic width of sound beam
k_i	Wave number in i[th] medium/direction
J_n	Bessel function of first kind of order n
Y_n	Bessel function of second kind of order n
I_n	Modified Bessel function of first kind of order n
K_n	Modified Bessel function of second kind of order n
e	Euler's number
z	Part of spherical coordinate system
K_1	Effective wavenumber in z direction for fluid 1
K_2	Effective wavenumber in z direction for fluid 2
ξ	z component of acoustic particle velocity

A_i	Constant appear on equations, amplitude of vibrations
B_i	Constant appear on equations
C_i	Constant appear on equations
D_i	Constant appear on equations
Z	Ratio of impedances of two different media
γ	Ratio of specific heats of medium
ϵ	Vibration of source
ϵ_0	Vibration amplitude of source
R	Radius of rigid sphere
ζ	Location of center of the rigid sphere
θ	Angular coordinate
j_n	Spherical Bessel function of first kind of order n
h_n	Spherical Hamkel function of first kind of order n
P_n	Legendre polynomial
F_i	Force on the ith axis/mass
V	Axial displacement of the rod
E	Elastic modulus
$A(x)$	Area of rod, area
$m(x)$	Mass density
$V(x)$	Axial displacement

$F(t)$	Forcing
β	An intermediate variable as a function of frequency
L	Length of the beam/acoustic cavity
λ_n	Wavelength of sound, at n^{th} natural frequency
σ	Normal stress
h	Thickness of the plate
∇^2	Laplacian operator
∇^4	Biharmonic operator
w	Transverse displacement of plate
W	Transverse displacement of plate
$R(r)$	A separated function in bending vibrations of plate
$\Theta(\theta)$	A separated function in bending vibrations of plate
κ	An intermediate constant in Bessel functions
D	Flexural rigidity of the annular plate
ν	Poisson's ratio
M_r	Bending moment on the plate
M_θ	Bending moment on the plate
$M_{r\theta}$	Twisting moment on the plate
Q_r	Transverse shearing force on the plate
Q_θ	Transverse shearing force on the plate

V_r	Kelvin-Kirchhoff edge reaction
V_θ	Kelvin-Kirchhoff edge reaction
a	Inner radius of the annular plate
b	Outer radius of the annular plate
f_{fit}	Curve-fit function to represent the vibration distribution
d_r	Diameter of concavity of the reflector

CHAPTER 1

INTRODUCTION

1.1 Historical Perspective

Acoustic levitation can be defined as levitation of material by sound waves. Original applications were not intended to levitate material, but they helped discovery of an interesting phenomenon.

The possibility of levitating material using sound was first observed by Kundt in an impedance tube experiment in 1866. The aim of the experiment was originally to utilize dust particles to determine the speed of sound in solid bodies and gases. It was observed that if a standing wave is generated inside the tube, dust particles tend to concentrate at the pressure nodes. Bücks et al. (1933) used acoustic levitation of alcohol vapor and alcohol droplets to determine natural frequency of piezoceramic crystals. A reflector is placed parallel to the face of crystal. The crystal is excited and the distance of the reflector is adjusted such that a standing wave is generated between the crystal and the reflector. The standing wave is visualized using alcohol vapor or alcohol droplets and the half-wavelength is measured to determine the natural frequency of crystal. The alcohol particles were concentrated at the pressure nodes of the standing wave and they were used to calculate the half-wavelength of the generated standing wave.

There exist two methods of acoustic levitation, standing wave acoustic levitation and near field acoustic levitation. In standing wave acoustic levitation, air is excited

at a certain frequency with a source, while a reflector is placed parallel to the source at a certain distance. If the distance is an integer multiple of the half wavelength of the excitation frequency, standing waves are obtained between the source and the reflector. Particles can be trapped at the pressure nodes of the standing wave pattern. Standing wave acoustic levitation requires source and reflector couples. There are three-axis and single-axis set-ups. In three-axis configurations source and reflector couples are arranged orthogonally while single-axis set-ups have simply a source and a reflector. Three-axis set-ups promise more stable levitation, but stability can be improved significantly in single-axis set-ups using different types of reflectors. Due to simplicity and efficiency, single-axis set-ups are used more widely. Near field acoustic levitation replaces the reflector with the particle itself. There no longer exist standing waves, but a thin squeeze film is obtained between the source and the particle. Near field acoustic levitation can be used to levitate heavier particles. In both methods, the frequency of excitation is usually in the ultrasonic range.

In the literature, there exist many studies on both methods of levitation. Theoretical studies as well as experimental studies can be found for different cases.

1.2 Review of Literature

1.2.1 Experimental Studies

Whymark (1975) proposed a single axis standing wave acoustic levitation set-up to be used in space experiments. A set-up is designed and several experiments are carried out. The set-up was consisting of a source and a flat reflector. Excitation to the source is given by eddy currents in a metal tube which is turned integrally with the base of the vibrator. Experiments done with that set-up demonstrated that the levitation ability of the set-up is independent of the direction of the sound beam with respect to gravity. Melting and shaping experiments are performed and it is concluded that the sound intensity in the levitation zone is generally much less than

required to crystallize the levitated material. Near field acoustic levitation is also performed with a brass disc of $5\,cm$ diameter and $5\,mm$ thickness. The author proposed position control by adjusting the position of the source or the reflector, but that control is not realized.

An acoustic levitation set-up with position control by resonance tracking is designed by Zhuyou et al. in 1992. The standing wave acoustic levitation set-up was consisting of a source, a flat reflector and a resonance tracking system. Piezoelectric disks were used to excite the source at desired frequency. The resonance chamber between the source and the reflector was cylindrical and covered with a Plexiglas tube. Resonance tracking system is designed as the properties of the medium may change during the levitation operation. The phase shift between the input and the output signals are controlled. Input signal is taken as the voltage applied to the source and the output signal is taken from a condenser microphone placed on the reflector. Using that information, the length of the chamber is changed to get the phase shift deviation to a minimum value. The position of the source and the reflector is adjusted using a control circuit such that the resonance is maintained and the position of the levitated particle is kept in a range. Various particles have been levitated in this set-up stably for around 2 hours.

Hashimoto et al. (1996) achieved near field acoustic levitation of flat samples using flexural vibrations of a plate. The plate is excited in a flexural mode using a piezoelectric transducer such that every segment of the plate makes piston motion at the same frequency, with different amplitude. Standing wave pattern is obtained on the plate and particles of several kilograms are successfully levitated. It was concluded that the levitation distance is proportional to the source vibration amplitude and inversely proportional to mass per unit area of the levitated object. The levitated object has to have a flat face facing the source and it should cover at least three halves of wavelength of the flexural vibration. As standing wave exists on the plate, objects are not transformed and stood at the same stable position for the duration of levitation. Later, Hashimoto et al. (1998) showed that transportation of objects using near field acoustic levitation is possible if traveling waves are excited on the plate. A rectangular plate is excited to obtain traveling waves at two

positions such that at one position the plate is excited, at the other position the vibrations are absorbed. The levitated object is observed to follow the energy flow on the plate, traveling from the exciting transducer to the absorbing transducer. It is concluded that the acoustic viscous forces were causing the object to travel in the energy flow direction. Plates of several different sizes are investigated and it is concluded that in order the plate to vibrate uniformly across the width, the width should be smaller than one third of the wavelength of the flexural vibration. The transportation speed is found out to be proportional to the vibration amplitude of the plate and inversely proportional to the weight of the levitated object. The authors also proposed using a non-uniform-shaped plate to prevent the falling of the object from the top of the plate.
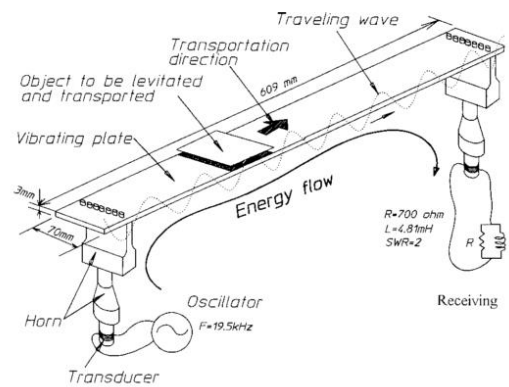
Figure 1 – Levitation set-up proposed by Hashimoto et al. (1998).

Hu et al. (1999) developed an ultrasonic motor utilizing near field acoustic levitation and the acoustic viscous forces between the source and the levitated object. The stator of the motor is used as source and the rotor of the motor is used as levitated object. If the vibration velocity is increased such that the boundary layer is separated from the rotor surface, the levitation force increased rapidly with further increase in the vibration velocity. Same effect is observed when the levitation distance is less than a certain threshold. The authors have concluded that if the driving frequency is tuned to one of the resonant frequencies of the air gap, the

levitation force will be drastically increased. With careful adjustment of vibration distribution, a speed of 4400 rpm is achieved during the experiments.
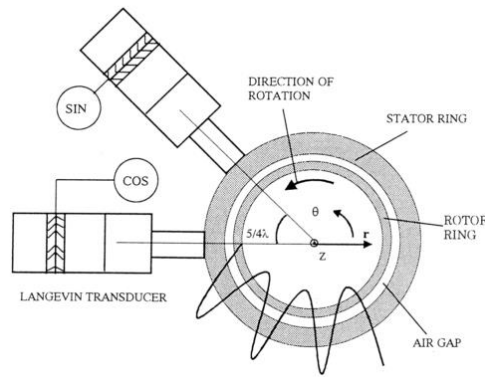
Figure 2 - The ultrasonic motor developed by Hu et al. (1999).

Loh et al. (2000) achieved transport of objects with near field acoustic levitation using two-mode excitation. The set-up was similar to the one of the Hashimoto et al. (1998), but there were two-point excitation on the beam rather than an exciting and an absorbing point. The excitation frequency was at the middle of two flexural resonant frequencies which do not have an anti-resonance frequency between. The two points on the beam are excited at a frequency but different phases. The phase difference between excitations determined the direction of the progressing wave. Some frequencies near the excitation frequency resulted in no progressive waves, implying there were two progressive waves cancelling each other. The authors have also developed an open loop control system to control the position of the particles levitated using this set-up. Open loop control served well initially, but closed loop control is suggested later. A transport speed of 10 cm/s is achieved for a 30 g object.

Figure 3 – Two point excitation used by Lou et al. (2000).

Matsuo et al. (2000) studied the lateral stability of an object levitated using near field acoustic levitation. The lateral oscillatory motion of the object was modeled as a harmonic motion and the distribution of the suspension coefficient, which appeared as stiffness in the equation of motion, is investigated. Piston motion as well as flexural vibrations of a plate can be used to levitate an object using near field acoustic levitation, the authors have found out that flexural vibrations provide more stability in lateral motion.

A ring-type acoustic levitator with low energy consumption was developed by Kaduchak et al. (2002). A hollow cylindrical piezoelectric tube is used as the levitator, where the resonant frequency of the inner cavity is matched with that of the piezoelectric material so that standing waves are generated inside the tube. In this case, all the walls of the cavity acted like both source and reflector. Stable equilibrium positions were parallel surfaces to the walls of the piezoelectric tube. Levitation of water drops were achieved in that set-up. The authors also proposed a tunable cylindrical levitation device. The resonant frequency of the inner cavity could be adjusted using an alignment rod placed in the cavity.

stable equilibrium
surfaces

C

B

A

PZT cylinder
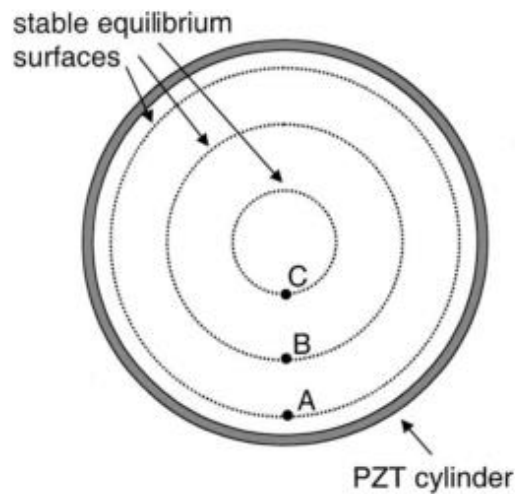
Figure 4 – Cylindrical levitation device proposed by Kaduchak et al. (2002).

Chang (2004) used near field acoustic levitation to design an ultrasonic clutch. The clutch has two cylindrical langevin type transducers, one is coupled to the motor, the other is coupled to the shaft and their surfaces are in contact. The central axis of the transducers coincides with the axis of rotation. When the transducers are not activated, their surfaces are in contact and the motion is transmitted. To separate the surfaces, at least one of the transducers is activated and the motion transmission is prevented. Due to viscous forces between the surfaces, there was motion transmission even if the transducers are activated.

Kozuka et al. (2006) achieved standing wave acoustic levitation by crossing two sound beams. Two transducers are placed facing each other and excited at the same frequency. The transducers are placed such that the sound beams generated by each transducer cross each other. At the crossing locations, standing waves are observed to be generated. The authors have reported that it is possible to control the pattern of the standing wave by controlling the phase difference between two transducers. Movement of small polystyrene particles is reported to be achieved by changing the

phase difference.
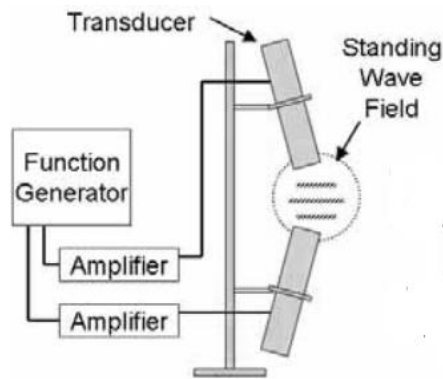
Figure 5 – Standing wave generation by crossing sound beams by Kozuka et al. (2006).

Ide et al. (2007) designed a linear noncontact bearing using near field acoustic levitation. Right angle shaped beam is excited by two transducers at both ends, in both standing waves and traveling waves. As the beam and the levitated slider both have right angle cross section, lateral stability is provided. Better levitation properties are obtained when the beam and object are V-shaped as the object covers all the cross-section of the beam. In Λ-shaped configuration, the levitated object cannot cover all the cross section, the uncovered sections are where the vibration amplitude is maximum. The beam was excited by two different methods, diagonally and vertically. Diagonal excitation provided both higher forces and better levitation stability. The authors have also successfully performed transportation in both directions by changing the phase difference between transducers.

Field et al. (2007) designed and manufactured an adjustable standing wave acoustic levitator. Humidity, temperature and pressure are measured via sensors and reflector position is adjusted via linear actuator. The authors have presented a guide to design an acoustic levitator from scratch. The final product successfully levitated a 5 μl water droplet with low energy consumption.

Zhao et al. (2009) presented a unique way of levitating large planar objects. The levitated object acted as reflector, but standing waves are obtained between the reflector and the source. The object is not trapped in any of the pressure nodes and

the levitation force was much smaller compared to a near field acoustic levitation. The source was a circular plate excited from its center at one of its flexural modes. A load cell is placed on a reflector, which is acting as levitated object, and the levitation force is observed with respect to the distance from the source. Levitation is found out to be much stronger at the near field acoustic levitation regions, and some force peaks are observed at distances that are integer multiples of the half wavelength of the excitation frequency. A compact disc was successfully levitated using this set-up, around a half wavelength above the source. The authors have taken into account also the absorption at the object, so that the simulation results fitted well with the experiments.

Traveling waves have previously been used in transport with near field acoustic levitation, but Ito et al. (2010) used them with standing wave acoustic levitation. An aluminum plate is excited at its one end via a langevin type transducer and lead plates placed at the other end to absorb the vibration. The plate is excited at a frequency such that traveling waves obtained on that plate. A reflector is placed parallel to the plate to generate standing waves. Standing wave field is obtained in the vertical direction while traveling wave field is obtained in the horizontal. The particle is suspended in vertical and undergone propulsion in the horizontal due to the wave field generated. Viscosity of the air was resisting the motion; hence a terminal speed was reached. The authors successfully levitated and transported a small polystyrene particle with a terminal speed of $410 \; mm/s$.
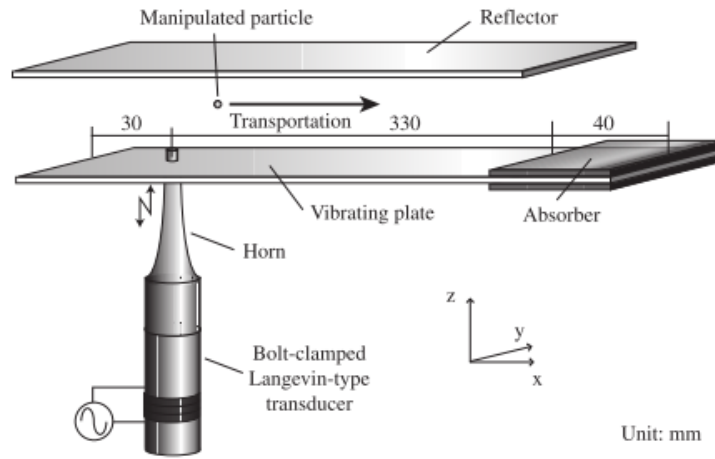
Figure 6 – Transportation prototype proposed by Ito et al. (2010).

Koyama et al. (2010) proposed a standing wave acoustic levitation set-up containing a long bending plate and a reflector. Position control of the particles along the length of the beam is achieved. The bending plate is excited at one of its flexural modes at two ends and a reflector is placed parallel to the plate to obtain standing waves. As the plate is excited at one of its modes, standing wave is obtained both in the horizontal and in the vertical. Every point on the plate made piston motion individually; hence every point except vibration nodes on the plate was suitable for levitation. The authors have managed levitation of liquid droplets and by changing the phase difference between the transducers they managed to control the wave pattern on the plate. Controlling the wave pattern on the plate led to the control of the levitation positions in the levitation area. Position control of accuracy of $0.046\ mm/degree$ is reported to be achieved.
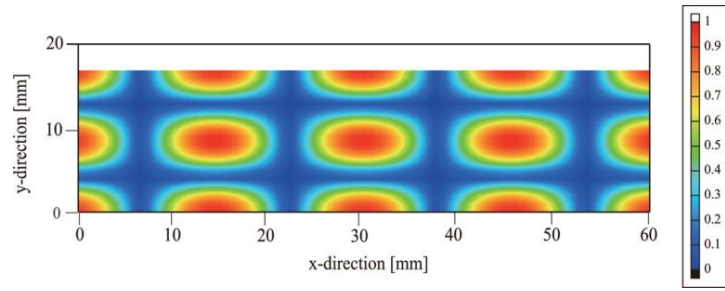
Figure 7- Standing wave field obtained by Koyama et al. (2010).

Koyama et al. (2010) also achieved standing wave acoustic levitation on a circular plate. The set-up was consisting of a circular plate, a circular reflector and 24 piezoelectric elements used to excite the circular plate. The plate is excited at one of its flexural modes by the arrangement of piezoelectric elements. The flexural mode excited was $(1, 4)$ mode. 24 piezoelectric elements are arranged such that by controlling their phase, the arrangement of the mode shape can be controlled. Switching their phases in order helped to move the particle on a curve on the circular plate. As the phases are switched, the mode shape pattern on the plate is rotated respectively around the central axis of the vibrating plate. In other words, vibration pattern on the plate is rotated instead of the plate. The reflector of the set-up is flat and stood still in the process of moving particles. Polystyrene particles of several mm of diameter are reported to be levitated and manipulated successfully on a circular trajectory.
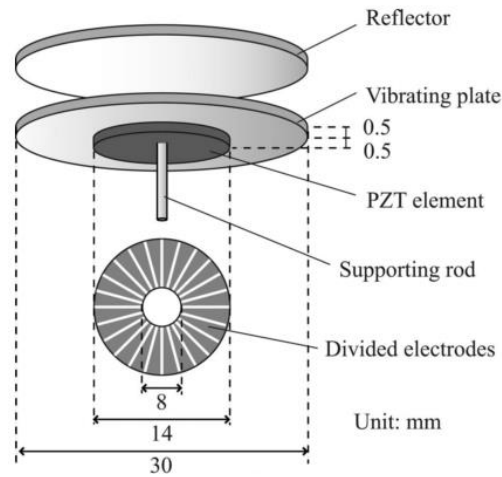
Figure 8 – Circular arrangement used by Koyama et al.

Demore et al. (2010) designed and manufactured a micro particle manipulation system. The particles are levitated vertically using standing wave acoustic levitation and moved horizontally along an axis by suitable arrangement of transducers. The path of the particle is covered with an array of piezoelectric elements so that by actuating the required elements, standing waves can be generated in any part of the tube. The authors have achieved transportation of small particles by actuation of the transducers in a certain order. It was concluded that by finer arrangement of the piezoelectric array and optimized design of levitation region, larger forces and better position control is possible.

Courtney et al. (2010) proposed a manipulation system utilizing superposition of two orthogonal standing waves. The set-up was consisting of two parts, one for levitating in vertical and one for manipulating in horizontal. The particles are first levitated in vertical to a certain height so that the horizontal system can control the position of the particles. The vertical system was a simple standing wave acoustic levitation set-up with a larger source and reflector area. Horizontal manipulation is performed by two transducers placed opposite to each other. Exciting traveling waves from the counter faced transducers yielded standing wave formation inside the cavity provided that the wave amplitudes are the same. By controlling the phase

difference between the opposite traveling waves, position of the pressure nodes of the standing wave pattern can be controlled.
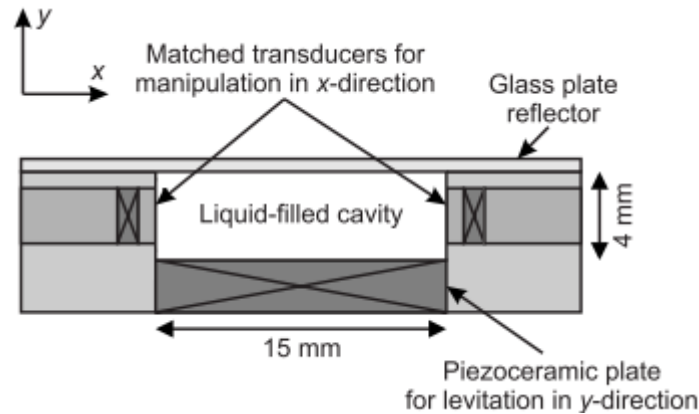
Figure 9 – Horizontal manipulation system proposed by Courtney et al. (2010).

Near field acoustic levitation is reported to be able to suspend objects by Takasaki et al. (2010). In the traditional near field acoustic levitation, the object is levitated over a vibrating surface about several micrometers. Takasaki et al. managed to suspend a flat object below a vibrating surface. The authors have proved that below a certain distance of separation, attractive forces are possible such that an object can be suspended below a vibrating surface.

Baer et al. (2011) were the first to use concave radiation sources in a standing wave acoustic levitation set-up. A flat radiator and a concave reflector have previously been proven to offer more lateral stability than a flat-flat couple. The authors have designed and manufactured a set-up containing a concave reflector and a concave radiator. Investigations have shown that a concave-concave couple applies more lateral force hence provides more lateral stability than a flat-flat couple.

1.2.2   Theoretical Studies

Theoretical studies on acoustic levitation are known to be started with King (1934). King has studied acoustic radiation force on rigid spheres in a compressible, non-viscous medium. Radiation pressure due to both progressive waves and standing waves are studied and it is concluded that in standing wave fields radiation pressure is much higher than that in the progressive wave fields. King indicated that in standing wave fields, radiation pressure acting on small dust particles forces them to the pressure nodes. Suspension of particles against gravity is also discussed and stated as experimentally possible. The author also predicted that the motion of the suspended particles is nothing but a harmonic oscillation around the suspension point.

Embleton (1954) has studied spherical body in a progressive spherical sound field. The mean radiation force is determined by summation of contributions of velocity potential and particle velocity. The contributions are found by integrating the respective properties on the particle surface. Embleton obtained curves to predict the radiation pressure on a spherical particle with respect to the distance to the source. It is shown that it is possible to obtain attractive or repulsive forces by adjusting the radius-to-distance ratio.

Relatively simple expressions for acoustic radiation pressure on a particle in a sound field have been derived by Gorkov in 1962. Method of Gorkov was so generic that it can be applied to any material of small particles in any type of sound fields. The restrictions of that method were the particle is assumed to be smaller than the wavelength of the excitation sound and the excited medium is non-viscous. The velocity potential is separated into incident and scattered parts and the scattered potential is expressed in terms of incident potential. Gorkov obtained the time averaged force potential and the final expression was applicable to even compressible particles in any sound field. Gorkov's study served the base of the most of the future theoretical works.

14

The application of the Gorkov's method to several types of standing wave fields was realized by Barmatz in 1985. Plane, cylindrical and spherical standing wave fields are considered and acoustic radiation potential is calculated. Positioning modes of each type of standing wave fields are investigated and compared and it is concluded that spherical fields are less useful for acoustic levitation. The author considered only rigid spheres but stated that with certain adjustments in procedure it is possible to include compressible spheres in the study. It was concluded that for all the types of the standing wave fields, the most practical modes are the lowest order ones. The author also stated that several levitation experiments are carried out in different types of fields but no results were presented in that particular publication.

A finite elements study is carried out by Hatano in 1994, as a part of a space shuttle program for NASA. The analysis is carried to aid the design of a tube type levitator and an axisymmetric model is used for simplicity. Velocity potential, positioning force and resonance shift is investigated as a function of particle size and position. To validate the results, a probe microphone is used to measure the pressure in the acoustic levitation tube and the results matched well with the simulation.

Xie et al. (2002) investigated the effect of geometric parameters on levitation capabilities in single axis standing wave acoustic levitation set-ups. The study is mainly focused on the parameters of reflector and the source. The source radius, reflector radius and reflector curvature radius are varied to investigate the enhancement of levitation with respect to the given parameters. Several types of reflectors are investigated and it is concluded that concave spherical reflectors promise stronger levitation than the likes of a hyperboloid of revolution or a paraboloid of revolution. It was also observed that the lower order modes provide stronger levitation. The authors concluded with careful adjustment of geometrical parameters, it is possible to enhance the levitation significantly. They achieved to levitate an iridium sphere in their experimental set-up.

A theoretical and experimental investigation of near field acoustic levitation is studied by Nomura et al. in 2002. As near field acoustic levitation utilizes a narrow

squeeze film between the source and the object, the authors have included viscosity of air in the calculations and assumed that the levitated object does not move in any means. They later measured that if the excitation frequency is close to one of the transverse natural frequencies of the levitated object, the object starts to vibrate significantly. The authors have validated the assumptions previously made by Hashimoto et al. in 1996 about the relation between the weight of the object and the levitation distance. They also carried out some experiments and observed an agreement between their theoretical predictions and experimental results.

Mitri (2005) studied the acoustic radiation forces of coated spheres in a plane progressing wave field. The spheres were elastic and the coating material is a viscoelastic material. The author concluded that radiation force on a coated sphere increases with the increase in the coating layer thickness due to the effect of absorption. The surrounding medium is assumed to be inviscid and several numerical examples are presented. It is hinted that with a similar methodology, spherical shells can also be studied.

Later, acoustic radiation force on spherical shells in standing wave field is studied by Mitri in 2005. In that study the material inside the shell is mainly investigated with the material of the shell and the surrounding medium. It is concluded that if the inside material causes a large impedance mismatch with the shell, it faces higher resonance force as it does not allow the waves to penetrate through the object. The absorption of the sound by the shell is observed to have great impact on the radiation force.

Mitri also studied the behavior of spherical shells under progressive wave field in 2005. The results obtained were similar to those for standing wave fields. For both studies, the author used ideal fluids as surrounding medium, but suggested that the problems should also be studied for real fluids.
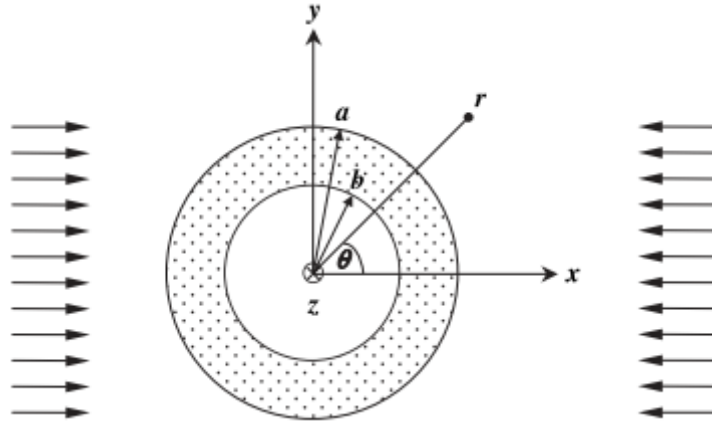
Figure 10 – Sketch of the spherical shell investigated by Mitri (2005).

Jun et al. (2007) studied the resonance shift in a cylindrical levitator using boundary element method. The authors have defined the distance between the source and the reflector as resonant interval. The resonant interval can easily be converted into the resonant frequency as it is nothing but an integer times the half wavelength of the corresponding resonant frequency. The effect of particle position and the size on the resonant interval is investigated in this study. A particle placed in the field results in a decrease in the resonance interval and it is found out that larger particles cause greater shift while the smallest particles cause almost no difference. As the particle moves in the standing wave field, the position also causes a resonance shift. The disturbance is higher at the antinodes than at the nodes of pressure. The authors have also conducted some experiments and obtained similar results to their theoretical work.

Transient properties of levitated objects with NFAL are studied by Jia et al. in 2011. A theoretical model is developed to predict the time response of the levitated material. Several calculations are carried out with differing velocity amplitudes. It is found out that as the velocity amplitude increases, the levitated object reaches the stable levitation position more rapidly. The authors have also stated that the velocity amplitude can be adjusted to make the time to reach stable position shortest.

A matrix method to simulate acoustic levitation is developed by Andrade et al. in 2011. The method discretized the sound field by dividing the surface of the source and the reflector into small areas. The space of interest is divided into measurements points at which the sound pressure is calculated. The interaction between any points or areas in the field is represented by transfer matrices. The reflections from the surfaces of the transducer and the reflector are also taken into account by transfer matrices. Using the pressure field obtained considering as many reflections as possible, velocity potential and velocity field can be obtained using Gorkov's method. The authors have also performed a finite element study to compare the results obtained from matrix method. The results have agreed and it is concluded that as the reflector curvature radius increase, more reflection terms should be included in the calculations. A non-contact manipulation system is also simulated with this method and the authors have concluded that the method is an efficient method for three dimensional set-ups without axisymmetry.
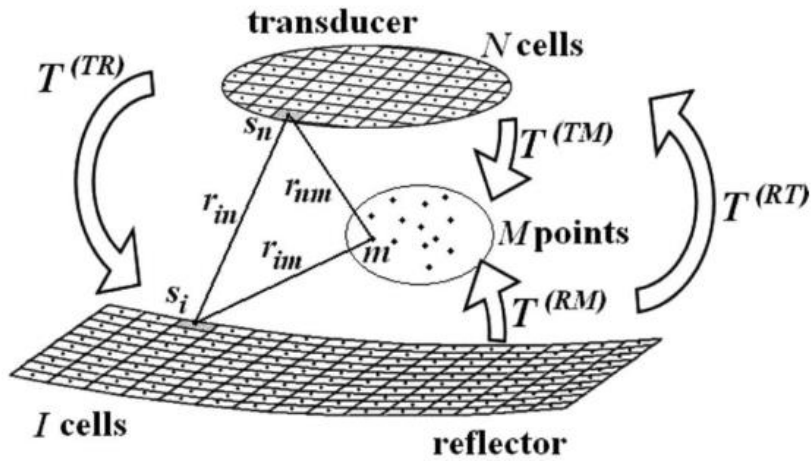
Figure 11- Schematic of the matrix method developed by Andrade et al. (2011).

1.2.3 Reported Applications of Acoustic Levitation

Applications of acoustic levitation are mainly focused in the chemical and biological sciences. Cronin et al. (1989) used acoustic levitation as an infrared spectroscopy sampling technique. A standing wave acoustic levitation set-up with a concave radiator and a flat reflector is used. The infrared spectrums of levitated particles are obtained. It was observed that the quality of the spectrum is highly dependent on the stability of levitation. The authors reported better results with more stable levitation. The set-up did not include a resonance tracking system; hence the stability of levitation is often affected by the change of temperature in the field. Liquid droplets with high vapor pressures are evaporated due to heating from the infrared beam. A better set-up with two radiators and ability to adjust the resonance is later suggested.

Surface tension of a liquid droplet is determined with the help of acoustic levitation by Tian et al. (1995). An acoustic levitation set-up is used to suspend the drop and measure the dimensions while the droplet is assumed to be symmetrical about its vertical axis. The surface tension is determined by measuring the altitude and the aspect ratio of the drop. The image of the drop is taken and measurements are done on the image captured. The authors have used pure water and dodecane in this set-up but heavier liquids can be used with proper set-ups.

Hawkes et al. (1998) used acoustic levitation to manipulate microparticles in a flow field. Suspension of yeast and orange beads in distilled water have entered the set-up in a laminar flow field. The field is later subjected to acoustic standing waves to concentrate the particles at the pressure nodes. The concentrated flow is later expanded for visualization purposes. As the particles concentrate at the nodes of the pressure field, band formation in the laminar flow is observed. The authors have concluded that this set-up is a useful method to visualize small cells and further developments for smaller particles would be feasible.
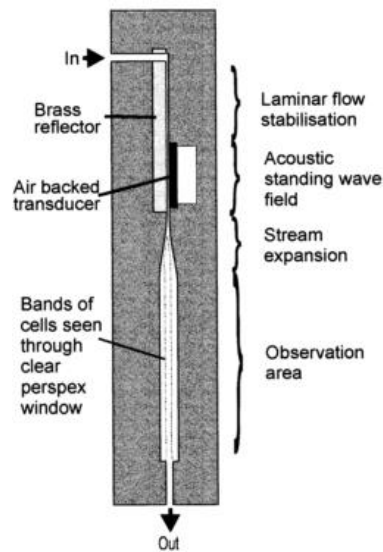
Figure 12 – Set-up used by Hawkes et al. (1998).

In 2001, Cao et al. achieved preparation of epoxy blends with nanoparticles by acoustic levitation. The mixture is brought into a standing wave acoustic levitator in such a point that the effect of different specific gravities of materials is eliminated. It is reported that this method provided a highly uniform microstructure. The blends prepared in a normal gravity field and in a microgravity field provided by acoustic levitation are compared. The nanoparticles are observed to be uniformly dispersed in the epoxy matrix and the polyester was at a highly dispersed amorphous state. The authors stated that such properties could not be obtained in a blend prepared under gravity.

Lü et al. (2006) performed experiments on supercooling of NaCl and KCl solutions in acoustic levitation field. Surface tension and bubble growth are observed to be the main factors on supercooling capability under standing wave acoustic levitation. NaCl solution is observed to have more surface tension. Large bubbles are noted to act as nucleation catalysts to decrease supercooling. As ionic concentration increases, NaCl solution is also reported to have more rapid decrease in gas concentration. The authors have concluded that NaCl is supercooled better due to the reasons described.

Small living animals have been levitated by standing wave acoustic levitation by Xie et al. in 2006. An ant, a ladybug and a young fish is levitated using acoustic levitation. The animals naturally tried to escape from the acoustical trap but none of them achieved to do so. The young fish is reported to be influenced badly due to lack of water. As the animals are of irregular shape, only ladybug can be simulated by computer. The animals have stably been levitated but as they move, the scattering from bodies and their influence on acoustic field cannot be predicted.
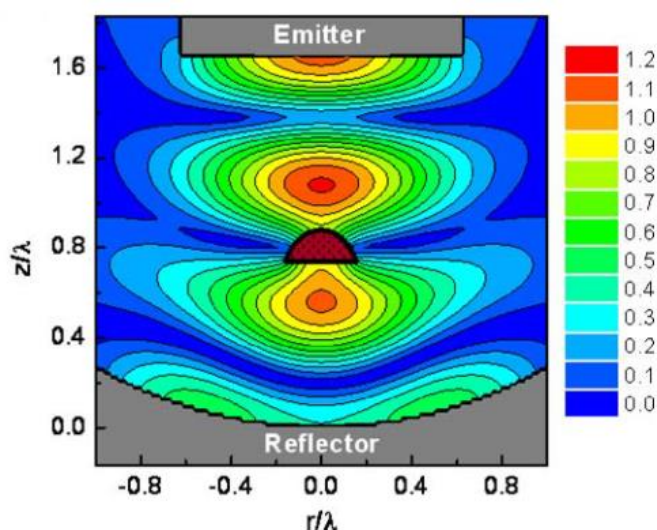
Figure 13 – Simulation of a Ladybug under acoustic levitation, Xie et al. (2006).

Leiterer et al. (2008) used standing wave acoustic levitation as a sampling technique for fluorescence studies. The main advantage of levitation was eliminating the intervention from supports. The infrared scattering and the shadow of the levitated particle is monitored during the experiments and several organic particles are examined.

In 2012, Dou et al proposed acoustic levitation to solve the aggregation problem in nanoparticle blends in polymer matrices. The microgravity condition provided by acoustic levitation helped the organic particles to disperse more uniformly. The

solution with acoustic levitation is reported to be better than the likes of making the monomer more viscous or making the particles hydrophilic.

To conclude this part, acoustic levitation is theoretically well understood in modern era. Applications are mainly focused on chemistry and life sciences. Systems to manipulate particles with acoustic levitation are well developed as basic set-ups. However, more complex and continuous structures still attract attention.

1.3 Objective and Scope of the Thesis

The aim of the thesis is to design and implement an annular acoustic levitation system. The experimental set-up is consisting of an annular plate, two transducers and waveguides, a reflector and other structural parts.

The annular plate is flexurally excited. It is designed such that it possesses a radial resonance around $20\ kHz$. The excitation is given by two langevin type transducers operating at the resonant frequency of the set-up. Waveguides will be used to excite the plate. Waveguides are excited by the transducers and they excite the plate with amplified vibrations. The waveguides are placed such that when they are turned on, the plate will vibrate at resonance. The vibrations of the plate will excite the air and the reflector is placed to obtain standing wave field.

The set-up is the first study on Acoustic Levitation in Turkey. In the literature, a number of continuous structures are used as sound sources in levitation set-ups. Originality of the work lies in that none of the known studies utilized any type of annular plates so far. Therefore, this study is also the first to use an annular plate as a sound source. With the implementation of the annular plate as the sound source, it is projected to be possible to levitate material in several numbers of axes.

This thesis covers the design and implementation of a set-up for use in experimental works regarding to acoustic levitation. A number of sample experiments will be carried out on this set-up.

In Chapter 1, the current status of the literature is presented. Chapter 2 covers an overview of radiation pressure and acoustic levitation is given. Chapter 3 presents the mechanical vibrations section. Chapters 4 and 5 cover the design and detail the experimental set-up, respectively. Chapter 6 concludes the thesis with discussions.

CHAPTER 2

ACOUSTIC LEVITATION

2.1 Acoustic Radiation Pressure

As a material surface is exposed to a sound field, it experiences the effect as a pressure. The excess pressure on the surface is defined as acoustic radiation pressure. This excess pressure applies a force onto the material, which is the acoustic radiation force. In this section, acoustic radiation pressure is defined for several cases and an example will be presented.

2.1.1 Mean Excess Pressure

The continuity equation for an ideal fluid is;

$$\frac{\partial \rho}{\partial t} + \frac{\partial (\rho u_j)}{\partial x_j} = 0 \qquad (1)$$

And the momentum equation is

$$\rho\left(\frac{\partial u_i}{\partial t} + u_j \frac{\partial u_i}{\partial x_j}\right) = -\frac{\partial P}{\partial x_i} \tag{2}$$

In these equations, ρ is the density of the fluid, t is the time, x_j is the jth generalized coordinate, u_j is the velocity in the jth generalized coordinate and P is the pressure in the medium. Pressure fluctuation due to sound follows an adiabatic process in air and sound field in an inviscid fluid is irrotational. Equations (3) and (4) are valid for the above cases.

$$u = \nabla\phi \tag{3}$$

$$\nabla w = \frac{\nabla P}{\rho} \tag{4}$$

where ∇ is the gradient operator, Φ is the velocity potential and w is the enthalpy per unit mass. Equation (2) can be rewritten for an inviscid fluid as

$$\nabla\left[\frac{\partial \phi}{\partial t} + \frac{1}{2}|\nabla\phi|^2\right] = -\frac{\nabla P}{\rho} \tag{5}$$

Hence

$$\nabla\left[\frac{\partial \phi}{\partial t} + \frac{1}{2}|\nabla\phi|^2\right] = -\nabla w \tag{6}$$

Equation (6) will be integrated in space. A constant C' will be obtained, which is constant in space but dependent on time.

$$w = -\frac{\partial \phi}{\partial t} - \frac{1}{2}|\nabla \phi|^2 + C' \tag{7}$$

To obtain an expression for the pressure, a Taylor series expansion of P in w can be written to second order as in Equation (8). P_0 is the ambient pressure.

$$P = P_0 + \left(\frac{\partial P}{\partial w}\right)w + \frac{1}{2}\left(\frac{\partial^2 P}{\partial w^2}\right)w^2 + \cdots \tag{8}$$

At equilibrium, Equations (9) and (10) are also valid for the adiabatic process

$$\left(\frac{\partial P}{\partial w}\right) = \rho \tag{9}$$

$$\left(\frac{\partial^2 P}{\partial w^2}\right) = \frac{\rho}{c_0^2} \tag{10}$$

In these equations c_0 is the speed of sound in the medium. Substituting Equations (9) and (10) into the expansion obtained in Equation (8)

$$P = P_0 + \rho_0 \left(-\frac{\partial \phi}{\partial t} - \frac{1}{2} |\nabla \phi|^2 + C' \right)$$

$$+ \frac{1}{2} \frac{\rho_0}{c_0^2} \left(-\frac{\partial \phi}{\partial t} - \frac{1}{2} |\nabla \phi|^2 + C' \right)^2 + \cdots \qquad (11)$$

Excess pressure is defined as $-P_0$, and it is obtained by simply arranging Equation (11).

$$P - P_0 = \frac{1}{2} \frac{\rho_0}{c_0^2} \left(\frac{\partial \phi}{\partial t} \right)^2 - \frac{1}{2} \rho_0 |\nabla \phi|^2 + \rho_0 C' \qquad (12)$$

As this is an inviscid fluid, Equation (13) is valid and it can be substituted into Equation (12).

$$\frac{\partial \phi}{\partial t} = -\frac{p}{\rho_0} \qquad (13)$$

After inserting Equation (13) into Equation (12) and averaging the equation over one cycle, denoted by $\langle \, \rangle$, one can obtain the mean excess pressure as

$$\langle P - P_0 \rangle = \frac{1}{2\rho_0 c_0^2} \langle p \rangle^2 - \frac{1}{2} \rho_0 \langle u \cdot u \rangle + C \qquad (14)$$

Where

$$C = \rho_0 \langle C' \rangle \tag{15}$$

$$\langle U \rangle = \frac{\langle p^2 \rangle}{2\rho_0 c_0^2} \tag{16}$$

$$\langle K \rangle = \frac{1}{2}\rho_0 \langle u \cdot u \rangle \tag{17}$$

In Equations (16) and (17), $\langle U \rangle$ is the time averaged potential energy density and $\langle K \rangle$ is the time averaged kinetic energy density, C is a constant.

The mean excess pressure is defined for a fixed point in space so far. It may as well be defined for a certain particle moving in space. It will be denoted as mean Lagrangian excess pressure. The Lagrangian pressure can be expressed in terms of Eulerian pressure as follows

$$P^L = P + \xi \cdot \nabla P \tag{18}$$

$$\langle P^L - P_0 \rangle = \langle P - P_0 \rangle + \langle \xi \cdot \nabla P \rangle \tag{19}$$

Where ξ is the displacement of the particle from its equilibrium position. The last term in Equation (19) is nothing but (Wang et al. 1998) the following expression

$$\langle \xi \cdot \nabla P \rangle = \rho_0 \langle u \cdot \mathrm{u} \rangle = 2\langle K \rangle \tag{20}$$

Hence the mean excess pressure of a particle is obtained as

$$\langle P^L - P_0 \rangle = \langle U \rangle + \langle K \rangle + C \tag{21}$$

2.1.2 Acoustic Radiation Stress Tensor

Acoustic radiation stress tensor of a point in space can be defined using continuity and momentum equations:

$$\frac{\partial(\rho u_i)}{\partial t} + \frac{\partial(\rho u_i u_j)}{\partial x_j} = -\frac{\partial P}{\partial x_i} \tag{22}$$

Equation (22) may be arranged as;

$$\frac{\partial(\rho u_i)}{\partial t} = -\frac{\partial P}{\partial x_i} - \frac{\partial(\rho u_i u_j)}{\partial x_j} \tag{23}$$

The time average over one cycle is used to obtain the acoustic radiation stress tensor. Time average over one cycle will be denoted by $\langle \ \rangle$.

$$\langle \frac{\partial(\rho u_i)}{\partial t} \rangle = \langle -\frac{\partial P}{\partial x_i} - \frac{\partial(\rho u_i u_j)}{\partial x_j} \rangle \qquad (24)$$

The left hand side of Equation (24) is equal to zero in steady state, and the acoustic radiation stress tensor is defined as:

$$\frac{\partial S_{ij}}{\partial x_j} = 0 \qquad (25)$$

and

$$S_{ij} = -\langle P \rangle \delta_{ij} - \langle \rho u_i u_j \rangle \qquad (26)$$

Recall that

$$P = P_0 + p \qquad (27)$$

$$\rho = \rho_0 + \rho' \qquad (28)$$

The acoustic radiation stress tensor can also be expressed as, replacing P by $P - P_0$

$$S_{ij} = -\langle P - P_0 \rangle \delta_{ij} - \rho_0 \langle u_i u_j \rangle \qquad (29)$$

2.1.3 Plane Wave Incident on a Flat Interface

Let there exist a flat interface such that the incident plane wave is partially reflected and partially transmitted. The interface separates two media with different densities and speeds of sound, and the incidence is normal. Let the incident beam be defined as:

$$p_i = A J_0(k_r r) e^{[i(K_1 z - \omega t)]} \tag{30}$$

The reflected and transmitted beams are, respectively, defined as

$$p_r = B J_0(k_r r) e^{[-i(K_1 z + \omega t)]} \tag{31}$$

$$p_t = D J_0(k_r r) e^{[i(K_2 z - \omega t)]} \tag{32}$$

In the representation of the incidence, cylindrical coordinates are used where r denotes the radial distance. A, B and D are the amplitudes of the respective pressures. To apply the compatibility conditions at the interface, the particle velocities should be defined in z direction as:

$$\xi_i = \frac{K_1 A}{\omega \rho_1} J_0(k_r r) e^{[i(K_1 z - \omega t)]} \tag{33}$$

$$\xi_r = -\frac{K_1 B}{\omega \rho_1} J_0(k_r r) e^{[-i(K_1 z + \omega t)]} \qquad (34)$$

$$\xi_t = \frac{K_2 D}{\omega \rho_1} J_0(k_r r) e^{[i(K_2 z - \omega t)]} \qquad (35)$$

The compatibility conditions at the interface are:

$$p_i + p_r = p_t \qquad (36)$$

$$\xi_i + \xi_r = \xi_t \qquad (37)$$

Defining the ratio of impedances, Z

$$Z = \frac{\rho_1 c_1}{\rho_2 c_2} \qquad (38)$$

Where the c_i is the speed of sound in i^{th} medium. The compatibility equations will result

$$B = \left(\frac{1 - Z}{1 + Z}\right) A \qquad (39)$$

$$D = \left(\frac{2}{1+Z}\right)A \qquad (40)$$

To obtain the mean excess pressure at either side of the medium, above expressions can be inserted into the Equation (14). For medium 1, mean excess pressure is

$$\langle P_1 - P_0 \rangle = \frac{AB \cos(2K_1 z)}{\rho_1 c_1^2}[J_0(k_x x)]^2$$
$$+ \frac{1}{4\rho_1 c_1^2}\left(\frac{k_x}{k_1}\right)^2 [(A^2 + B^2)\{[J_0(k_x x)]^2 \qquad (41)$$
$$- [J_0'(k_x x)]^2\}$$
$$- 2AB \cos(2K_1 z)\{[J_0(k_x x)]^2 + [J_0'(k_x x)]^2\}]$$

For medium 2, mean excess pressure is

$$\langle P_2 - P_0 \rangle = \frac{D^2}{4\rho_2 c_2^2}\left(\frac{k_x}{k_2}\right)^2 \{[J_0(k_x x)]^2 - [J_0'(k_x x)]^2\} \qquad (42)$$

In these equations, K_i is the effective wavenumber in z direction for fluid i.

2.2 Near Field Acoustic Levitation

In near field acoustic levitation, the object gets closer to the source and levitated at a distance of several micrometers. The pressure on the object can be expressed if the radiation pressure is evaluated at/on the location/surface of the levitated object. Chu

et al. (1982) evaluated the radiation pressure on a flat object above a piston source in the following way. The source is vibrating harmonically as $\epsilon = \epsilon_0 \cos \omega t$ and the resulting radiation pressure is

$$P = \frac{1+\gamma}{2} \frac{\epsilon_0^2}{4} \frac{\rho_0 \omega^2}{\sin^2 kz} \left(1 + \frac{\sin 2kz}{2kz}\right) \tag{43}$$

where γ is the ratio of the specific heats of the media. If the levitation distance is small enough that $kz \ll 1$, Equation (43) may take the form

$$P = \frac{1+\gamma}{4} \rho_0 c^2 \frac{\epsilon_0^2}{z^2} \tag{44}$$

And the levitation distance will be

$$z = c\epsilon_0 \sqrt{\frac{\rho_0(1+\gamma)}{8P}} \tag{45}$$

The pressure can be taken as the weight per unit area of the object in direction gravitational field. Therefore, it can be interpreted that if the weight per unit area of the object increases, the levitation distance will decrease. The levitation distance is directly proportional to the amplitude of the source vibration, and the frequency does not affect the levitation distance.

2.3 Standing Wave Acoustic Levitation

Consider a source radiating sound at a certain frequency, and a reflector placed a distance away from the source. If the distance between the source and the reflector are one of the integer multiples of the half wavelength of sound in air at that frequency, standing wave is obtained between the source and the radiator, and a particle can be trapped at the nodes of the standing wave. The force on a rigid sphere in a gaseous medium is obtained by Wang et al. (1998) in the following fashion.

Now, consider a rigid sphere with radius R trapped in a gas. The incident wave can be expressed as

$$p_i = A \sin kz \ e^{i\omega t} \tag{46}$$

The location $z = 0$ is the location of the pressure node. Using a polar coordinate system, the center of the sphere is located at $z = \zeta$ and the system is aligned such that $\theta = 0$ is aligned with the positive z axis. This alignment makes possible the representation of

$$z = \zeta + x \cos \theta \tag{47}$$

The exponential function can be represented as a series expansion

$$e^{ikx\cos\theta} = \sum_{n=0}^{\infty}(2n+1)i^n j_n(kx)P_n(\cos\theta) \qquad (48)$$

which leads to

$$p_{i0} = A\sin kz = \sum_{n=0}^{\infty}(2n+1)A_n j_n(kx)P_n(\cos\theta) \qquad (49)$$

Where P_n is the Legendere Polynomial, j_n is the spherical Bessel's function of first kind of order n, h_n is the spherical Hankel function of first kind of order n. The A_n multipliers in Equation (49) are

$$A_n = \frac{A}{2i}i^n[e^{ik\zeta} - (-1)^n e^{-ik\zeta}] \qquad (50)$$

There is also scattering from the surface of the sphere. The scattered wave can be defined as

$$p_r = p_{r0}e^{i\omega t} \qquad (51)$$

$$p_{r0} = \sum_{n=0}^{\infty}B_n h_n(kx)P_n(\cos\theta) \qquad (52)$$

37

The scattered wave represents a spherical wave propagating from the center of the sphere in outwards direction. The total sound pressure will be the sum of the incident and scattered waves. At the surface of the sphere, the total sound pressure should result in a zero particle velocity, which is expressed as

$$\left(\frac{\partial p_{i0}}{\partial x}\right)_{x=R} = -\left(\frac{\partial p_{r0}}{\partial x}\right)_{x=R} \tag{53}$$

Applying Equation (53), Equation (54) is obtained with equating the terms with the same n

$$B_n = -A_n \frac{(2n+1)j_n'(kR)}{h_n'(kR)} \tag{54}$$

Knowing that

$$p_0 = p_{i0} + p_{r0} \tag{55}$$

The total sound pressure at the outer radius of the sphere can be written as

$$p_0 = \sum_{n=0}^{\infty} (2n+1)\left[j_n(kR) - \frac{j_n'(kR)h_n(kR)}{h_n'(kR)}\right] A_n P_n(\cos\theta) \tag{56}$$

38

The sphere is assumed to be rigid; hence the compact source assumption $kR \ll 1$ is also valid. For small kR, the total sound pressure will become

$$p_0 = \left[1 - \frac{(kR)^2}{2}\right] A \sin k\zeta + \frac{3}{2}(kR)A \cos k\zeta \, P_1(\cos\theta)$$
$$- \frac{5}{9}(kR)^2 \, A \sin k\zeta \, P_2(\cos\theta) \tag{57}$$

At the surface of the sphere, the normal component of the particle velocity vanishes. The tangential component of the particle velocity is

$$u_\theta = u_{\theta 0} e^{-i\omega t} \tag{58}$$

where

$$u_{\theta 0} = \frac{1}{i\omega\rho_0 R}\frac{\partial p_0}{\partial\theta}$$
$$= \frac{3i}{2}\frac{A}{\rho_0 c_0}\cos k\zeta \, \sin\theta \tag{59}$$
$$- \frac{5i}{3}\frac{kR}{\rho_0 c_0}\frac{A}{\rho_0 c_0}\sin k\zeta \, \cos\theta \, \sin\theta$$

with this information, mean excess pressure at the surface can be written as

39

$$\langle P - P_0 \rangle = \frac{A^2}{4\rho_0 c_0} [\sin^2 k\zeta + \frac{3}{2} kR \sin 2k\zeta \cos \theta$$
$$- \frac{9}{4} \cos^2 k\zeta \sin^2 \theta \qquad (60)$$
$$+ \frac{5}{2} kR \sin 2k\zeta \sin^2 \theta \cos \theta]$$

Now, the mean excess pressure is obtained, the expression for the acoustic radiation stress tensor should be recalled

$$S_{ij} = -\langle P - P_0 \rangle \delta_{ij} - \rho_0 \langle u_i u_j \rangle \qquad (61)$$

The normal component of the particle velocity is zero and due to axisymmetric property, the force acting on the sphere should have only z component. In this case the tensor will be

$$S_{ij} n_j = -\langle P - P_0 \rangle n_i \qquad (62)$$

where $n = -e_x$. For the z axis

$$\boldsymbol{n} \cdot \boldsymbol{e_z} = \cos \theta \qquad (63)$$

And the force will be the result of the surface integral.

$$F_z = \int_S \langle P - P_0 \rangle \cos \theta \, dS \tag{64}$$

or

$$F_z = \int_0^\pi \langle P - P_0 \rangle \cos \theta \, 2 \, \pi \, R^2 \sin \theta \, d\theta \tag{65}$$

The result of the integral will be evaluated as

$$F_z = -\frac{5\pi}{6} \frac{A^2 k R^3}{\rho_0 c_0^2} \sin 2k\zeta \tag{66}$$

For small $k\zeta$, the force becomes

$$F_z = -\frac{5\pi}{6} \frac{A^2 k R^3}{\rho_0 c_0^2} 2k\zeta \tag{67}$$

It should be noted that the force is positive for the negative values of ζ and negative for the positive values of ζ. This property means that the radiation force is acting as a linear spring around the equilibrium position. The small deviations in the equilibrium state could be compensated with the help of the radiation force, hence making the pressure node a stable equilibrium position.

Equation (67) suggests that the force is proportional to the square of the pressure amplitude and the third power of the radius of the object. It can be anticipated that if two objects have the same mass but different densities, the one with lower density has higher chance of being levitated. Hence, the force is inversely proportional with the density of the levitated material.

It is possible to predict the force on a particle in a single axis standing wave acoustic levitation set-up using Equation (67). However, this study under development utilizes a complex set-up with an annular plate as a sound source. Obtaining the expressions for sound pressure due to radiation from annular plate is even a cumbersome process. Hence, the finite element method will be used to predict the sound pressure. The sound pressure can be simulated using COMSOL Multiphysics ® either including both the plate and the air above it or representing the plate by a normal acceleration on the mating surface of the air cavity. The latter is found to be more computationally efficient.

CHAPTER 3

VIBROACOUSTICS OF LEVITATION

In most cases, mechanical vibrations and sound radiation are said to be vibroacoustically coupled. In this study, surrounding air will be excited by mechanical vibrations of designed structures for the purpose of acoustic levitation.

3.1 Axial Vibrations of a Free-Free Rod

Equation of motion for a rod in free axial vibration can be written as follows:

$$EA(x)\frac{\partial^2 v}{\partial x^2} - m(x)\frac{\partial^2 v}{\partial t^2} = 0 \tag{68}$$

Where E is the elastic modulus, $A(x)$ is the area of the rod, $m(x)$ is the mass density of the rod. If the cross section and the density are uniform along the length of the beam, Equation (71) will simplify to

$$E\frac{\partial^2 v}{\partial x^2} = \rho\frac{\partial^2 v}{\partial t^2} \tag{69}$$

43

The displacement v will be of the form

$$v(x,t) = V(x)F(t) \tag{70}$$

where $V(x)$ is the axial displacement and $F(t)$ is the forcing. The differential equation of motion will be

$$E\frac{\partial^2(V(x)F(t))}{\partial x^2} = \rho\frac{\partial^2(V(x)F(t))}{\partial t^2} \tag{71}$$

As the variables are separated, the partial derivative will become ordinary derivative. Each side of Equation (71) will be divided by $\rho U(x)F(t)$, then

$$\frac{1}{\rho V(x)}E\frac{d^2V(x)}{dx^2} = \frac{1}{F(t)}\frac{d^2F(t)}{dt^2} \tag{72}$$

The above equation can be correct only when each side of the equation is equal to a constant. In vibration problems, the constant is taken as $-\omega^2$ to obtain a non-trivial solution. Consider the right side of the Equation (72).

$$\frac{d^2F(t)}{dt^2} + \omega^2F(t) = 0 \tag{73}$$

The solution of the second order ordinary differential equation is

$$F(t) = A_1 \cos(\omega t) + A_2 \sin(\omega t) \qquad (74)$$

Now consider the left side of the Equation (72)

$$\frac{d^2 U(x)}{dx^2} + \frac{\omega^2 \rho}{E} U(x) = 0 \qquad (75)$$

Let

$$\beta^2 = \frac{\omega^2 \rho}{E} \qquad (76)$$

Then,

$$\frac{d^2 V(x)}{dx^2} + \beta^2 V(x) = 0 \qquad (77)$$

Solution for the second order ordinary differential equation will be given by

$$V(x) = B_1 \cos(\beta x) + B_2 \sin(\beta x) \qquad (78)$$

As the solution is obtained, the boundary conditions should be applied for a free-free case. At the both ends, the conditions have to be satisfied as the stress should be equal to zero.

$$\frac{dV(x)}{dx} = -\beta B_1 \sin(\beta x) + \beta B_2 \cos(\beta x) = 0 \qquad (79)$$

Application of the condition at $x = 0$ yields

$$B_2 = 0 \qquad (80)$$

Applying the condition at the end, $x = L$ and knowing that both coefficients cannot be zero results in

$$\sin(\beta L) = 0 \qquad (81)$$

The β values will satisfy the above criterion, for integer n values

$$\beta_n = \frac{n\pi}{L} \qquad (82)$$

and the corresponding natural frequencies will be expressed as

46

$$\omega_n = \sqrt{E/\rho}\,\frac{n\pi}{L} \qquad (83)$$

Knowing that $\sqrt{E/\rho}$ is the speed of sound in the bar, c_0 in a medium, the natural frequencies will be given by

$$\omega_n = c_0 \frac{n\pi}{L} \qquad (84)$$

3.1.1 Axial Vibrations of Stepped Horn Waveguides

Waveguides are used for focusing or amplifying the incident wave excitation. In other words, energy is transferred using a waveguide. Let's consider a bar under axial loading. Equation for natural frequencies in axial motion can be manipulated to give

$$L = \frac{c_0}{f_n}\frac{n}{2} = \lambda_n \frac{n}{2} \qquad (85)$$

Where λ_n denotes the wavelength of sound at f_n. If the bar is tuned to a certain frequency, the length of the bar should be equal to an integer multiple of the half wavelength of the sound in the bar material. The waveguides are designed using bar velocity of sound rather than the bulk velocity of sound. When the diameter is equal to 0.3λ, the error in natural frequency estimations will be about 2% (Ensminger, 2008).

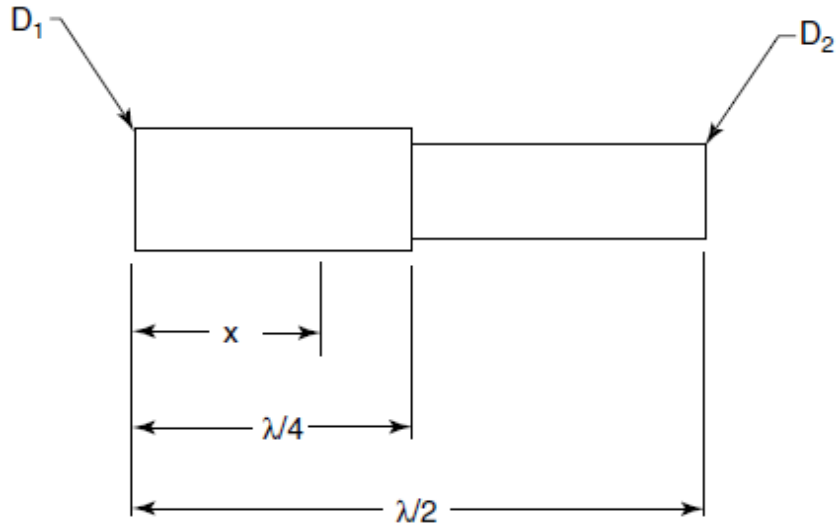Consider a double cylinder waveguide with a step at the middle.

Figure 14 – Stepped horn type waveguide

The displacement, velocity and acceleration can be written, respectively, as

$$v = A \cos\left(\frac{\omega x}{c}\right) \cos(\omega t) \tag{86}$$

$$\frac{dv}{dt} = -\omega A \cos\left(\frac{\omega x}{c}\right) \sin(\omega t) \tag{87}$$

$$\frac{d^2 v}{dt^2} = -\omega^2 A \cos\left(\frac{\omega x}{c}\right) \cos(\omega t) \tag{88}$$

The stress at any point can be expressed as

$$\sigma = \frac{iE}{\omega}\frac{dv}{dx} = iE\frac{\omega A}{c}\sin\left(\frac{\omega x}{c}\right)\sin(\omega t) \tag{89}$$

The mechanical impedance is given by

$$Z = \frac{F}{dv/dt} = \frac{-\sigma S}{dv/dt} = iS\rho c\tan\left(\frac{\omega x}{c}\right) \tag{90}$$

Where σ is the normal stress and S is the area. The large-diameter part of the waveguide will be taken as the input part and the small-diameter part will be the output part. As the waveguide is tuned to have a half wavelength, the maximum displacement of each side will occur at the free ends. At the input part

$$v = v_1\cos\left(\frac{\omega x}{c}\right)\cos(\omega t) \tag{91}$$

$$\frac{dv}{dt} = -\omega v_1\cos\left(\frac{\omega x}{c}\right)\sin(\omega t) \tag{92}$$

$$\frac{d^2v}{dt^2} = -\omega^2 v_1\cos\left(\frac{\omega x}{c}\right)\cos(\omega t) \tag{93}$$

At the output part

$$v = v_2 \cos\left(\frac{\omega(l-x)}{c}\right) \cos(\omega t) \tag{94}$$

$$\frac{dv}{dt} = -\omega v_2 \cos\left(\frac{\omega(l-x)}{c}\right) \sin(\omega t) \tag{95}$$

$$\frac{d^2 v}{dt^2} = -\omega^2 v_2 \cos\left(\frac{\omega(l-x)}{c}\right) \cos(\omega t) \tag{96}$$

The either side of the step should satisfy the following criteria

$$\frac{v_2}{v_1} = \frac{Z_1}{Z_2} = \frac{S_1}{S_2} \tag{97}$$

Then the amplification will simply be expressed by

$$v_2 = \frac{S_1}{S_2} v_1 \tag{98}$$

3.2 Bending Vibrations of Annular Plates

The differential equation of motion for a beam in free bending vibrations is given by

$$D \, \nabla^4 w + \rho h \frac{\partial^2 w}{\partial t^2} = 0 \qquad (99)$$

where D is the flexural rigidity of the plate and w is the transverse displacement of the plate. In polar coordinates, the Laplacian operator is

$$\nabla^2(\cdot) = \frac{\partial^2(\cdot)}{\partial r^2} + \frac{1}{r}\frac{\partial(\cdot)}{\partial r} + \frac{1}{r^2}\frac{\partial^2(\cdot)}{\partial \theta^2} \qquad (100)$$

and the biharmonic operator is

$$\nabla^4 = \nabla^2 \nabla^2 \qquad (101)$$

The displacement can be written in the form

$$w(r, \theta, t) = W(r, \theta)e^{i\omega t} = We^{i\omega t} \qquad (102)$$

Substituting Equation (102) to the differential equation of motion one obtains

$$(\nabla^4 - \beta^4)W = 0 \qquad (103)$$

51

In the equation of motion, the flexural rigidity D is expressed as

$$D = \frac{Eh^3}{12(1 - \nu^2)} \qquad (104)$$

and β is given by

$$\beta^4 = \frac{\rho h \omega^2}{D} \qquad (105)$$

The expanded equation is

$$(\nabla^2 + \beta^2)(\nabla^2 - \beta^2)W = 0 \qquad (106)$$

It can be expressed in two linear differential equations

$$(\nabla^2 + \beta^2)W_1 = 0 \qquad (107)$$

$$(\nabla^2 - \beta^2)W_2 = 0 \qquad (108)$$

where the total solution can be written as

$$W = W_1 + W_2 \tag{109}$$

Using separation of variables, the solution can be expressed as

$$W = R(r)\Theta(\theta) \tag{110}$$

Start solving equation of motion by separation of variables

$$W_1 = W_1(r,\theta) = R_1(r)\Theta_1(\theta) = R_1\Theta_1 \tag{111}$$

$$\Theta_1 \frac{d^2 R_1}{dr^2} + \frac{\Theta_1}{r}\frac{dR_1}{dr} + \frac{R_1}{r}\frac{d^2\Theta_1}{d\theta^2} + \beta^2 R_1\Theta_1 = 0 \tag{112}$$

Multiplying Equation (112) with $\frac{r^2}{R_1\Theta_1}$ and re-arranging

$$r^2\left[\left(\frac{d^2 R_1}{dr^2} + \frac{1}{r}\frac{dR_1}{dr}\right)\frac{1}{R_1} + \beta^2\right] = -\frac{1}{\Theta_1}\frac{d^2\Theta_1}{d\theta^2} \tag{113}$$

Equation (113) can be correct only if either side of the equation is equal to a constant. Equating each side to κ^2, Equations (114) and (115) are obtained.

53

$$\frac{d^2\Theta_1}{d\theta^2} + \kappa^2\Theta_1 = 0 \tag{114}$$

$$\frac{d^2R_1}{dr^2} + \frac{1}{r}\frac{dR_1}{dr} + \left(\beta^2 - \frac{\kappa^2}{r^2}\right)R_1 = 0 \tag{115}$$

Equation (114) has a solution of the form

$$\Theta_1 = G_1 \cos(\kappa\theta) + H_1 \sin(\kappa\theta) \tag{116}$$

With a little manipulation, Equation (115) will take the form where $\tau = \beta r$

$$\frac{d^2R_1}{d\tau^2} + \frac{1}{\tau}\frac{dR_1}{d\tau} + \left(1 - \frac{k^2}{\tau^2}\right)R_1 = 0 \tag{117}$$

This is Bessel's equation with a solution given by

$$R_1 = \bar{A}J_k(\beta r) + \bar{B}Y_k(\beta r) \tag{118}$$

and

$$W_1 = \Theta_1 R_1 \tag{119}$$

The solution to Equation (118) will be similar after β is replaced by $i\beta$

$$(\nabla^2 + (i\beta)^2)W_2 = 0 \tag{120}$$

$$W_2 = W_2(r,\theta) = R_2(r)\Theta_2(\theta) = R_2\Theta_2 \tag{121}$$

After a similar procedure, the solution is obtained as

$$\frac{d^2\Theta_2}{d\theta^2} + \kappa^2\Theta_2 = 0 \tag{122}$$

$$\Theta_2 = G_2\cos(\kappa\theta) + H_2\sin(\kappa\theta) \tag{123}$$

For the other equation in which the replacement is done

$$\frac{d^2R_2}{dr^2} + \frac{1}{r}\frac{dR_2}{dr} + \left((i\beta)^2 - \frac{\kappa^2}{r^2}\right)R_2 = 0 \tag{124}$$

Now taking $\tau = i\beta r$, the solution will be given by

$$R_2 = \bar{C} \, I_\kappa(\beta r) + \bar{D} \, K_\kappa(\beta r) \tag{125}$$

and

$$W_2 = \Theta_2 R_2 \tag{126}$$

As the annular plate has a closed form, the solution should be periodic with 2π. Therefore, the κ values should be integers. The solution will be of the form:

$$
\begin{aligned}
W(r,\theta) = \sum_{n=0}^{\infty} &\{[A_n J_n(\beta r) + B_n Y_n(\beta r) + C_n I_n(\beta r) \\
&+ D_n K_n(\beta r)] \cos(n\theta) \\
&+ [A_n^* J_n(\beta r) + B_n^* Y_n(\beta r) + C_n^* I_n(\beta r) \\
&+ D_n^* K_n(\beta r)] \sin(n\theta)\}
\end{aligned}
\tag{127}
$$

As the boundary conditions are symmetric along the diameter of the plate, one can neglect the series with coefficients $\sin n\theta$ (Leissa, 1969). Therefore, the solution will be of the form:

$$
\begin{aligned}
W_n(r,\theta) = [A_n J_n(\beta r) + B_n Y_n(\beta r) + C_n I_n(\beta r) \\
+ D_n K_n(\beta r)] \cos(n\theta)
\end{aligned}
\tag{128}
$$

The above solution will satisfy the boundary conditions. The bending and twisting moments are expressed as:

$$M_r = -D \left[\frac{\partial^2 W}{\partial r^2} + \nu \left(\frac{1}{r} \frac{\partial W}{\partial r} + \frac{1}{r^2} \frac{\partial^2 W}{\partial \theta^2} \right) \right] \qquad (129)$$

$$M_\theta = -D \left[\frac{1}{r} \frac{\partial W}{\partial r} + \frac{1}{r^2} \frac{\partial^2 W}{\partial \theta^2} + \nu \frac{\partial^2 W}{\partial r^2} \right] \qquad (130)$$

$$M_{r\theta} = -D \left[(1 - \nu) \frac{\partial}{\partial r} \left(\frac{1}{r} \frac{\partial W}{\partial \theta} \right) \right] \qquad (131)$$

The transverse shearing forces are given by

$$Q_r = -D \frac{\partial}{\partial r} \left(\nabla^2 W \right) \qquad (132)$$

$$Q_\theta = -D \frac{1}{r} \frac{\partial}{\partial \theta} \left(\nabla^2 W \right) \qquad (133)$$

The Kelvin-Kirchhoff edge reactions are determined as

$$V_r = Q_r + \frac{1}{r} \frac{\partial M_{r\theta}}{\partial \theta} \qquad (134)$$

$$V_\theta = Q_\theta + \frac{\partial M_{r\theta}}{\partial r} \tag{135}$$

The boundary conditions for an annular plate with both inner and outer edges free are:

$$M_r(b, \theta) = 0 \tag{136}$$

$$V_r(b, \theta) = 0 \tag{137}$$

$$M_r(a, \theta) = 0 \tag{138}$$

$$V_r(a, \theta) = 0 \tag{139}$$

The expressions for necessary quantities to evaluate the boundary conditions are:

$$M_r(r, \theta) = -D\left[\left(A_n J_n''(\beta r) + B_n Y_n''(\beta r) + C_n I_n''(\beta r)\right.\right.$$
$$\left. + D_n K_n''(\beta r)\right)$$
$$+ \frac{\nu}{r}\left(A_n J_n'(\beta r) + B_n Y_n'(\beta r) + C_n I_n'(\beta r)\right.$$
$$\left. + D_n K_n'(\beta r)\right)$$
$$- n^2\frac{\nu}{r^2}\left(A_n J_n(\beta r) + B_n Y_n(\beta r) + C_n I_n(\beta r)\right.$$
$$\left.\left. + D_n K_n(\beta r)\right)\right]\cos(n\theta)$$

(140)

$$M_{r\theta}(r, \theta) = -D(1$$
$$- \nu)\left[n\frac{1}{r^2}\left(A_n J_n(\beta r) + B_n Y_n(\beta r) + C_n I_n(\beta r)\right.\right.$$
$$\left. + D_n K_n(\beta r)\right)$$
$$- n\frac{1}{r}\left(A_n J_n'(\beta r) + B_n Y_n'(\beta r) + C_n I_n'(\beta r)\right.$$
$$\left.\left. + D_n K_n'(\beta r)\right)\right]\sin(n\theta)$$

(141)

$$\nabla^2 W = \left[\left(A_n J_n''(\beta r) + B_n Y_n''(\beta r) + C_n I_n''(\beta r) + D_n K_n''(\beta r)\right)\right.$$
$$+ \frac{1}{r}\left(A_n J_n'(\beta r) + B_n Y_n'(\beta r) + C_n I_n'(\beta r)\right.$$
$$\left. + D_n K_n'(\beta r)\right)$$
$$- n^2\frac{1}{r^2}\left(A_n J_n(\beta r) + B_n Y_n(\beta r) + C_n I_n(\beta r)\right.$$
$$\left.\left. + D_n K_n(\beta r)\right)\right]\cos(n\theta)$$

(142)

$$Q_r(r,\theta) = -D\left[\left(A_n J_n'''(\beta r) + B_n Y_n'''(\beta r) + C_n I_n'''(\beta r)\right.\right.$$

$$\left.+ D_n K_n'''(\beta r)\right)$$

$$-\frac{1}{r^2}\left(A_n J_n'(\beta r) + B_n Y_n'(\beta r) + C_n I_n'(\beta r)\right.$$

$$\left.+ D_n K_n'(\beta r)\right)$$

$$+\frac{1}{r}\left(A_n J_n''(\beta r) + B_n Y_n''(\beta r) + C_n I_n''(\beta r)\right.$$

$$\left.+ D_n K_n''(\beta r)\right)$$

$$\tag{143}$$

$$- n^2 \frac{2}{r^3}\left(A_n J_n(\beta r) + B_n Y_n(\beta r) + C_n I_n(\beta r)\right.$$

$$\left.+ D_n K_n(\beta r)\right)$$

$$+ n^2 \frac{1}{r^2}\left(A_n J_n'(\beta r) + B_n Y_n'(\beta r) + C_n I_n'(\beta r)\right.$$

$$\left.\left.+ D_n K_n'(\beta r)\right)\right]\cos(n\theta)$$

$$V_r(r,\theta) = Q_r(r,\theta) + \frac{1}{r} D (1-v) n^2 \left[-\frac{1}{r^2}\left(A_n J_n(\beta r) + \right.\right.$$

$$B_n Y_n(\beta r) + C_n I_n(\beta r) + D_n K_n(\beta r)\right) + \frac{1}{r}\left(\left(A_n J_n'(\beta r) + \right.\right. \tag{144}$$

$$\left.\left.\left. B_n Y_n'(\beta r) + C_n I_n'(\beta r) + D_n K_n'(\beta r)\right)\right)\right]\cos(n\theta)$$

There are four equations coming from the boundary conditions and four unknowns appearing as the coefficients of the Bessel functions. They can be re-arranged to be put in a matrix form as follows:

$$M_r(r,\theta) = -D\cos(n\theta)\left[A_n M_A(\beta r) + B_n M_B(\beta r)\right.$$

$$\left.+ C_n M_C(\beta r) + D_n M_D(\beta r)\right] \tag{145}$$

where

$$M_A(\beta r) = J_n''(\beta r) + \frac{\kappa}{r} J_n'(\beta r) - n^2 \frac{\kappa}{r} J_n(\beta r) \tag{146}$$

$$M_B(\beta r) = Y_n''(\beta r) + \frac{\kappa}{r} Y_n'(\beta r) - n^2 \frac{\kappa}{r} Y_n(\beta r) \tag{147}$$

$$M_C(\beta r) = I_n''(\beta r) + \frac{\kappa}{r} I_n'(\beta r) - n^2 \frac{\kappa}{r} I_n(\beta r) \tag{148}$$

$$M_D(\beta r) = K_n''(\beta r) + \frac{\kappa}{r} K_n'(\beta r) - n^2 \frac{\kappa}{r} K_n(\beta r) \tag{149}$$

It should be noted that the functions are also functions of n, which determines the order of the Bessel functions.

$$V_r(r, \theta) = -D \cos(n\theta) \left[A_n V_A(\beta r) + B_n V_B(\beta r) + C_n V_C(\beta r) \right. \\ \left. + D_n V_D(\beta r) \right] \tag{150}$$

where

$$V_A(\beta r) = -\left(J_n'''(\beta r) - \frac{1}{r^2}J_n'(\beta r) + \frac{1}{r}J_n''(\beta r)\right)$$

$$+ n^2\left(\frac{2}{r^3}J_n(\beta r) - \frac{1}{r^2}J_n'(\beta r)\right) \tag{151}$$

$$+ \frac{1}{r}(1-\kappa)n^2\left(-\frac{1}{r^2}J_n(\beta r) + \frac{1}{r}J_n'(\beta r)\right)$$

$$V_B(\beta r) = -\left(Y_n'''(\beta r) - \frac{1}{r^2}Y_n'(\beta r) + \frac{1}{r}Y_n''(\beta r)\right)$$

$$+ n^2\left(\frac{2}{r^3}Y_n(\beta r) - \frac{1}{r^2}Y_n'(\beta r)\right) \tag{152}$$

$$+ \frac{1}{r}(1-\kappa)n^2\left(-\frac{1}{r^2}Y_n(\beta r) + \frac{1}{r}Y_n'(\beta r)\right)$$

$$V_C(\beta r) = -\left(I_n'''(\beta r) - \frac{1}{r^2}I_n'(\beta r) + \frac{1}{r}I_n''(\beta r)\right)$$

$$+ n^2\left(\frac{2}{r^3}I_n(\beta r) - \frac{1}{r^2}I_n'(\beta r)\right) \tag{153}$$

$$+ \frac{1}{r}(1-\kappa)n^2\left(-\frac{1}{r^2}I_n(\beta r) + \frac{1}{r}I_n'(\beta r)\right)$$

$$V_D(\beta r) = -\left(K_n'''(\beta r) - \frac{1}{r^2}K_n'(\beta r) + \frac{1}{r}K_n''(\beta r)\right)$$

$$+ n^2\left(\frac{2}{r^3}K_n(\beta r) - \frac{1}{r^2}K_n'(\beta r)\right) \tag{154}$$

$$+ \frac{1}{r}(1-\kappa)n^2\left(-\frac{1}{r^2}K_n(\beta r) + \frac{1}{r}K_n'(\beta r)\right)$$

With this information, the boundary conditions will yield the following equation system

$$-D\cos(n\theta)\begin{bmatrix} M_A(\beta b) & M_B(\beta b) & M_C(\beta b) & M_D(\beta b) \\ V_A(\beta b) & V_B(\beta b) & V_c(\beta b) & V_D(\beta b) \\ M_A(\beta a) & M_B(\beta a) & M_C(\beta a) & M_D(\beta a) \\ V_A(\beta a) & V_A(\beta a) & V_C(\beta a) & V_D(\beta a) \end{bmatrix}\begin{bmatrix} A_n \\ B_n \\ C_n \\ D_n \end{bmatrix} = 0 \quad (155)$$

The frequencies that make the determinant of the 4×4 matrix equal to zero are the natural frequencies of the annular plate.

$$\begin{vmatrix} M_A(\beta b) & M_B(\beta b) & M_C(\beta b) & M_D(\beta b) \\ V_A(\beta b) & V_B(\beta b) & V_c(\beta b) & V_D(\beta b) \\ M_A(\beta a) & M_B(\beta a) & M_C(\beta a) & M_D(\beta a) \\ V_A(\beta a) & V_A(\beta a) & V_C(\beta a) & V_D(\beta a) \end{vmatrix} = 0 \qquad (156)$$

The procedure to obtain natural frequencies for given properties of the plate is cumbersome if the properties are to be found for given frequencies. Therefore, the finite element method is used to determine the dynamic characteristics of the plate.

Equations obtained here are valid for the free-inside-free-outside boundary conditions of the plate. However, in the actual case the plate is connected to the waveguides, waveguides are connected to the transducers and the whole assembly is fixed at the flanges of the waveguides. To predict the natural frequencies and mode shapes of the set-up, all of the assembly should be analytically modeled. The whole set-up contains different materials, holes and complex shapes.

Although the equations obtained in this section are not sufficient to model the behavior of the plate in this set-up, they provide background and show modeling path for the representation of the plate in the simulations.

CHAPTER 4

DESIGN AND IMPLEMENTATION

The set-up will consist of an annular plate, a concave reflector parallel to the plate and the transducer-waveguide assembly as explained before,. The first design step will be the design of the plate. Then, the waveguide will be designed in such a way that it has an axial mode at a frequency for which the plate has a bending mode. The last step will be the design of the reflector to concentrate and amplify the sound pressure in the levitation region. The transducer is already available, so the target frequencies will be around $20\ kHz$.

4.1 Annular Plate

An expression has been developed for the natural frequencies of an annular plate in chapter 3.

$$\begin{vmatrix} M_A(\beta b) & M_B(\beta b) & M_C(\beta b) & M_D(\beta b) \\ V_A(\beta b) & V_B(\beta b) & V_C(\beta b) & V_D(\beta b) \\ M_A(\beta a) & M_B(\beta a) & M_C(\beta a) & M_D(\beta a) \\ V_A(\beta a) & V_A(\beta a) & V_C(\beta a) & V_D(\beta a) \end{vmatrix} = 0 \qquad (157)$$

This equation contains lengthy and complex expressions including Bessel functions and their derivatives. Calculating the dimensions of a plate for a given frequency will be extremely cumbersome.

Availability of material and ease of manufacturing are other issues to be considered. Material of the plate is selected to be Al5754 with the modulus of elasticity $E = 69\ GPa$ and density $\rho = 2.66\ kg/m^3$. The most common available thickness of the plate is $3\ mm$. The width of the plate is once determined to be $40\ mm$ initially for visualization purposes. A study is conducted in COMSOL Multiphysics ® to disclose bending characteristics of the plate. In the model, a cross section of the plane is built and revolved around the central axis. The plate is meshed with "free tetrahedral" option with the given parameters.
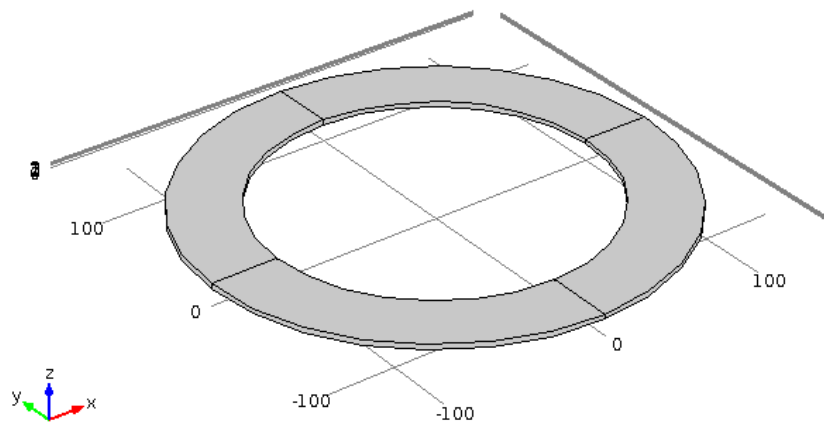
Figure 15 – Model of the plate in COMSOL Multiphysics ®

Element Size Parameters

Maximum element size:

| 3.5 | mm |

Minimum element size:

| 0.054 | mm |

Maximum element growth rate:

| 1.3 |

Resolution of curvature:

| 0.2 |

Resolution of narrow regions:

| 1 |

Figure 16 – Mesh properties of the plate
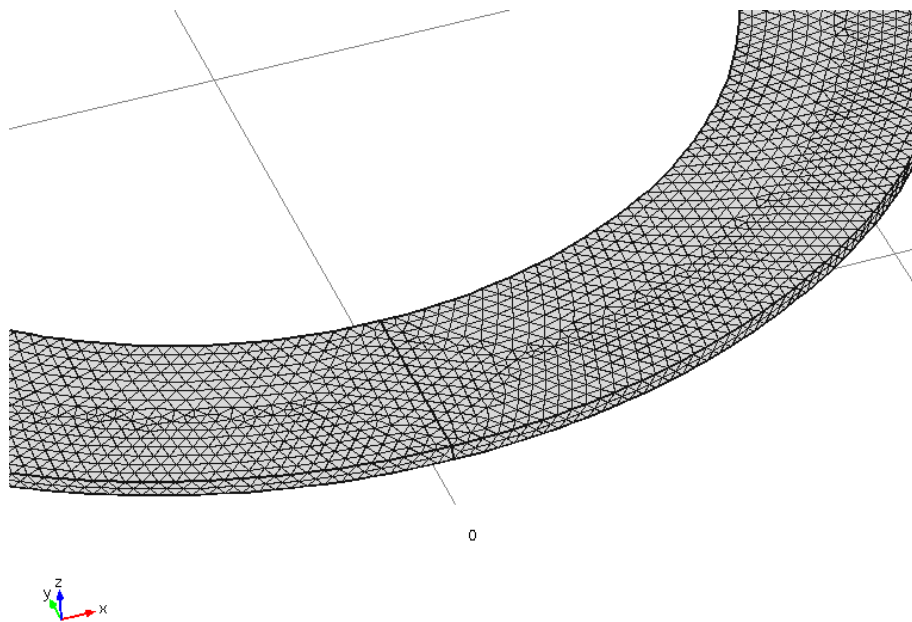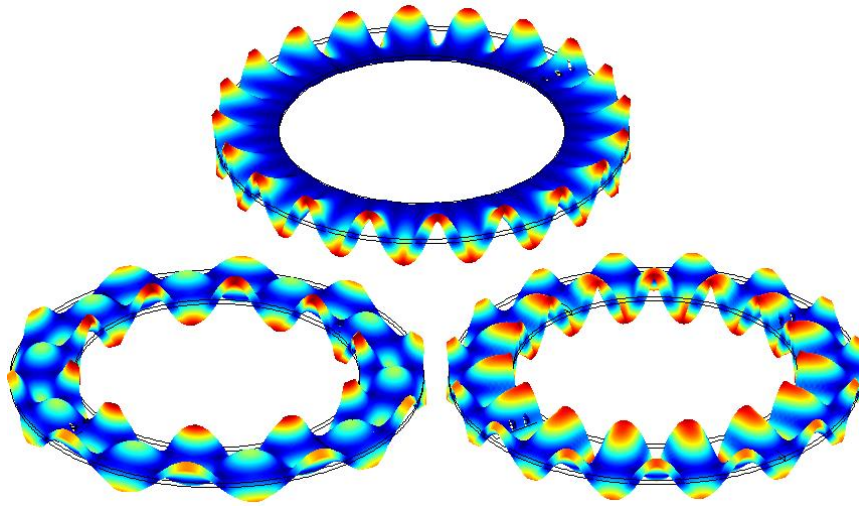

Figure 17 – Meshed view of the plate

Figure 18 - Bending modes of the annular plate

It is seen from the simulations that three radial patterns are repeated over successive modes. As the modal frequency increases, number of modal radii also increases. The modes of the plate will be denoted by a letter for ease of comparison. The top one will be type A, the bottom left will be type B and the bottom right will be type C. The radial normalized harmonic vibration distributions of the corresponding modes are given.
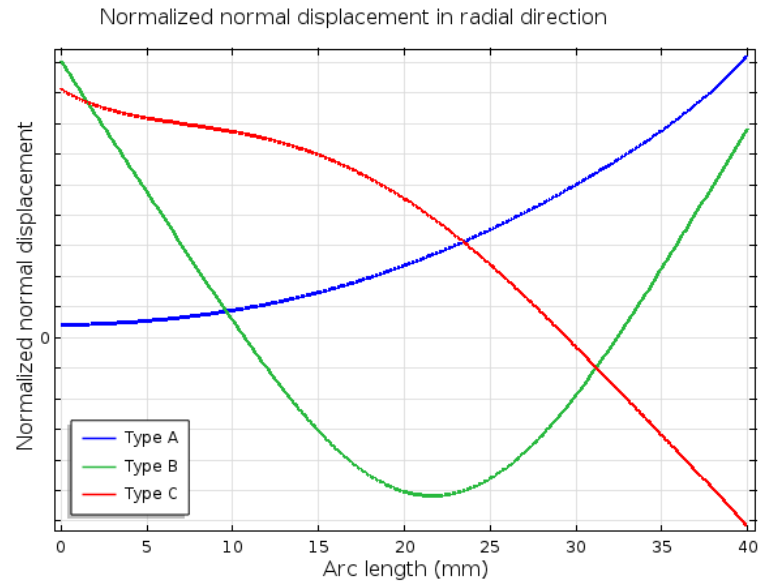
Figure 19 – Harmonic displacement distributions of different types of modes
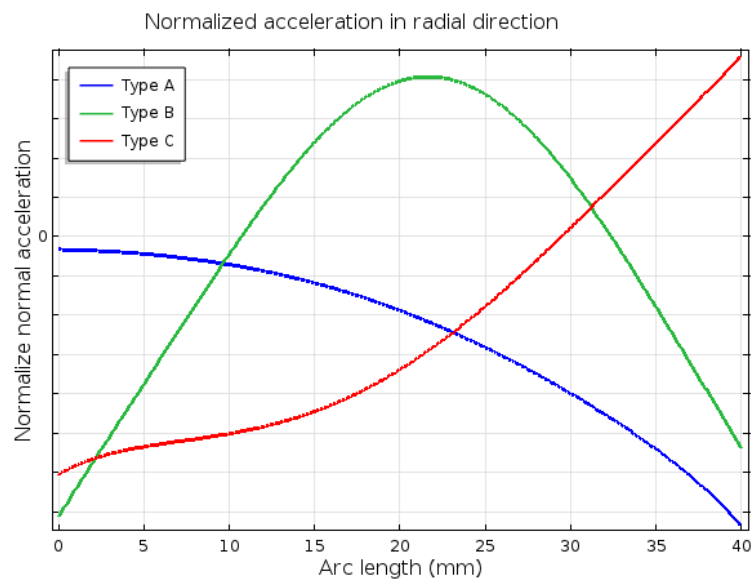
Figure 20 – Harmonic acceleration distributions of different types of modes

Type A modes provide the maximum acceleration and displacement on the outer edge of the plate. They do not include any nodal circle. Type B modes provide the maximum acceleration and displacement near the middle of the plate. They thus

include two nodal circles. Type C modes have one nodal circle, providing the maximum acceleration and displacement at both edges. The distributions obtained in COMSOL Multiphysics ® are exported and a curve fitting operation is done in MATLAB ® to represent the accelerations as functions of radial distance. In these operations, the maximum value of the corresponding distribution is equated to unity and the inner end of the plate is taken as origin. The following representations are obtained for corresponding distributions. In the curve fitting operations, polynomial fits of nine or higher degrees have coefficients of the order 10^{-17}. As the order of the polynomial increase, the correlation coefficient increased. Eighth order polynomials are found to successfully represent the data.

Table 1 – The curve fit parameters for the normalized displacement

$Coeff$	$Disp\ (A)$	$Disp\ (B)$	$Disp\ (C)$
x^0	0.0444	0.9998	0.9999
x^1	0.001	-0.1009	-0.0408
x^2	4.4×10^{-4}	0.0026	0.0052
x^3	-1.5×10^{-5}	-3.7×10^{-4}	-4.1×10^{-4}
x^4	2.3×10^{-6}	2.2×10^{-7}	1.7×10^{-5}
x^5	-1.3×10^{-7}	-3.6×10^{-7}	-5.6×10^{-7}
x^6	4.5×10^{-9}	-1.8×10^{-9}	1.2×10^{-8}
x^7	-8.8×10^{-11}	7.3×10^{-11}	-1.4×10^{-10}
x^8	7.4×10^{-13}	-2.5×10^{-13}	5.3×10^{-13}
$r_{corr.}$	1.000	1.000	1.000

Table 2 - The curve fit parameters for the normalized acceleration

$Coeff$	Acc (A)	Acc (B)	Acc (C)
x^0	-0.0444	-1.000	-1.0002
x^1	-0.001	0.1014	0.041
x^2	-4.3×10^{-4}	-0.0028	-0.0053
x^3	1.2×10^{-5}	4.1×10^{-4}	4.3×10^{-4}
x^4	-1.9×10^{-6}	-2.6×10^{-5}	-1.9×10^{-5}
x^5	1.0×10^{-7}	5.1×10^{-7}	6.3×10^{-7}
x^6	-3.5×10^{-9}	-2.2×10^{-9}	-1.4×10^{-8}
x^7	7.0×10^{-11}	-1.6×10^{-11}	1.7×10^{-10}
x^8	-6.1×10^{-13}	-7.1×10^{-14}	-7.0×10^{-13}
$r_{corr.}$	0.9999	1.000	1.000

Eighth order polynomials were found to be sufficient to represent the corresponding distributions as seen from the correlation coefficients obtained. The polynomial forms will be used in simulations in which the pressure distribution between the plate and the reflector will be obtained. The polynomial distributions obtained are plotted.
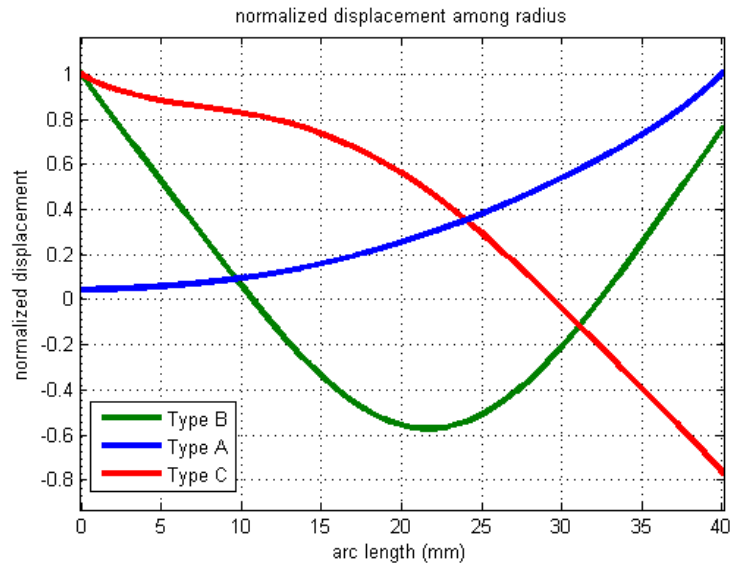
Figure 21 – Polynomial representations of normalized displacement
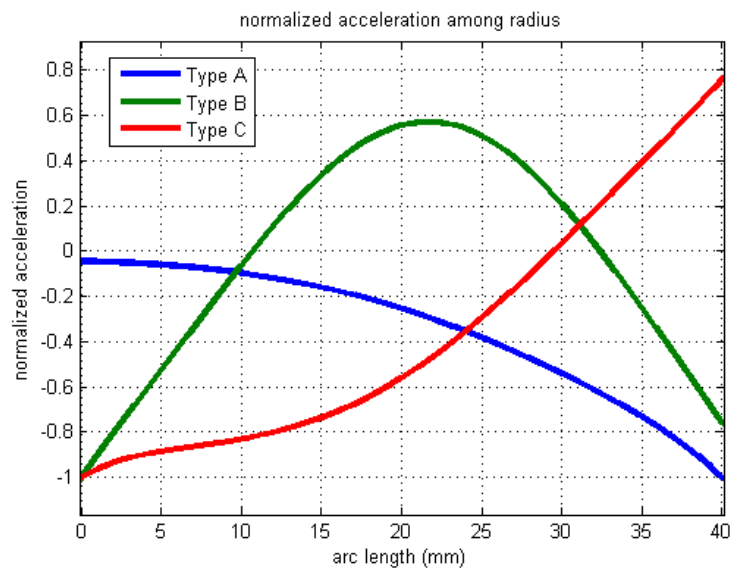
Figure 22 – Polynomial representations of normalized acceleration

Natural frequencies of the plate for different values of inner radius are listed in Table 3. The superscripts on the frequencies represent the corresponding type of mode shape. The study is conducted using COMSOL Multiphysics ® with the

previous mesh properties. Ten natural frequencies are searched around $20\ kHz$ for each value of inner radius.

Table 3 – Natural frequencies around $20\ kHz$ for different inner radii

Inner radius (mm)	Natural Frequencies (Hz)
50	$20463^A, 21257^B, 21306^C$
55	$18970^C, 19772^B, 20911^A$
60	$18962^A, 19693^C, 20770^B$
65	$19436^A, 19564^B, 20336^C$
70	$19870^A, 20456^B, 20904^C$
75	$19012^C, 19420^B, 20262^A, 21277^B$
80	$19566^C, 20224^B, 20627^A$
85	$19072^A, 19372^B, 20069^C, 20960^A$
90	$19437^A, 20082^B, 20528^C$
95	$19278^B, 19778^A, 20768^B, 20950^C$
100	$19422^C, 19966^B, 20096^A,$

The transducers purchased have a design operating frequency of $20 \pm 0.5\ kHz$. Therefore, it would be preferable to have natural frequencies in that range for more efficient use of transducers. However, these frequencies are expected to shift a little after assembling with the waveguides. As there are many configurations that contain natural frequencies in the design range, the mode shapes should be compared and the most prospective of the modes will be targeted. The sound pressure distributions of each mode are simulated in COMSOL Multiphysics ® for a frequency of $20\ kHz$. In the simulation, normalized acceleration distributions are used. A rectangle is developed to represent a section of the plate. The bottom edge of the rectangle will be the face of the plate; the top edge will be the reflector. The left and right sides will just allow the radiation of sound. Table 4 summarizes the geometrical properties of the simulation.

Table 4 – Properties of the simulation section

Property	Value
Frequency	$20\ kHz$
Acoustical Wavelength in air at 20 C	$17.15\ mm$
Width of section	$40\ mm$
Number of nodes	3
Height of section	$25.725\ mm$

The vibration of the plate is represented as the normal acceleration. To represent the mode shape, previously obtained eighth degree polynomials are used. The acceleration distributions are normalized such that each has a maximum value of unity. The maximum acoustic pressure and pressure distribution should be compared and evaluated in order to favor one type of mode. Mesh properties for the simulation are given where $lam0$ corresponds to the wavelength at the excitation frequency.

Figure 23 – 2d mesh parameters in COMSOL Multiphysics ®

The pressure distributions for the three types of modes are given in Figures from 24 to 26.
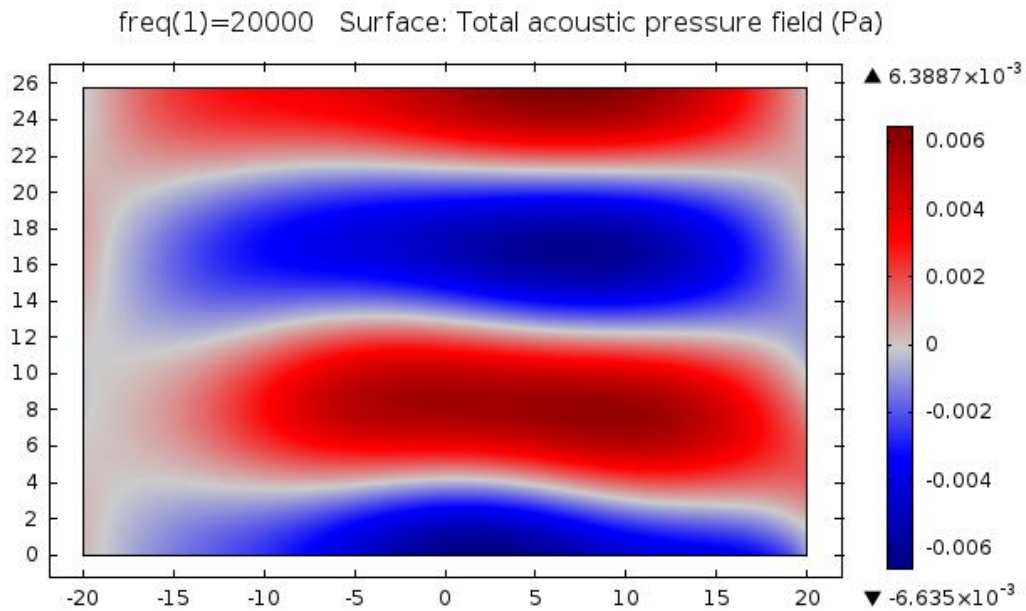
Figure 24 – Pressure distribution of a type A mode with flat reflector
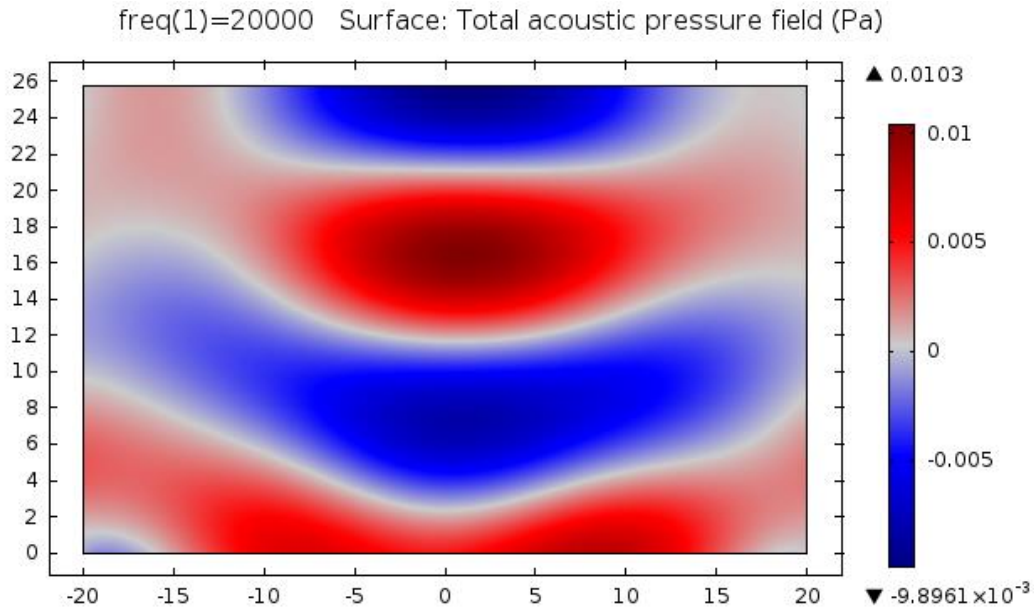
Figure 25 – Pressure distribution of a type B mode with flat reflector
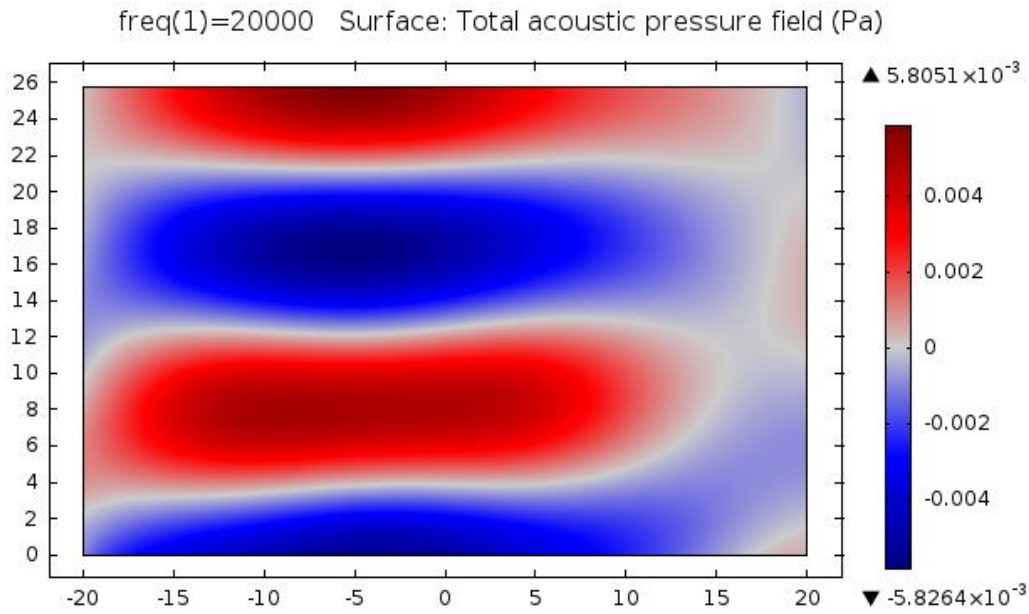
Figure 26 – Pressure distribution of a type C mode with flat reflector

It is clear from the simulations that type B and type A of modes cause higher sound pressure levels in respective order. The corresponding frequencies are closest to $20 \, kHz$ when the inner radius is $100 \, mm$. Therefore, the inner radius of the plate is chosen to be $100 \, mm$ while its thickness is $3 \, mm$ and outer radius is $140 \, mm$. The properties of the plate are listed in Table 5.

Table 5 – Properties of the annular plate

Property	*Value*
Inner radius	$100 \, mm$
Outer radius	$140 \, mm$
Thickness	$3 \, mm$
Material	$Al5754$

The corresponding type A and type B modes of the plate are shown in Figures 27 and 28.
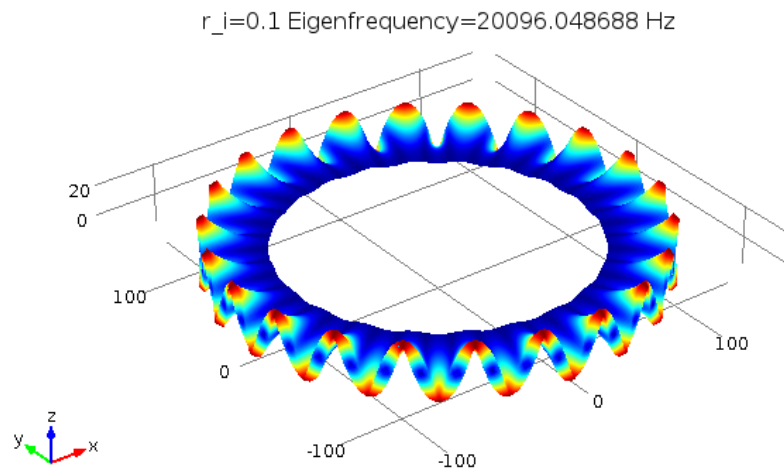
Figure 27 – Type A mode
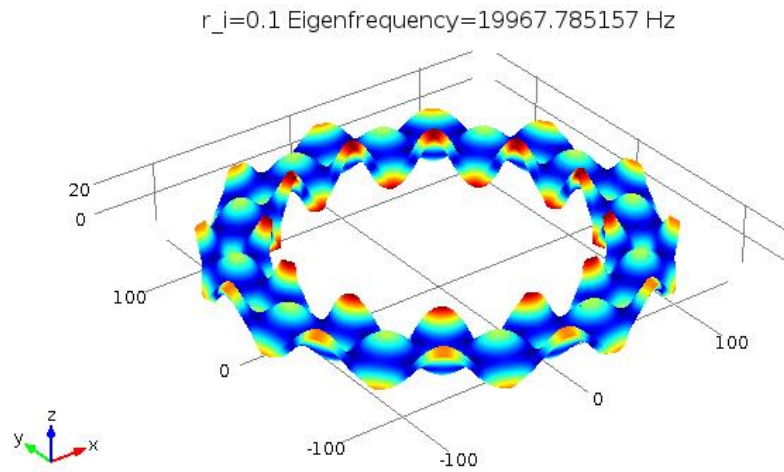
Figure 28 – Type B mode

Both modes are symmetric around the x and y axes on the defined coordinate system. The plate will be excited by the waveguides on the locations of one of the symmetry axes. As both locations are expected to be in the same phase, the excitations will be in phase too. The connection to the waveguides will be realized via three $M5$ bolts. As material is removed, a slight increase in natural frequencies is expected. The technical drawing of the plate is given in the Appendix A.

4.2 Waveguide

The transducers used in this set-up are selected to be MPI-5050F-20L transducers by the MPI Interconsulting Company. Working frequency of the transducers is $20 \pm 0.5\ kHz$ and the diameter of the transducers is $50\ mm$. Therefore, the waveguides should have a base diameter $50\ mm$. The output part of the waveguide will be of rectangular cross section to excite the plate more uniformly in the radial direction. The transition in the waveguide will be a step. The material of the waveguide will be Al7075. Properties of the material are given in Table 6.

Table 6 – Properties of the waveguide material

Property	*Value*
Material	Al7075
Young's Modulus	$70\ GPa$
Density	$2800\ kg/m^3$
Speed of sound	$5000\ m/s$

With the information, if the waveguide is to be tuned to $20000\ Hz$, the length can be found from:

$$L = \frac{c_0}{f_n}\frac{n}{2} = \lambda_n \frac{n}{2} \tag{158}$$

The waveguide will include one half-wavelength to have a node in the middle. Therefore, the length is found to be:

$$L = \frac{c_0}{f_n}\frac{n}{2} = \frac{5000}{20000}\frac{1}{2} = 0.125 \ m \tag{159}$$

The rectangular cross section of the output is selected to be a $30 \ mm \times 10 \ mm$ rectangle to be fit to the annular plate. Three $M5$ bolts will provide connection to the plate, which mainly determined the dimensions of the output section. The connection to the transducer is made through a $M10$ bolt. Therefore, a hole of $10 \ mm$ diameter and $27 \ mm$ depth is created at the interface. As the holes are at the ends of the waveguide, the sections at which the maximum amplitude of vibrations occurs, they should be included in the calculations. There will be a flange at the transition to fix the waveguide (the flange is counted in the base part). In the simulations, the flange is taken to be fixed. The thickness of the flange is $5 \ mm$ and its diameter is $70 \ mm$.
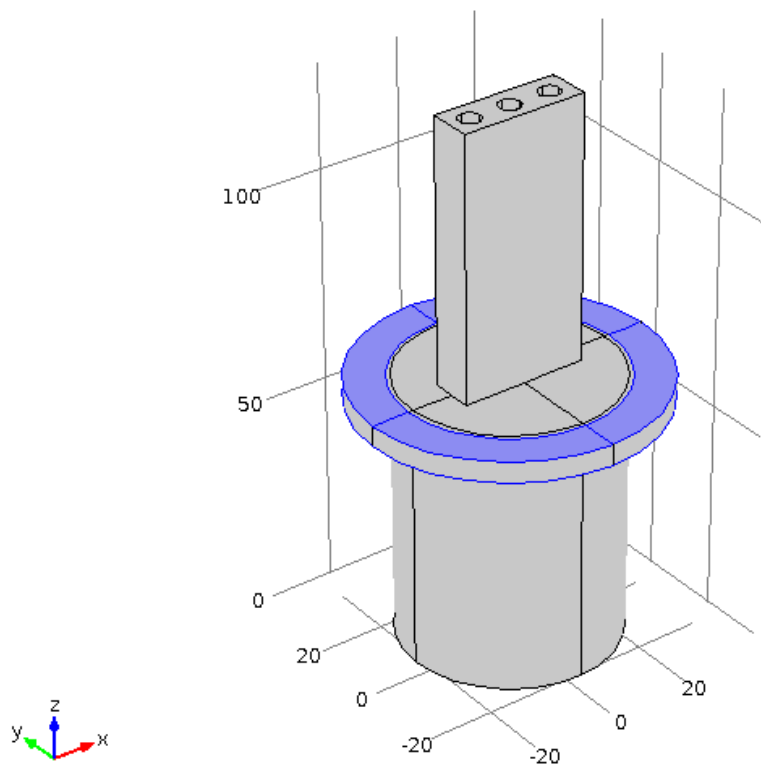
Figure 29 – Model of the waveguide with fixed locations highlighted

A simulation study is conducted using the calculated parameters. The total length is $125\ mm$ where input and output sections are $67.5\ mm$ long each. The connection holes are included. The mesh parameters are given in Figure 30.

Element Size Parameters

Maximum element size:

```
3
```
mm

Minimum element size:

```
0.5
```
mm

Maximum element growth rate:

```
1.4
```

Resolution of curvature:

```
0.4
```

Resolution of narrow regions:

```
0.7
```

Figure 30 – Mesh parameters of the waveguide
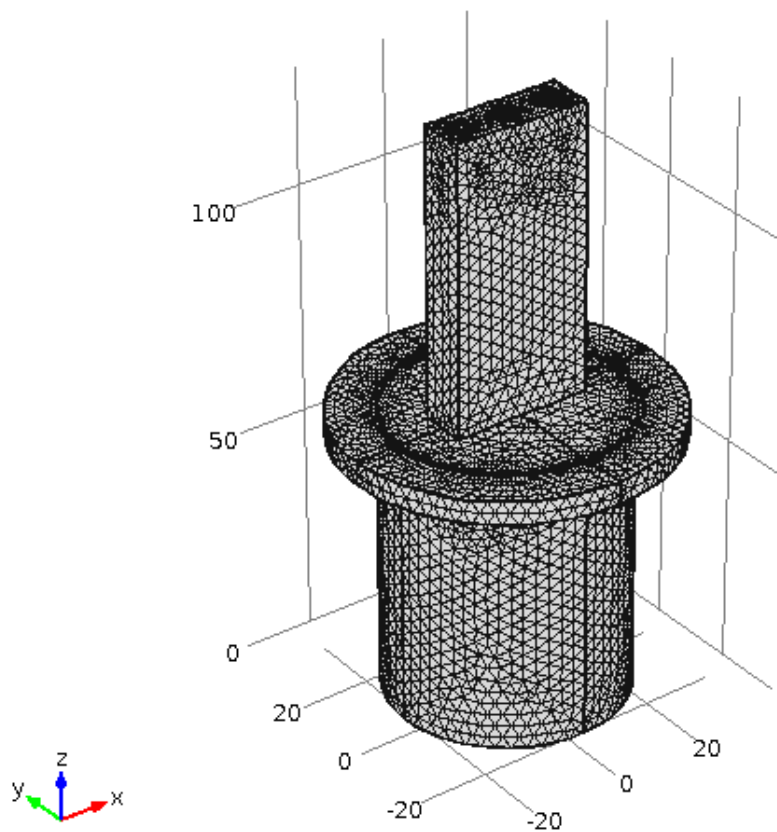
Figure 31 – Meshed view of the waveguide

The simulation resulted in a natural frequency different than the design frequency. As some material is removed at the ends of the waveguide, an increase in the natural frequency was definitely expected.
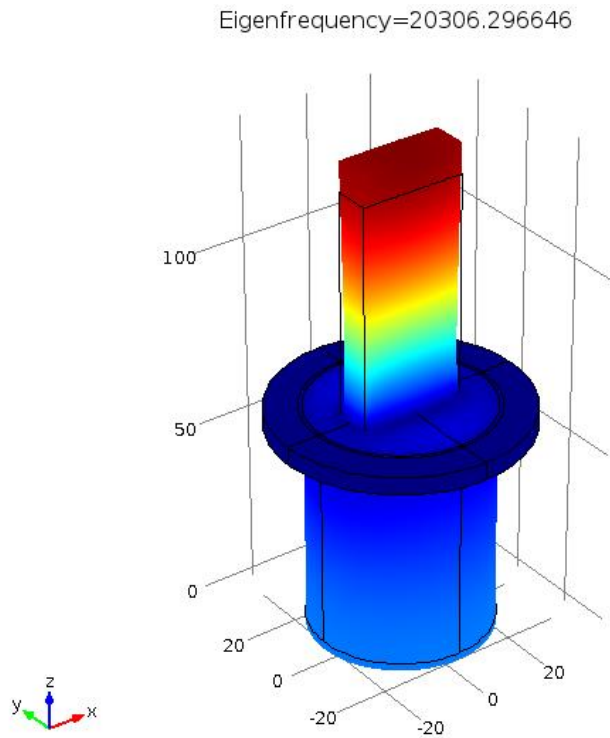
Figure 32 – Result of the first simulation

The initial simulation indicates that the useful axial mode of the waveguide is present. An iterative path should be followed to tune the waveguide to $20\ kHz$. The waveguide definitely has a different natural frequency than expected due to transition and material removal. The desired and obtained frequencies are to be noted and an interpolation or extrapolation will be applied to find the designation frequency to tune the waveguide to $20\ kHz$. In the simulations, the resulting lengths for a given frequency are rounded up to take the effects of accuracy in manufacturing into account. All of the lengths are rounded to an order of $0.01\ mm$. Table 7 lists the design frequencies and the obtained natural frequencies.

Table 7 – Initial frequency vs natural frequency

Initial Frequency (Hz)	Natural Frequency (Hz)
20000	20306
19000	19310
19500	19810
19250	19558
19750	20058

Table 7 suggests that the initial design frequency should be between $19500\,Hz$ and $19750\,Hz$. Interpolation from the data gives $19691\,Hz$ as the initial frequency to obtain desired frequency. The result obtained for a design frequency of $19691\,Hz$ is given in Figure 33. It should be noted that the displacement output is given as mass normalized by the software in all eigenfrequency studies.
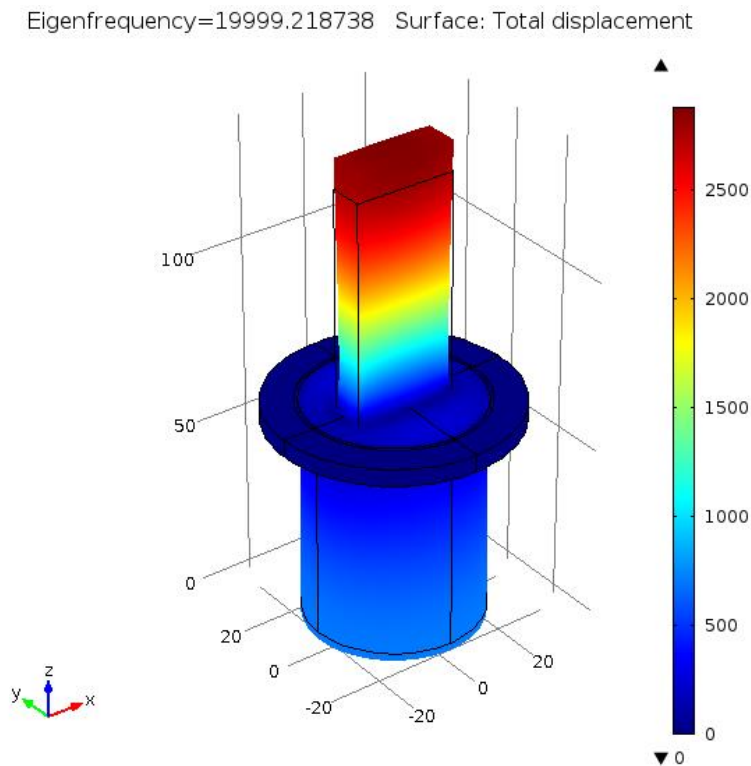
Figure 33 – Waveguide tuned to $20\,kHz$

The ratio of the area of the input to the area of output will be the amplification factor. With this design, the raw area of the base is

$$A_{base}^{raw} = \pi \times r_{base}^2 = \pi \times (25\ mm)^2 = 1.963 \times 10^3\ mm^2 \quad (160)$$

The raw area of the tip is

$$A_{tip}^{raw} = w_{tip} \times b_{tip} = 30\ mm \times 10\ mm = 300\ mm^2 \quad (161)$$

The area of the hole at the base

$$A_{base}^{hole} = \pi \times r_{bhole}^2 = \pi \times (5\ mm)^2 = 78.54\ mm^2 \quad (162)$$

Total area of the holes at the tip (as there are three holes)

$$A_{tip}^{hole} = 3 \times \pi \times r_{thole}^2 = 3 \times \pi \times (2.5\ mm)^2$$
$$= 58.905\ mm^2 \quad (163)$$

The total areas of the tip and the base are respectively:

$$A_{tip} = A_{tip}^{raw} - A_{tip}^{hole} = 241.095\ mm^2 \quad (164)$$

$$A_{base} = A_{base}^{raw} - A_{base}^{hole} = 1.885 \times 10^3\ mm^2 \quad (165)$$

The ratio of the base area to the tip area will give the theoretical amplification factor

$$r_{amp} = \frac{A_{base}}{A_{tip}} = 7.818 \qquad (166)$$

The theoretical amplification factor was estimated assuming uniform cross sections among input and output sections. The sharp transition between sections is also not considered. A more accurate amplification factor can be found from measuring the calculated displacements of input of output surfaces in the simulation. The properties of the waveguides can be summarized in Table 8. The amplification factor from the simulation is found out to be:

$$r_{amp} = \frac{d_{out}}{d_{in}} = \frac{2864}{704} = 4.068 \qquad (167)$$

Table 8 – Properties of the waveguide

Property	Value
Length	$126.96 \ mm$
Length of the base	$63.48 \ mm$
Length of the tip	$63.48 \ mm$
Base diameter	$50 \ mm$
Tip dimensions	$30 \ mm \times 10 \ mm$
Base connection hole	$M10 \times 27 \ mm$
Tip connection holes (3 holes)	$M5 \times 15 \ mm$
Base area	$1885 \ mm^3$
Tip area	$241.095 \ mm^3$
Amplification	4.068
Flange diameter	$70 \ mm$
Flange thickness	$5 \ mm$
Material	$Al7075$

The technical drawing of the waveguide is illustrated in Appendix B.

4.3 Transducer

As mentioned in the previous section, the transducers purchased have a working frequency of $20 \pm 0.5 \, kHz$. The diameter of the transducers is $50 \, mm$ and the transducers are of Langevin type.

Langevin type transducers utilize an even number of piezoceramic disks sandwiched between metal masses. The transducers are tuned to a certain frequency, and at resonance it will include a half wavelength at the resonance frequency. Masses at each side include quarter wavelengths. As long as their length is equal to the quarter wavelength, there is no restriction of material. A representation of a langevin type transducer is given in Figure 34.
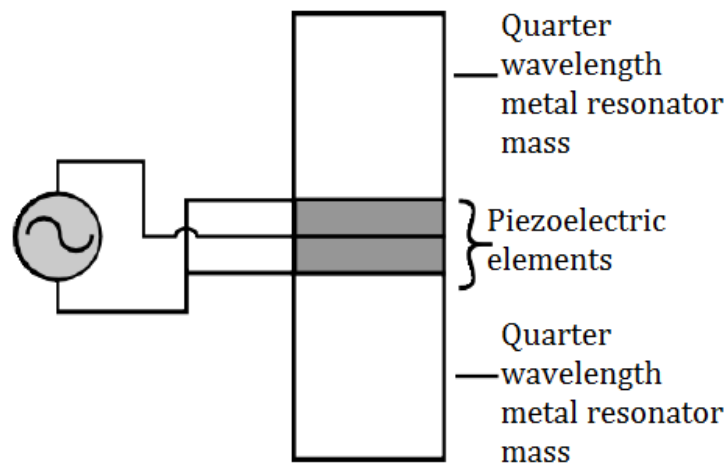
Figure 34 – Sketch of a Langevin type transducer

In this type of configuration, the maximum amplitude of vibrations occurs at the top and the bottom surfaces of the transducer. The top and bottom faces vibrate at opposite phases. The piezoceramic disks are the source of vibration, electrical voltage is applied to the surfaces at a certain frequency and the disks will yield vibration response.

Figure 35 – The transducer used in the set-up

The piezoelectric ceramics included in the transducers are Lead Zirconate Titanate (PZT-8) ceramics. The front metal mass is $Al7075$. The masses and ceramics are assembled with a $M20$ bolt. The connection to the waveguide will be with a $M10$ bolt at the output face. Datasheet of the transducer is given in Appendix C.

4.4 Plate and Waveguides

Although the plate and waveguides are designed separately, they will operate in an assembly. Therefore, the natural frequencies of the assembly will count rather than the natural frequency of each sub element by itself. The simulation of the assembly is carried in COMSOL Multiphysics ®. The geometry file of the waveguide is exported from the previous studies. In the study of assembly, the plate is created with the designed dimensions; the waveguides are imported and moved to symmetric locations in designed orientation. The assembled view of the set-up is given in Figure 36.
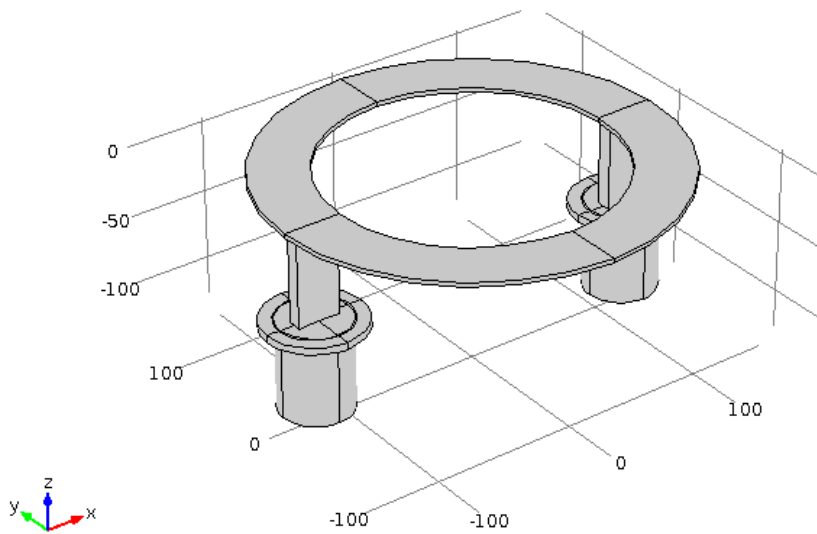
Figure 36 – Assembled set-up in COMSOL Multiphysics ®

The materials of the plate and the waveguide are $Al5754$ and $Al7075$, respectively. In the simulation, the contacting surfaces of the waveguides and the plate are modeled to be in perfect contact as in the real set-up will be made by three $M5$ bolts

for each connection. The flanges of the waveguides are modeled as fixed. These fixed locations are shown in Figure 37.
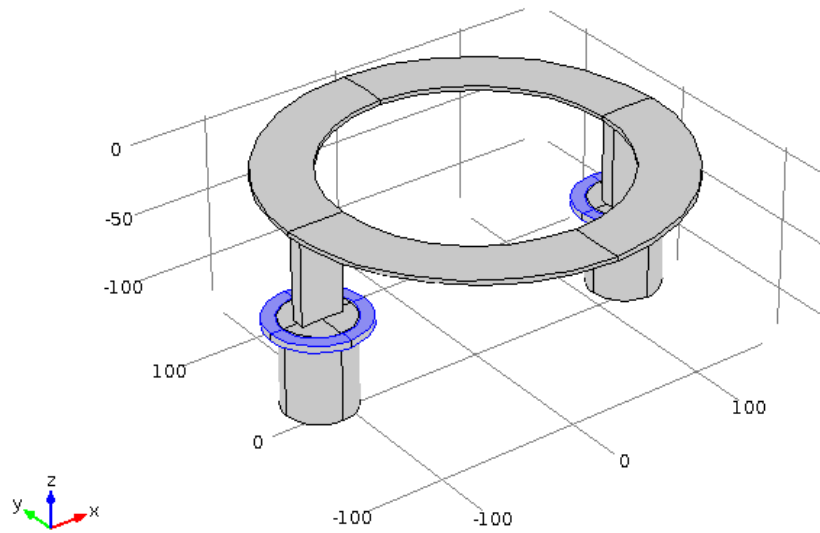
Figure 37 – Fixed flanges in the simulation

After the geometry is constructed, the mesh is done with the properties listed in Figure 38.

Element Size Parameters

Maximum element size:

3   mm

Minimum element size:

0.125   mm

Maximum element growth rate:

1.35

Resolution of curvature:

0.3

Resolution of narrow regions:

0.85

Figure 38 – Mesh parameters for the assembly

The meshed view of the assembly is displayed in Figure 39.
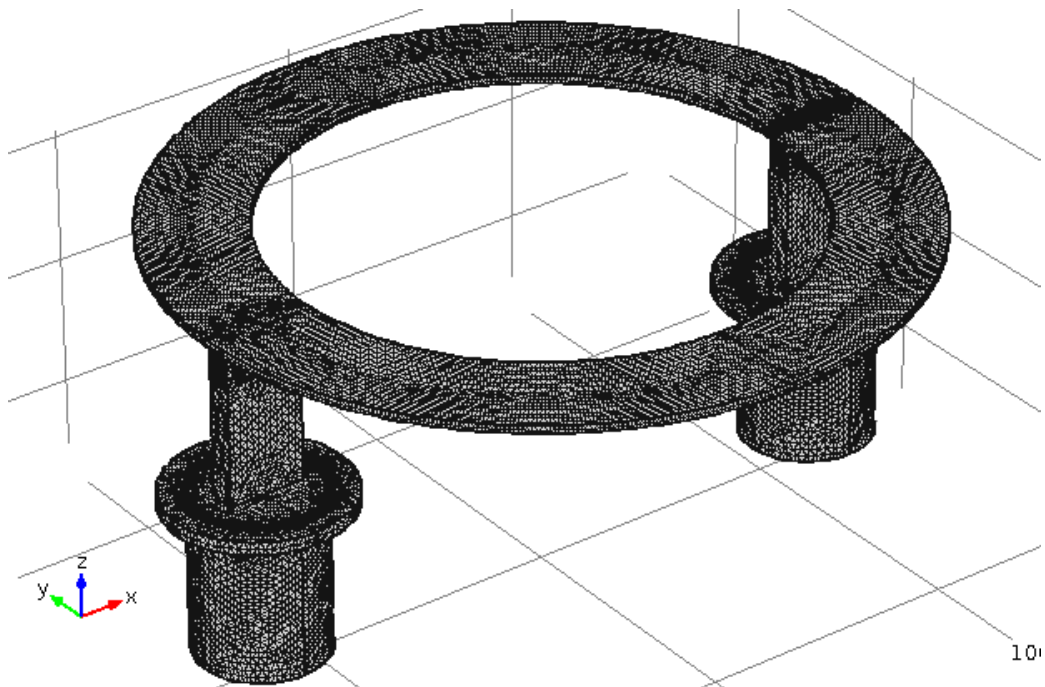
Figure 39 – Meshed view of the assembly
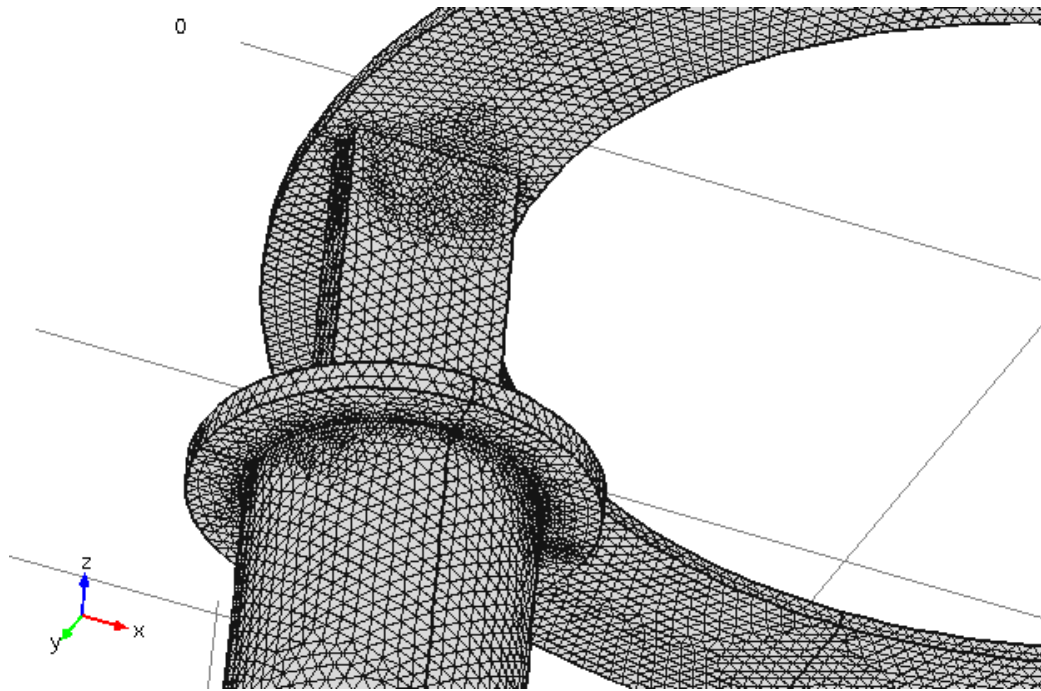
Figure 40 – Meshed view of the assembly

In the simulation, natural frequencies of the system are searched around 20 kHz. The modes between 19.5 kHz and 20 kHz are checked and evaluated. A particular mode at 19525 Hz is shown in Figure 41. It should be recalled that the displacement output is given as mass normalized by the software in all eigenfrequency studies.
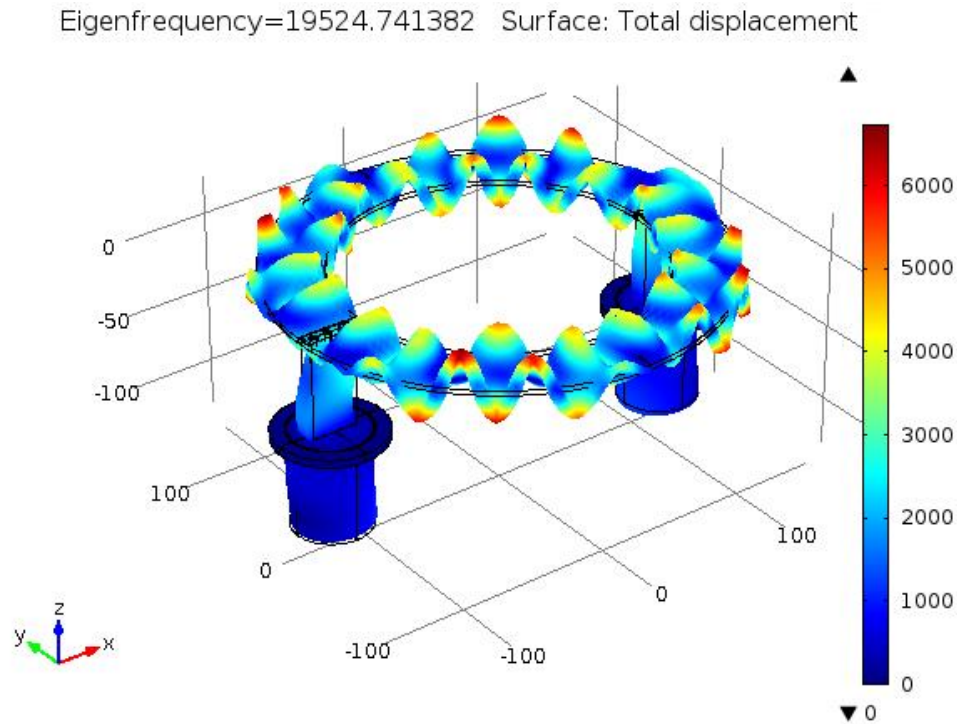
Figure 41 – Type C-like mode at 19525 Hz

The first mode obtained is similar to the type C mode of the plate. Type C modes of the plate are not preferred in the first place. Moreover, the mode does not seem to have a symmetric distribution over the angular direction. The waveguide is desired to vibrate in axial direction. However, in this mode bending vibrations of the waveguide are also present. Considering all of the facts, the given mode is not found to be desirable and suitable for levitation.

The next frequency is found out to be 19707 Hz. The figure of the frequency is given in the Figure 42. Torsional vibrations occur at both plate and waveguide at that mode; therefore this mode is also not suitable and desirable for levitation.
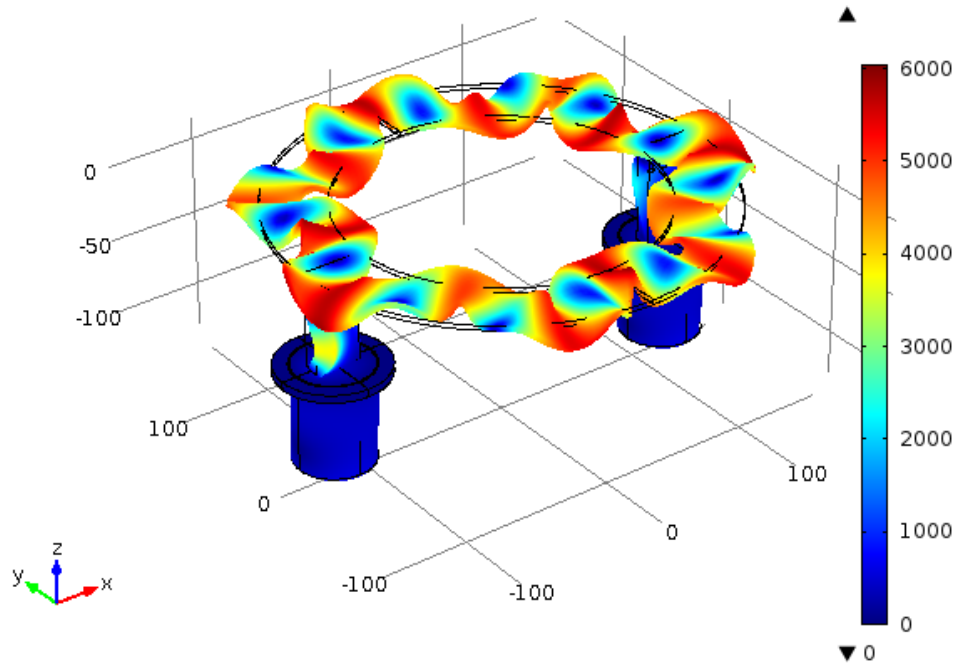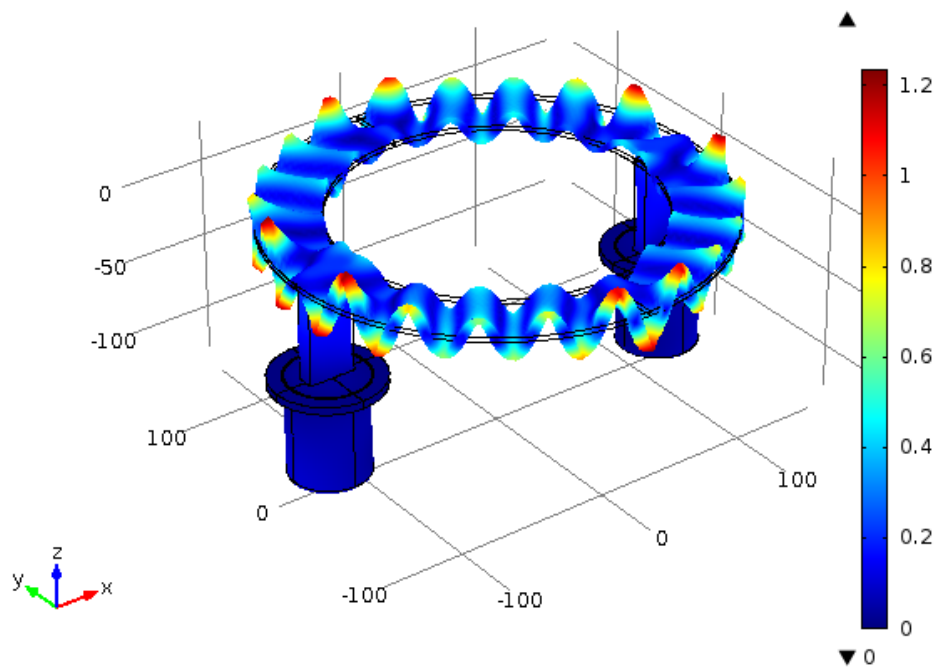
Figure 42 – Torsional mode at 19707 *Hz*

Figure 43 – Type A-like mode at 19909 *Hz*

A type A-like mode is observed at 19909 Hz. The vibrations are mainly occurring on the plate while the waveguide vibrates less compared to the plate. The plate is vibrating in bending mode and the waveguide vibrates in axial mode. Although this mode looks like a type A mode, it is not a type A mode at all. It does not have symmetry along the central axis of the plate and it mainly is not a type A mode. The radial vibration distribution does not fit to the type A model. This mode, despite having bending vibrations on the plate and axial vibrations on the waveguide, is not a suitable/feasible and desirable mode for levitation.

Another type A-like mode is observed at 20191 Hz. The bending vibrations on the plate are similar to the previous mode. Waveguide, however, vibrates in bending mode at this frequency. The mode is displayed in Figure 44. This mode is not a desirable and suitable/feasible mode for levitation.
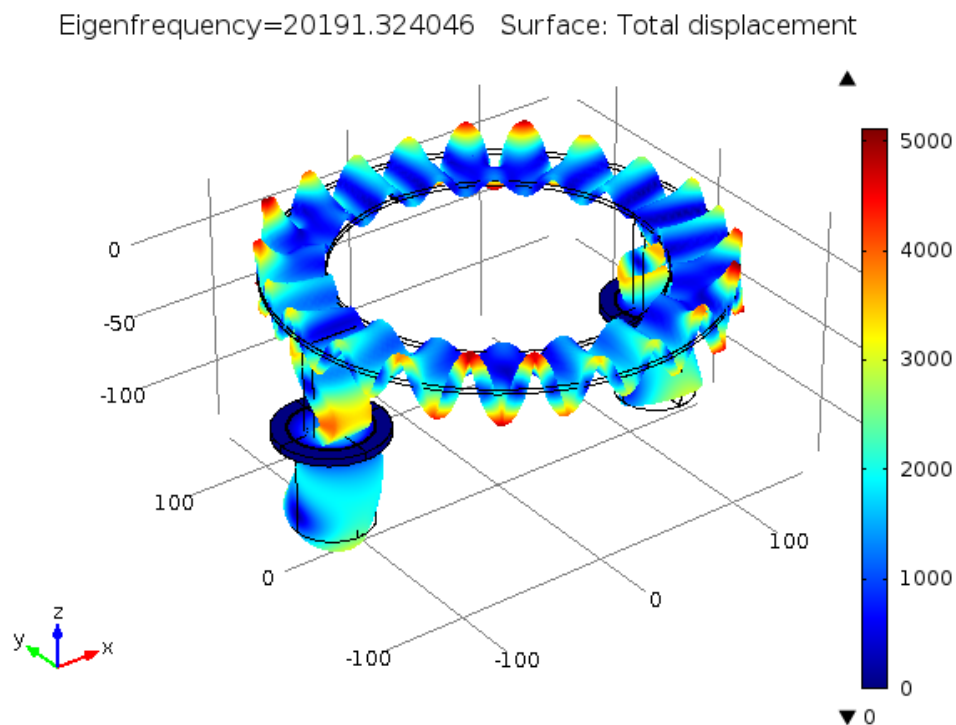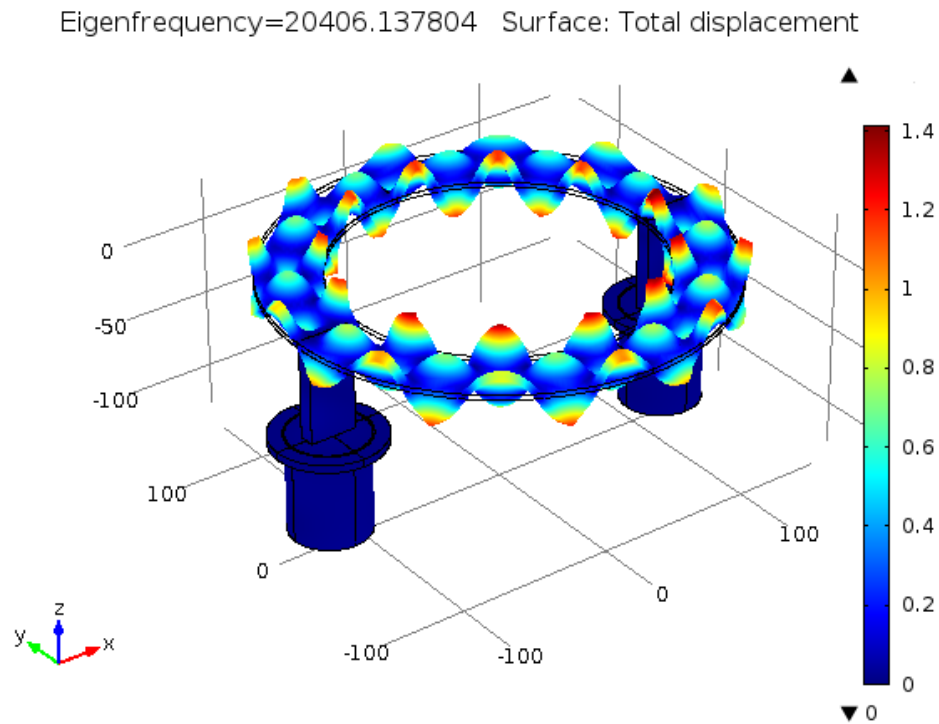

Figure 44 – Type A-like mode at 20191 Hz

94

Figure 45 – Type B mode at 20406 Hz

A type B mode is found at 20406 Hz. The plate vibrates in bending more at a type B mode. Although some minor differences in amplitude seem to be present, the mode is symmetric around the central axis of the plate. The waveguide is vibrating in axial mode, and vibration amplitude is drastically low compared to the amplitudes on the plate. This indicated that vibrations mainly occur on the plate while the waveguide will just transfer the vibrations to the plate. It can also be inferred that the plate here acts like a vibration absorber attached on the waveguides. The mode is the desired/feasible and suitable mode for levitation. The design for reflector will be based on the assumption that the assembled set-up is working at this frequency and this mode.

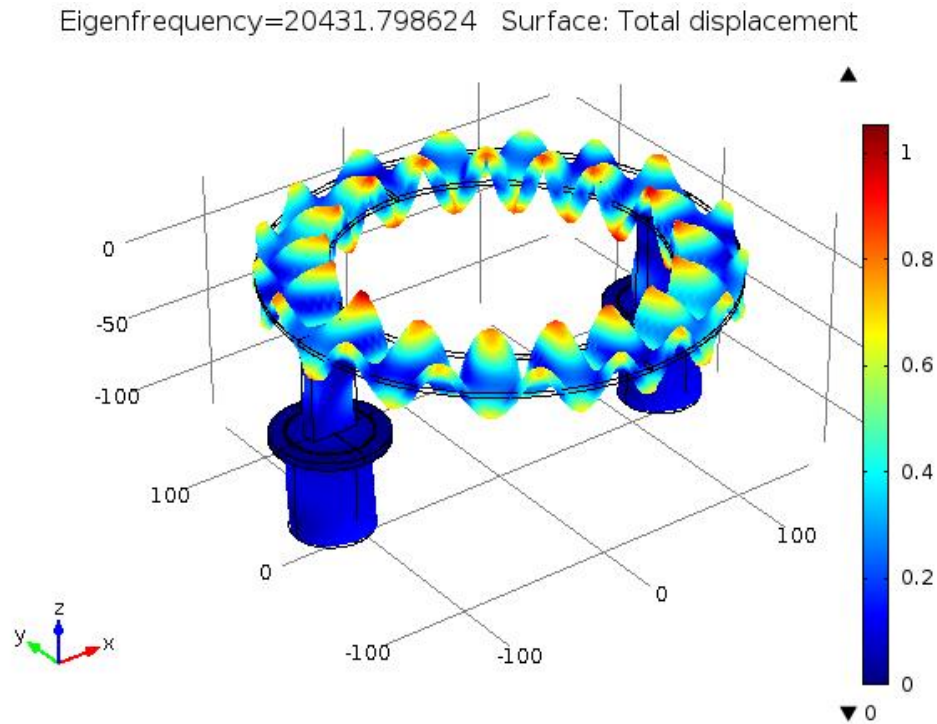Another mode observed at the frequency of 20432 Hz is illustrated in Figure 46.

Figure 46 – Type C mode at $20432\ Hz$

The mode at $20432\ Hz$ is a type C mode. The plate is vibrating in bending mode, and the vibrations are symmetric around the central axis of the plate. The waveguide seem not to vibrate much here but the mode it vibrates in is a torsional mode. Torsional vibrations on the waveguide are not desired; hence the mode is also not a suitable and not a desirable mode for levitation.

Of the modes observed between $19500\ Hz - 20500\ Hz$, the type B mode at $20406\ Hz$ will be used for levitation. The reflector will be designed to get maximum contribution from the selected mode.

96

4.4.1 Assembly with Transducers

Another study is carried out including the transducers. This study is initially planned as a future work, but it is realized within the framework of the thesis later. The mesh parameters for the study are illustrated in Figure 47.

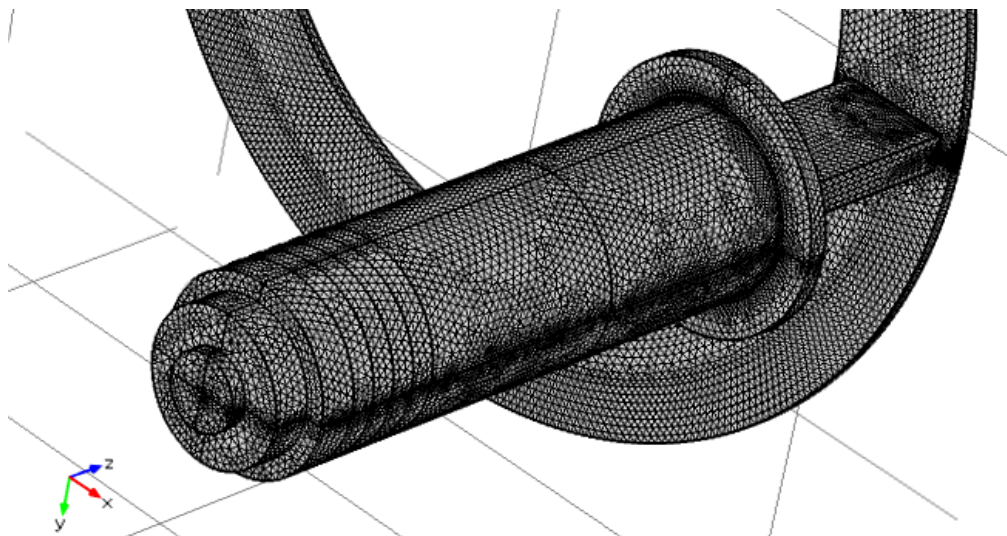Figure 47 – Mesh parameters for the assembly including transducers

Figure 48 – Meshed view of the assembly including transducers

This study predicted a type B mode at $20345\ Hz$. This mode was previously predicted to occur at $20406\ Hz$. As extra material is added to the system, the frequencies shift down. There also exist a type C mode at $20395\ Hz$ and a type A mode at $19920\ Hz$. The type B mode predicted is illustrated in Figure 49.
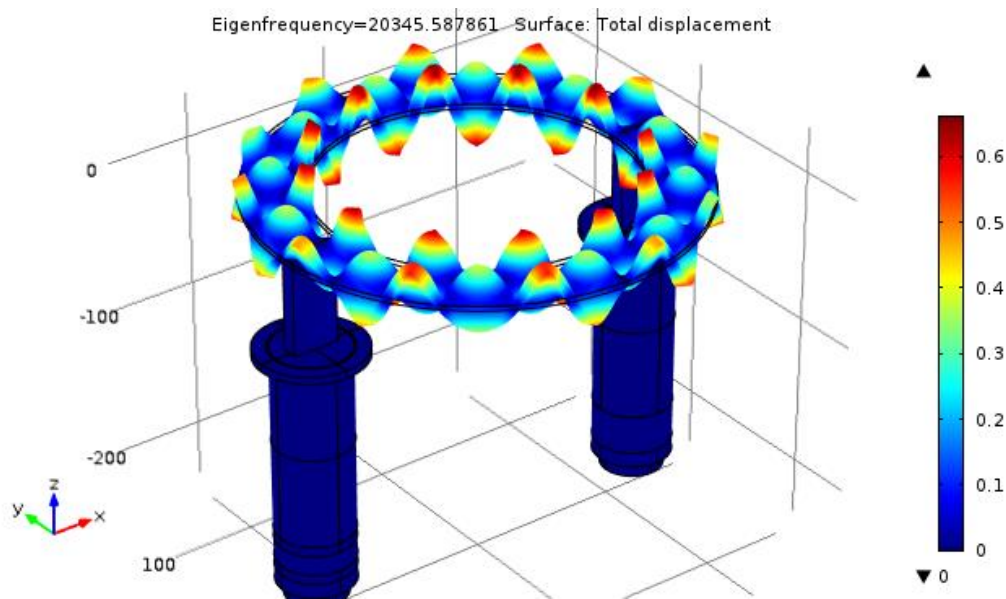

Figure 49 – Type B mode at $20345\ Hz$

It is predicted in the previous study, which omits the effects of transducers such that the desired frequency of operation of the set-up lays within the transducers' effective operating range. When the transducers are added to the assembly an even more accurate frequency is predicted.

4.5 Reflector

A reflector is positioned to form a standing wave between the source and the reflector. The reflector will be of annular shape to cover all over the plate. The surface of the reflector may be flat, concave of convex. Convex surfaces are immediately eliminated as they will obviously scatter the sound, weakening the standing wave obtained. Concave reflectors will focus the incident wave and expected to fortify the standing wave. A type B mode is used on the plate; therefore the simulations for the reflector will be conducted based on the assumption of a type B mode.

The simulation for determination of the radius of curvature of the reflector will include the air between reflector and the plate. The waveguides do not need to be included. COMSOL Multiphysics ® allows users to simulate an air cavity with excitation introduced as normal acceleration. The simulation will use the acceleration distribution on the plate as normal acceleration to the air at $20406\,Hz$. The vibration distribution of a type B mode is already been resolved in the radial direction. An eighth order polynomial represents the distribution at a highly satisfactory accuracy. If the general form of the mode shape is recalled:

$$W_n(r,\theta) = [A_n J_n(\beta r) + B_n Y_n(\beta r) + C_n I_n(\beta r) + D_n K_n(\beta r)]\cos(n\theta) \tag{168}$$

It is seen that the radial distribution has a harmonic distribution in the angular direction. Checking at the mode shape obtained, the number of times that the distribution repeats itself is found out to be 12. The radial distribution containing Bessel functions is replaced by a fitted polynomial in this case. Therefore, the vibration distribution of the plate will be represented as

$$W_n(r,\theta) = f_{fit}(r)\cos(12\theta) \tag{169}$$

The acceleration distribution is given by, owing to the harmonic structure of the vibrations

$$W_n''(r,\theta) = -\omega^2 f_{fit}(r)\cos(12\theta) \tag{170}$$

Exact values of the distributions are not needed to compare the reflector shape. Therefore, a normalized distribution is used where the maximum acceleration is unity.

$$W_n''(r,\theta) = f_{fit}^{normalized}(r)\cos(12\theta) \tag{171}$$

The normalized polynomial fit is obtained from exporting the acceleration data among radius in COMSOL Multiphysics ® and post processing the data to fit a curve in MATLAB ®. 379 data points are used from inner radius of $100\ mm$ to outer radius of $140\ mm$. The exported data contain the position information and the acceleration information.

The procedure for obtaining the polynomial coefficients is already given in Section 4.1. The fitted polynomial and the exported data are seen in Figure 50.
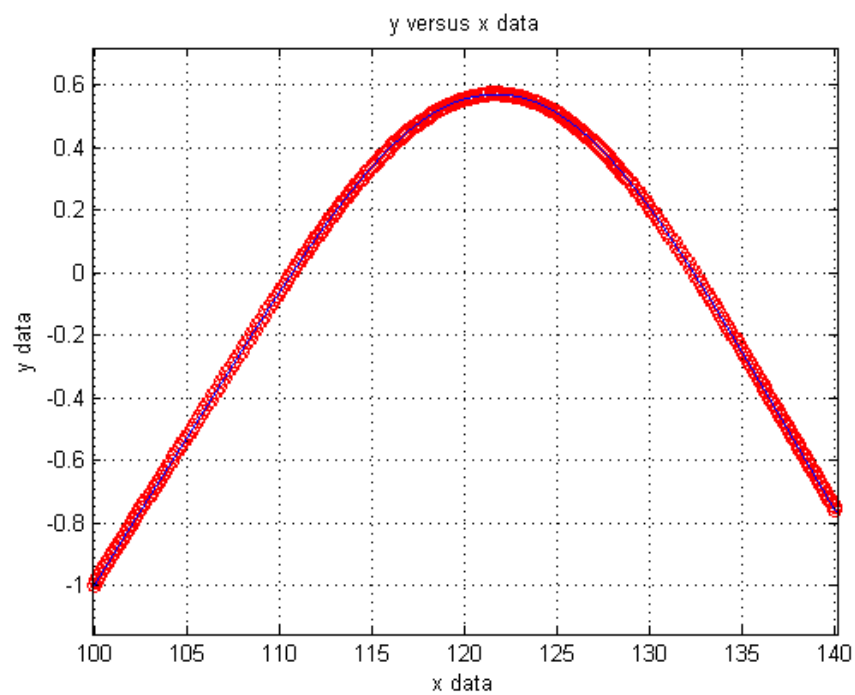
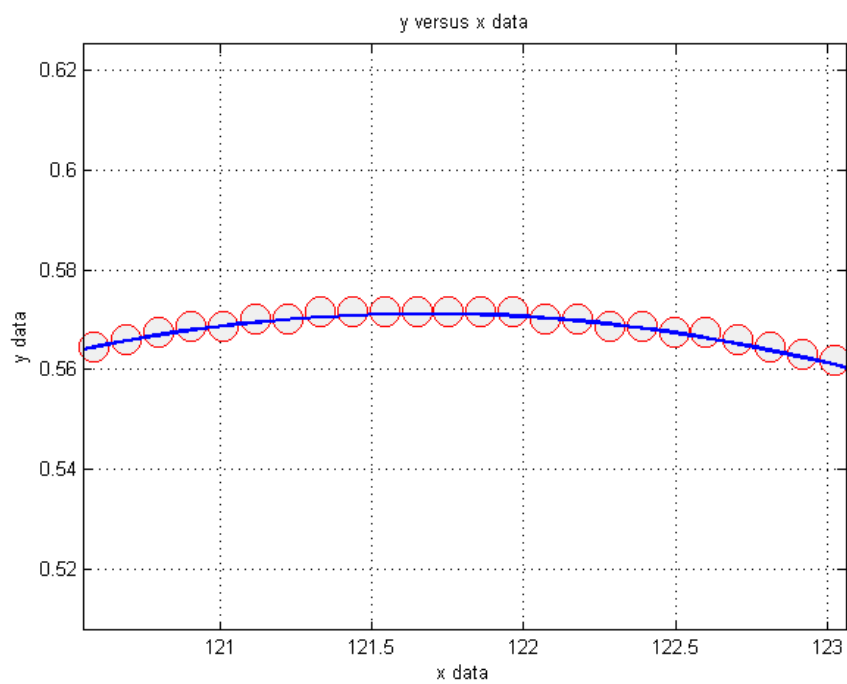Figure 50 – The polynomial fit (blue line) and data points (red circles)

Figure 51 – The polynomial fit (blue line) and data points (red circles)

The polynomial fit as a function of radius is expressed as:

$$a_r^{fit}(r) = -7.49 \times 10^{-14} r^8 + 3.413 \times 10^{-11} r^7 - 3.39$$
$$\times 10^{-9} r^6 - 5.48 \times 10^{-7} r^5 + 9.056$$
$$\times 10^{-5} r^4 + 0.0092 r^3 - 2.7 r^2 + 200.348 r \qquad (172)$$
$$- 5.084 \times 10^3 \ m/s^2$$

The total acceleration distribution is given by

$$a(r,\theta) = a_r^{fit} \cos(12\theta)$$

$$(173)$$

With the fitted data, the acceleration distribution on the plate (which also corresponds to the mode shape due to harmonic condition) can be plotted as in Figure 52.
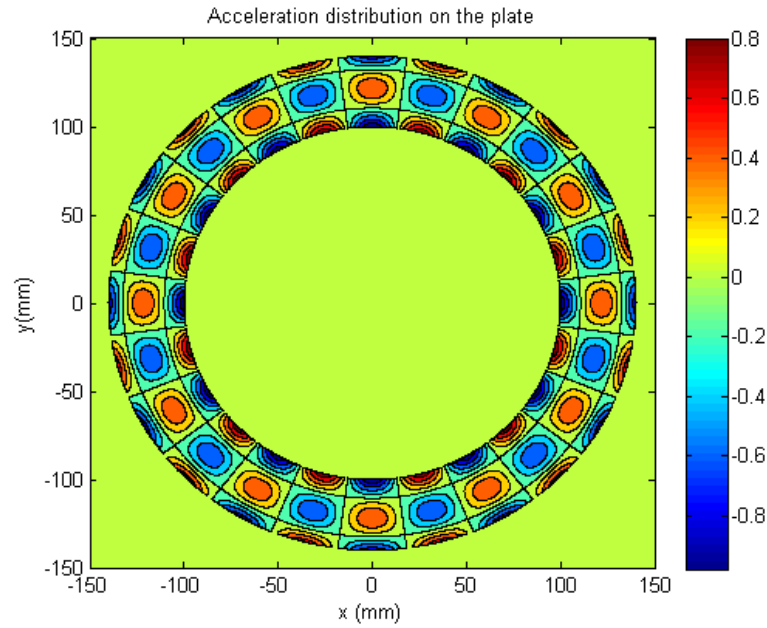
Figure 52 – Acceleration distribution with fitted data

The plot with the fitted data well represents the type B mode. The maximum pressure will be obtained where the vibration amplitude is at its maximum. Referring the figure obtained in MATLAB ®, the plane to be investigated will be normal to the plate surface at $x = 0$ line. The pressures will be evaluated on a slice cutting through that surface.

The simulation started with the flat reflector case. The mesh parameters of the plate are given in Figure 53. The parameter "lam0" represents the wavelength of the sound at the excitation frequency.

Figure 53 – Mesh parameters of air in reflector simulation

Figure 54 – Meshed view of the air

To avoid high computational work, not all the air but some angular segment of the air will be included. The arc is started as 10° segment and increased, the obtained pressures are compared. After a certain angle the maximum value of pressure converged to a value and it is concluded that a 120° segment is satisfactory to

104

represent the whole air between the reflector and the plate. The pressure distribution for a flat reflector is given in Figure 55.
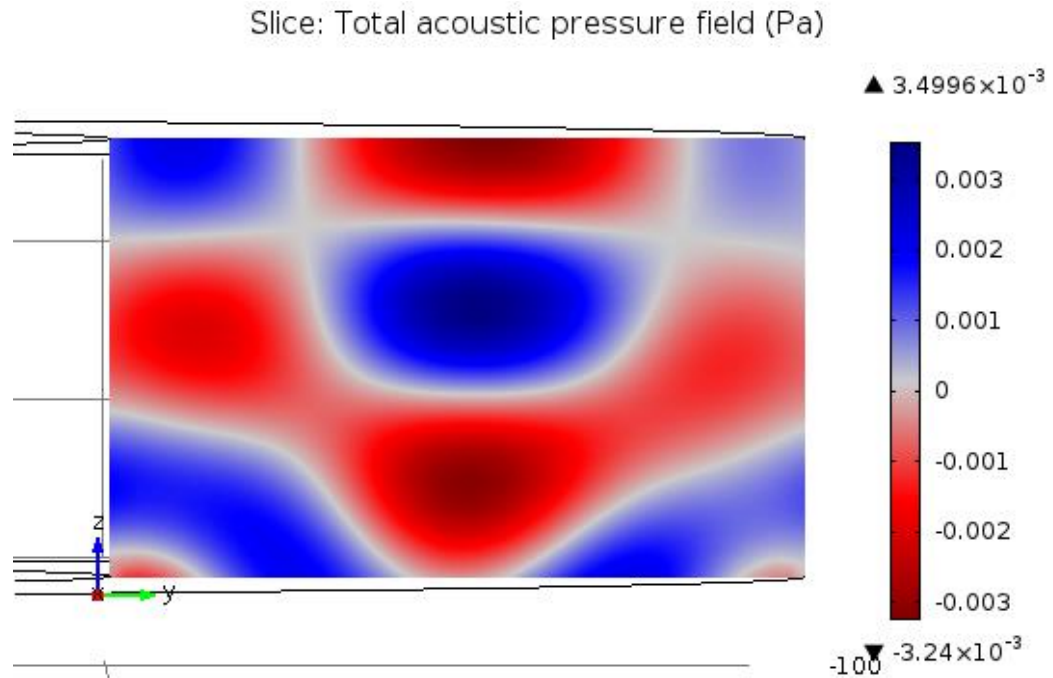

Figure 55 – Pressure distribution with a flat reflector

To verify the validity of this solely-air modeling, another study is carried out. The verification study includes both the plate and the air. In this study, the excitation had to be given at the natural frequency of the unassembled plate, which is 19960 Hz. The mesh properties of the plate and air are given in Figures 56 and 57. During the simulations it is seen that the vibration distribution on the plate did not perfectly match with the vibration distribution obtained from the previous study.

In the solely-air modeled study, the acceleration is represented as normalized distribution. The verification study, however, utilizes a unit harmonic force on the plate. The force represents the excitation from the waveguides.

Figure 56 – Element size parameters for the air section

Figure 57 – Element size parameters for the plate section

The mesh parameters for the air are kept same with the solely-air study. The vibration distribution on the plate and the pressure distribution are illustrated in Figures 58 and 59.
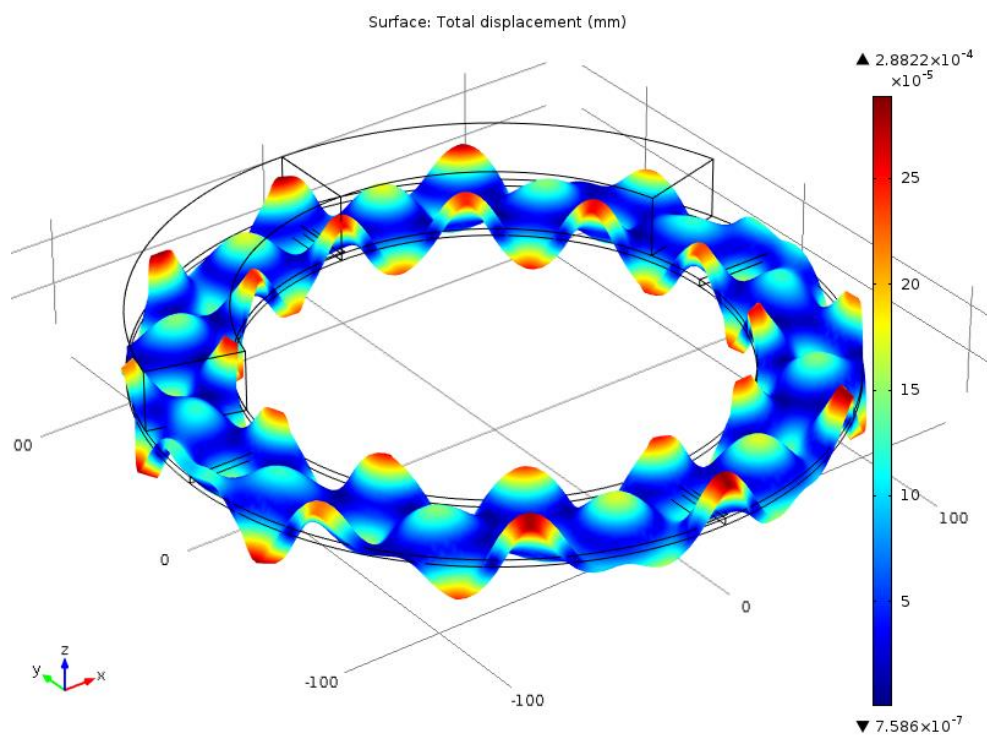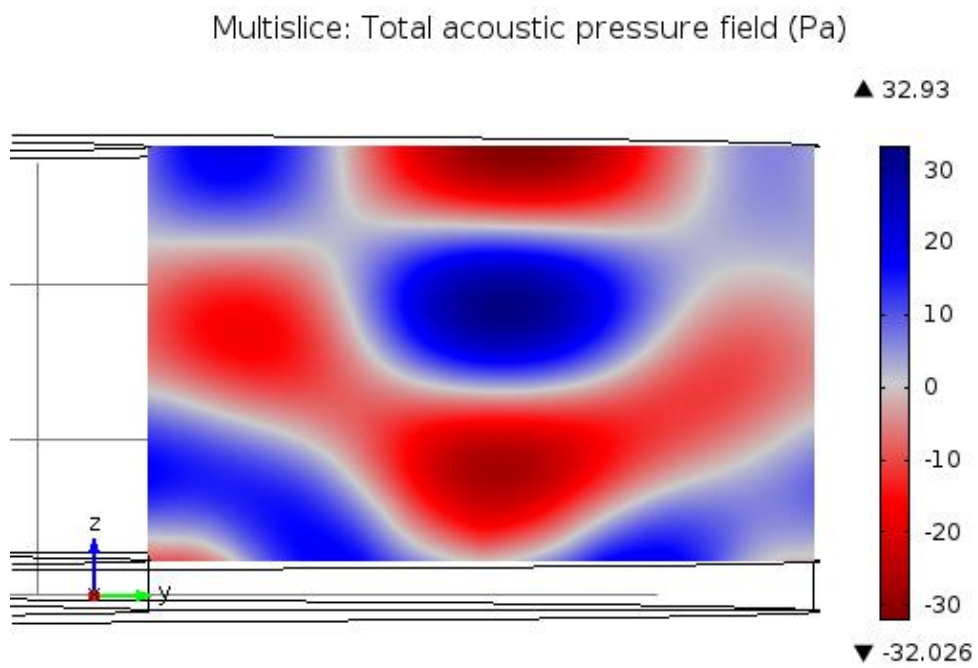
Figure 58 – Vibration distribution on the plate

Figure 59 – Pressure distribution on a slice

The amplitude of the pressures does not match as in the solely-air study normalized distribution is used. If the vibration distribution is investigated, it can be seen that the reason of slight differences in the pressure distributions at the lateral edges of the sliced plane is the not-exactly-type B vibration distribution on the plate. Therefore, except the slight differences on the sides/edges, the solely-air simulations represent well the wave behavior in air between the plate and the reflector.

The simulations for determining the shape of the reflector will start with the flat case. The diameter of concavity started from $45\ mm$ and increased by $5\ mm$ increments to $120\ mm$. As the purpose of the reflector is to focus and amplify acoustic pressure, the diameter which yields maximum pressure amplitude will be used. If the diameter of concavity of the reflector is $d_r = 45\ mm$, the pressure distribution in Figure 60 is obtained for a normalized acceleration distribution.
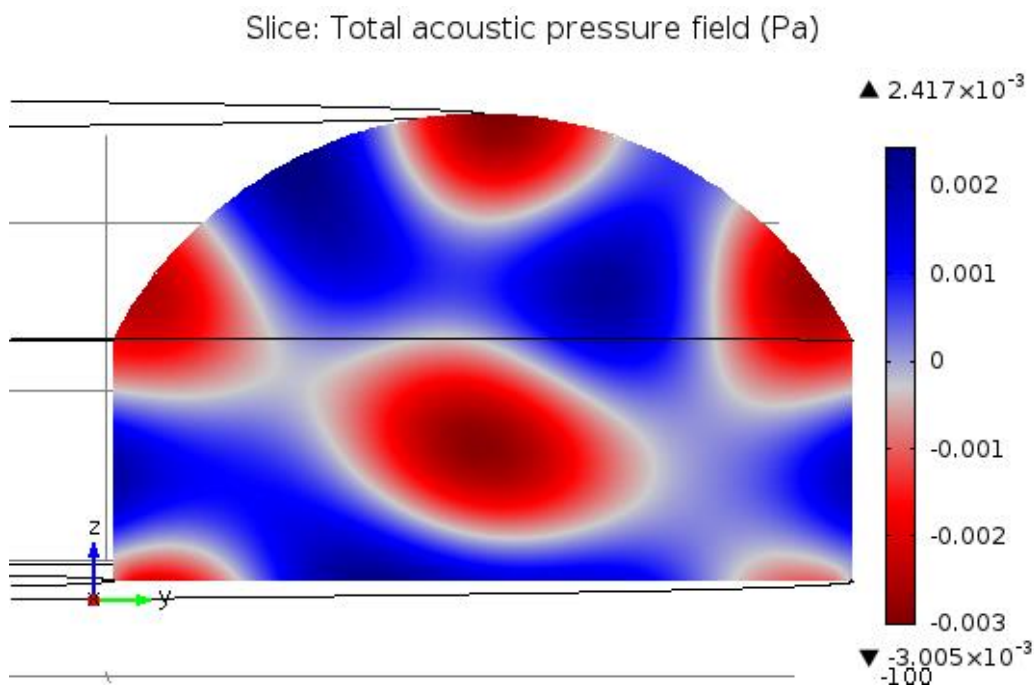

Figure 60 – Pressure distribution when $d_r = 45\ mm$

During the simulations it is observed that if the diameter of concavity is too small, it is focusing too much that it results in highly uneven pressure distribution. When $d_r = 55\ mm$, the distribution in Figure 61 is obtained.
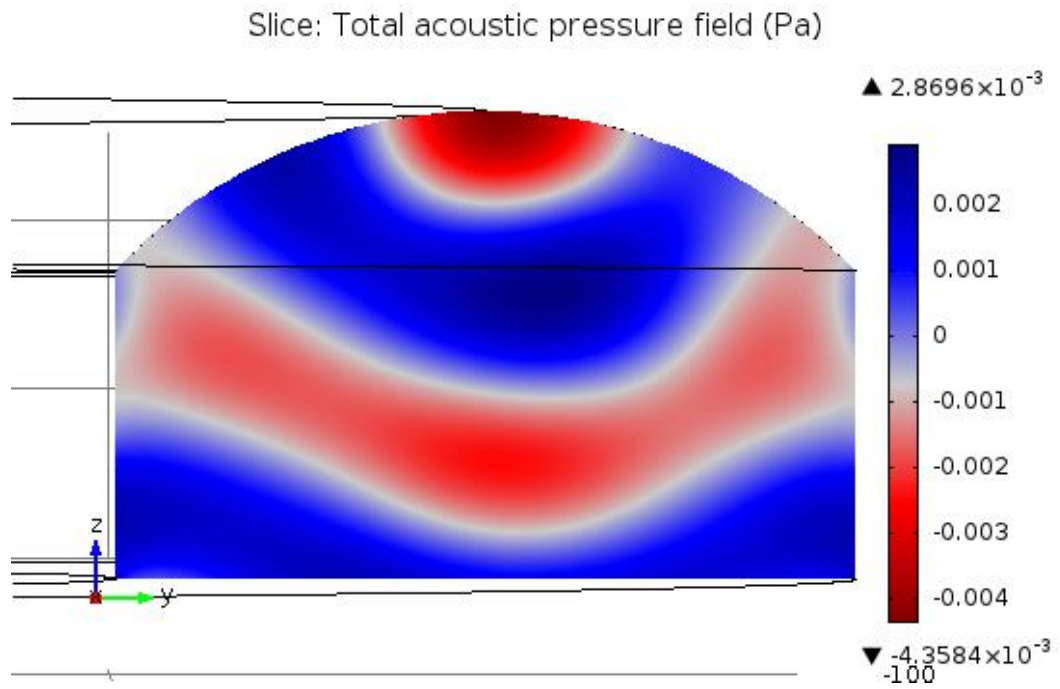

Figure 61 – Pressure distribution when $d_r = 55\ mm$

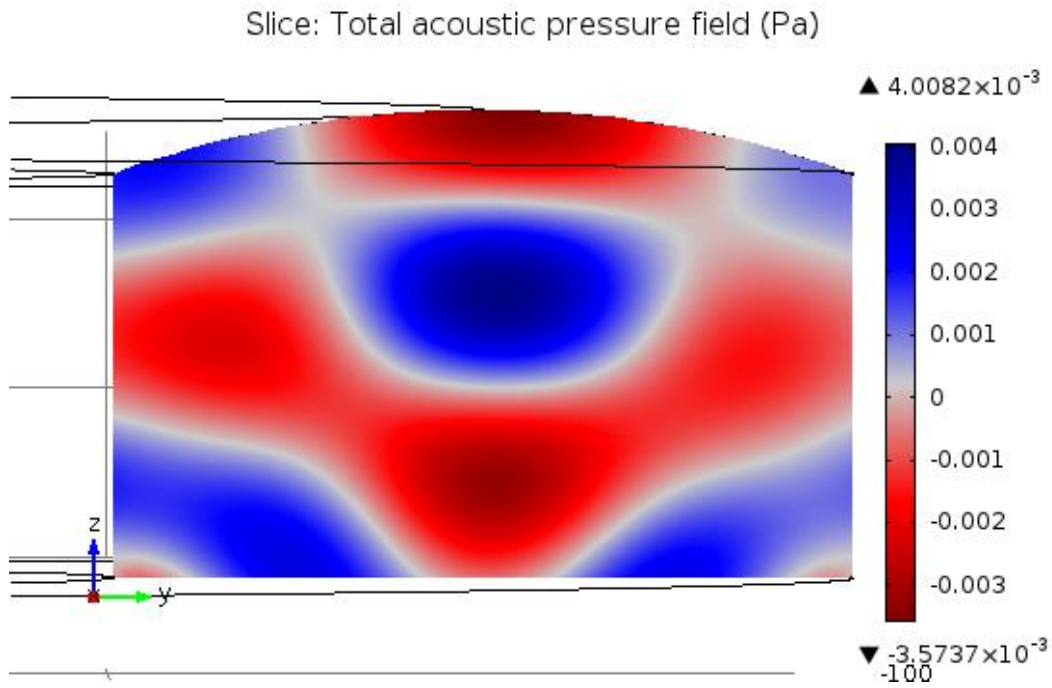A diameter of concavity of $d_r = 120\ mm$ yields the distribution given in Figure 62.

Figure 62 – Pressure distribution when $d_r = 120\ mm$

Table 9 lists the maximum pressure amplitude for differing values of d_r. It should be noted that in the simulations to determine the d_r value, normalized acceleration distribution is used.

Table 9 – Maximum pressure for different values of d_r

$d_r\ (mm)$	$P_{max}\ (Pa)$
45	3.005×10^{-3}
50	3.487×10^{-3}
55	4.358×10^{-3}
60	4.514×10^{-3}
65	4.383×10^{-3}
70	4.43×10^{-3}
75	4.413×10^{-3}

Table 9 (Continued)

d_r (mm)	P_{max} (Pa)
80	4.375×10^{-3}
85	4.313×10^{-3}
90	4.264×10^{-3}
95	4.214×10^{-3}
100	4.165×10^{-3}
105	4.125×10^{-3}
110	4.081×10^{-3}
115	4.041×10^{-3}
120	4.008×10^{-3}
$flat$	3.45×10^{-3}

The table suggests that the maximum pressure amplitude is obtained when $d_r = 60\ mm$. The pressure distribution corresponding to this case is given in Figure 63.
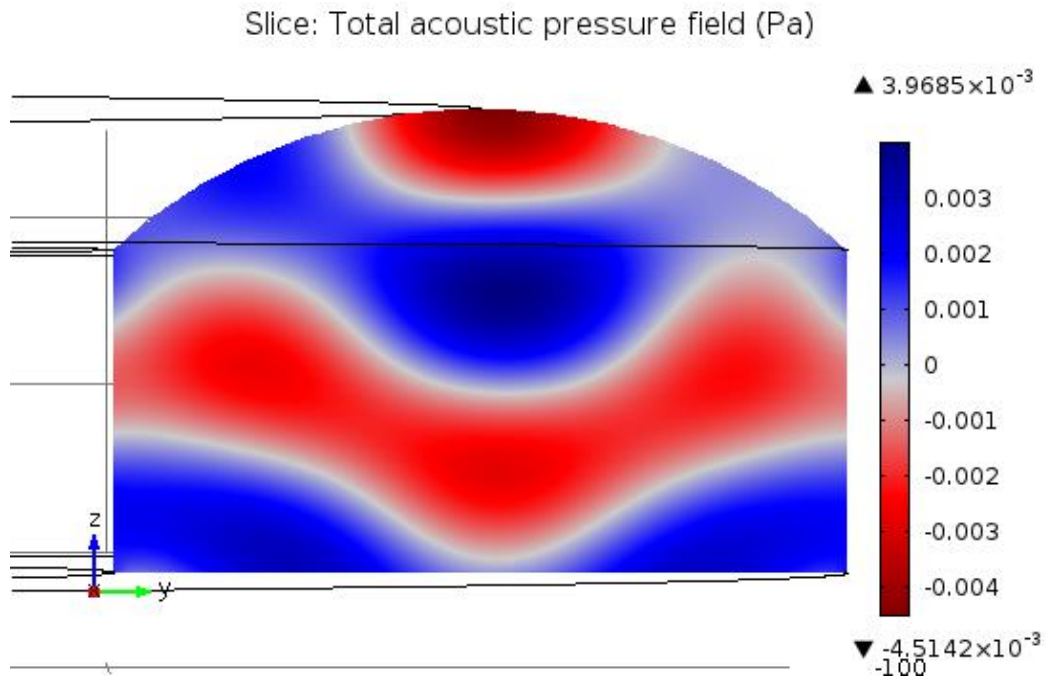
Figure 63 – Pressure distribution when $d_r = 60\ mm$

It is previously seen that when the diameter is too small the pressure is too focused that the distribution is disturbed. It should be no surprise that the maximum pressure is obtained just before the excessively focused case.

The sound pressure at the outer surfaces of the air space is shown in the next figure. The areas close to each end do not have the correct distribution as they have open ends rather than the continuity of the excitation.

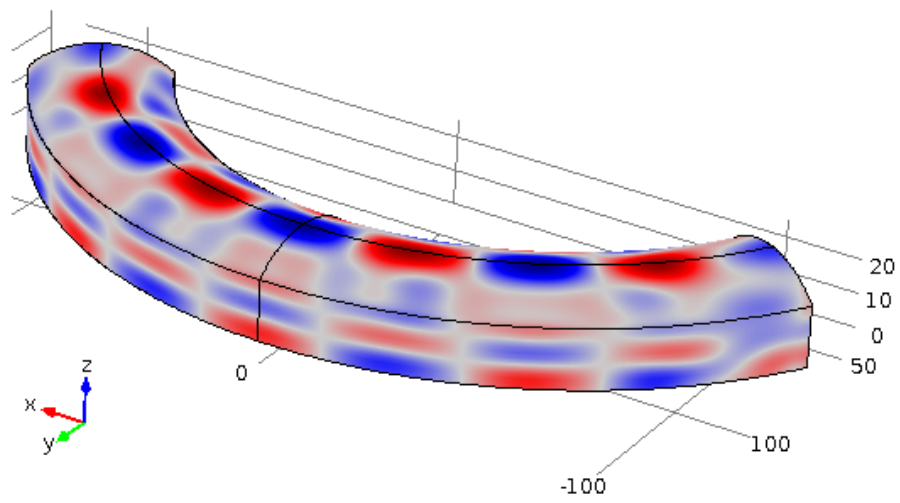dr(4)=60 Surface: Total acoustic pressure field (Pa)

Figure 64 – Acoustic pressure distribution at the outer surfaces of air

4.6 Supporting Structure

The supporting structure will include the feet to fix the waveguides from their flanges and the structures to position the reflector. The fixture is dimensioned such that it will allow both upward and downward orientation of the waveguides. As the excitation will be coming at a certain frequency, the frequency response of the foot is important at that particular frequency. The supports include two feet, two bent parts to fix the reflector and four parts to hold the flanges

The foot part is shown in Figure 65. The material will be a structural steel available at the manufacturer.
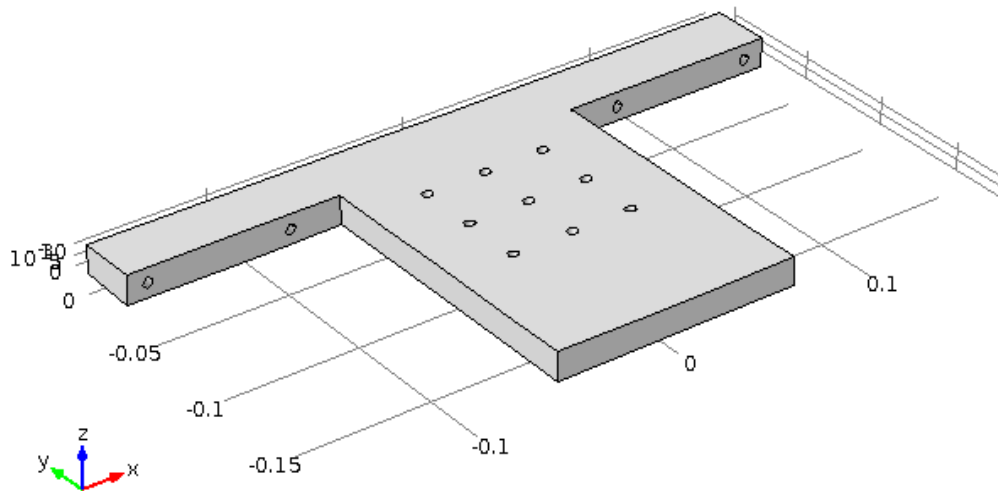

Figure 65 – The foot part

The four holes at the arms will be used to fix the flanges of the waveguide between the foot and the holding parts. The nine holes are used for the connection of reflector. The excitation coming from the waveguides will come from the contacting surfaces. The natural frequencies of the foot are calculated in COMSOL

Multiphysics ®. Excitation is coming from y direction on the arms. Therefore, the important thing is the foot should not have any bending mode around $20400\,Hz$.

The modes around $20400\,Hz$ are as follows. At $19096\,Hz$, a bending mode in z direction exists. A torsional mode on x axis exists at $19667\,Hz$. An axial mode on y axis exists at $20620\,Hz$ and another bending mode on z axis exists at $20867\,Hz$.

The flanges of the waveguides will be fixed between the foot and the holding part. The material of the holding part is also structural steel. It is shown in Figure 66.

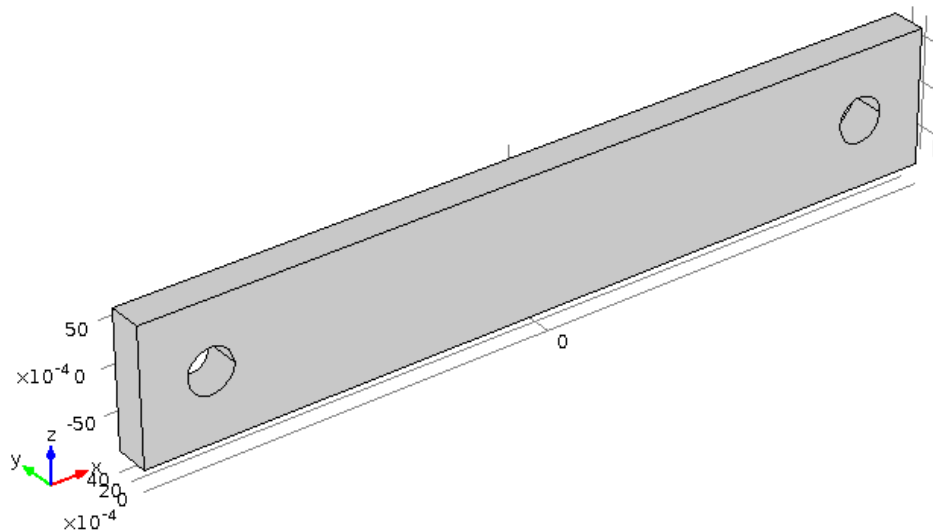
Figure 66 – Holding part

The natural frequencies of the holding part around $20400\,Hz$ are calculated in COMSOL Multiphysics ®. The part will be excited in y direction, therefore it should not have any bending mode in y direction around the excitation frequency. In the simulation it is found that the closest mode to $20400\,Hz$ is a bending mode in z direction occurring at $21095\,Hz$.

The connection of the reflector to the foot parts will be done through two bent parts. The material of the bent parts will be aluminum available at manufacturer.

The bent part is shown in Figure 67.
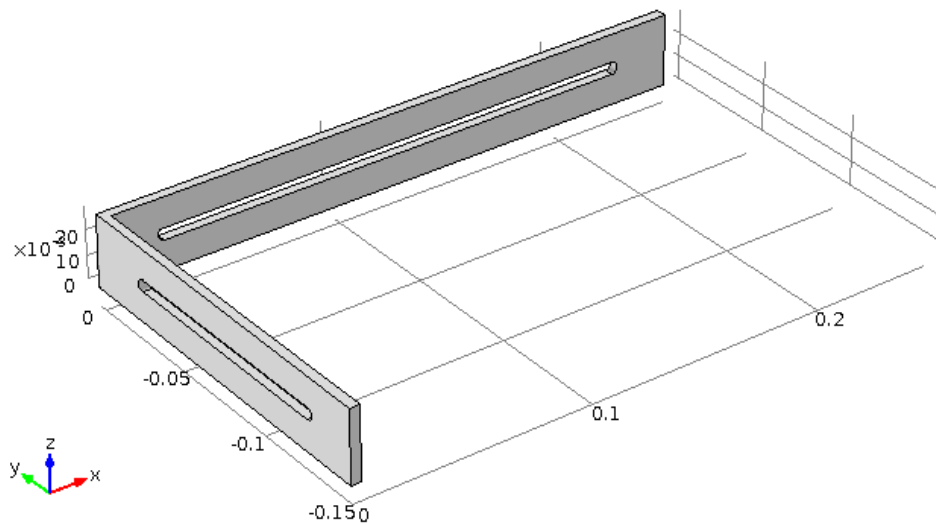
Figure 67 – The bent part

The excitation to the bent part can be taken as coming in the x direction from the reflector. The natural frequencies of the part are calculated in COMSOL Multiphysics ®. The closest frequency to $20400\,Hz$ is a torsional mode in x direction at $20600\,Hz$.

4.7 The Assembly

The assembled set-up is shown in Figure 68 with upward configuration. Transducers and connecting elements are not shown in the figure.

Figure 68 – Assembled view of the set-up

CHAPTER 5

EXPERIMENTAL STUDIES

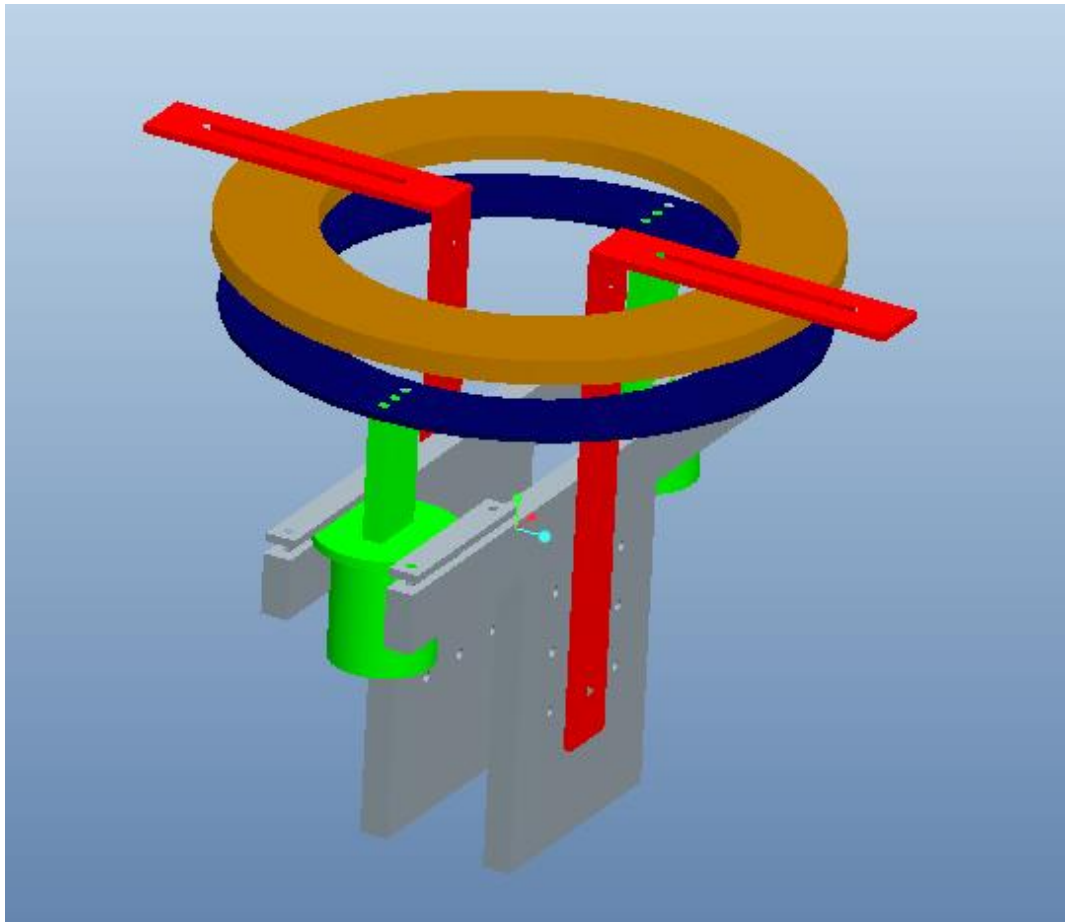Once the set-up is manufactured and assembled, levitation of some material is performed. The schematic view of the set-up is in the Figure 69.

```
┌─────────────────┐                    ┌─────────────────┐
│   HP Signal     │ - - - - - - - ->   │ Derritron TA300 │
│   Generator     │                    │   Amplifier     │
└─────────────────┘                    └─────────────────┘
                                                │
                                                │
                                                ▼
┌─────────────────┐                    ┌─────────────────┐
│ Bending Vibrations│ <- - - - - - -   │   Transducers   │
│ of plate & Acoustic│                  │   &Waveguides   │
│   Levitation    │                    │                 │
└─────────────────┘                    └─────────────────┘
```
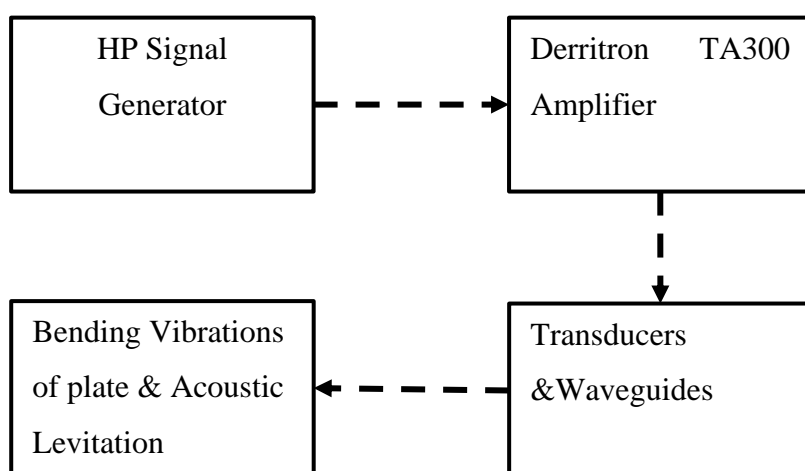
Figure 69 – Schematic representation of the set-up

The HP Signal Generator is actually dynamic signal analyzer with a wide variety of capabilities. It is used for generating harmonic signals at desired frequencies. It is also used for measuring sound by a microphone and its preamplifier. Capabilities of the generator also include frequency sweep option, which is used for detecting the bending modes of the plate. A picture of the generator is given in Figure 70.

Figure 70 – HP 35665A Dynamic Signal Analyzer

In the figure the analyzer is connected to the power amplifier via source port and an external microphone is connected to the analyzer via channel 1 port. The connections are realized with BNC connectors and the data is transferred with coaxial cables. The microphone is not shown and placed approximately one meter away from the analyzer.

The power amplifier used in this set-up is a Derritron TA300 model. This device takes input from a coaxial cable with a BNC connector and gives AC output from two ports. These ports are of $180°$ phase and therefore can be taken as $(+)$ and $(-)$ ports. The amplifier is able to deliver $20 \, V_{PP}$ at maximum. Having the output ports at opposite phases are ideal for driving piezoelectric transducers. The excitation is given by applying potential difference among discs and to do so adjacent faces are connected to opposite ports on the amplifier. The amplifier has also the ability to

generate signals on its own but in the set-up the more precise HP analyzer is used as signal generator.

A picture of the amplifier is given.

Figure 71 – Derritron TA300 Power Amplifier

Figure 72 – Input and output ports of the amplifier

All parts of the set-up is manufactured and assembled. The set-up is initially assembled as if the reflector is above the plate. However, it is later placed below the plate. The reflector is manufactured as a one-quarter section due to size restrictions in assembly. The midpoint of the reflector is placed 90° away from the waveguides. Some pictures of the individual parts and assembled set-up are given.

Figure 73 – The annular plate
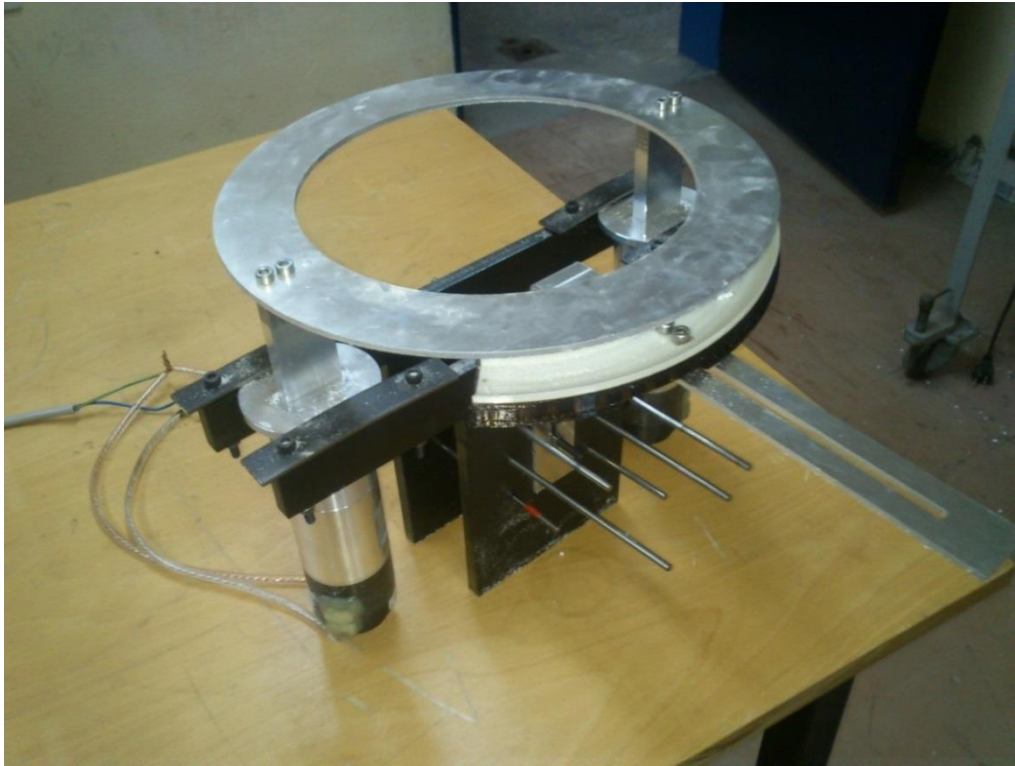

Figure 74 – A sample reflector
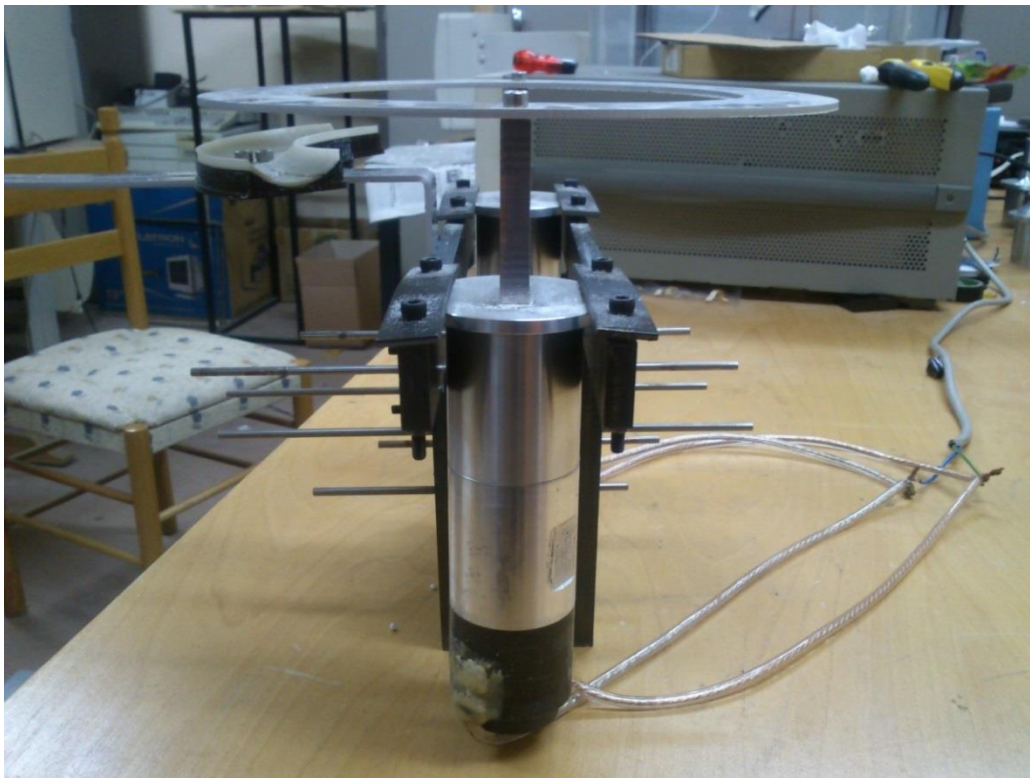
Figure 75 – Assembled view of the set-up

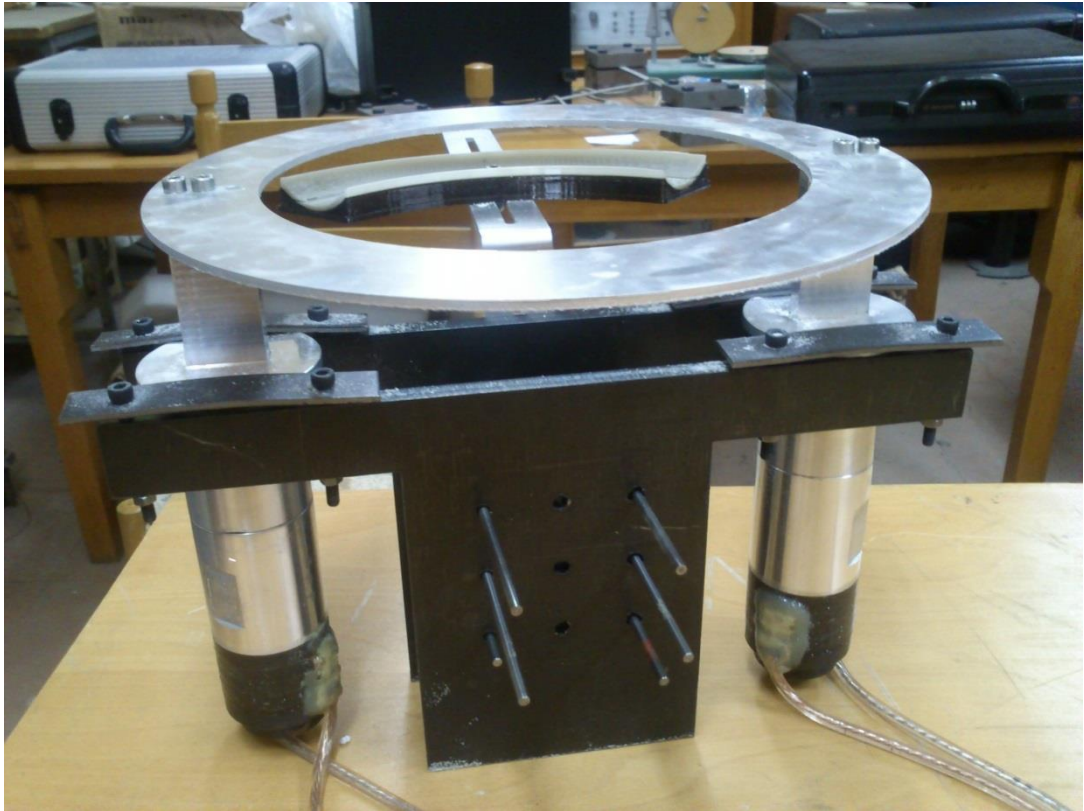Figure 76 – Assembled view of the set-up

Figure 77 – Assembled view of the set-up

The set-up needs to be tested for its natural frequencies. For this purpose, salt is poured on the plate and the mode shapes are observed through sine sweep testing. The natural frequency detection and levitation experiments are included in the next sections.

5.1 Natural Frequency Detection

Finite element simulations predicted the preferred bending mode of the plate around $20406\ Hz$. In the experiment the natural frequency is searched around that value by changing the frequency by the marker on the HP analyzer. While changing the frequencies, a type B mode is observed at $20400\ Hz$. Figures 78 and 79 show the initial position of salt particles on the plate and the concentration at resonance.

Figure 78 – Initial positions of salt particles

Figure 79 – Salt particle concentration at 20400 Hz.

The finite element simulations predicted the type B mode to be around $20406\ Hz$ and in the experiments it is observed to be at $20400\ Hz$. Considering the effects of mounting and manufacturing, the shift in the frequency is unexpectedly small. Consequently, acoustic levitation experiments are decided to be conducted with the excitation frequency of $20400\ Hz$.

5.2 Acoustic Levitation Experiments

The reflector is manufactured at a one-quarter scale. As the vibrations on the plate are symmetric among the central axis this configuration satisfactorily represents the entire set-up. The experiments are carried out on $May\ 24, 2014$ and the air temperature was measured as $19°C$ in the evening. As the set-up is designed to cover three nodes, the distance between the source and the reflector should be adjusted as follows:

The wavelength at the excitation frequency is

$$\lambda = \frac{c_0}{f} = \frac{343\ m/s}{20400\ Hz} = 16.81\ mm$$

(174)

The distance to cover three nodes will be

$$d = 3 \times \frac{\lambda}{2} = 25.22\ mm$$ (175)

The reflector is adjusted to that distance and several polystyrene particles are shown to be resting on the reflector surface in Figure 80.
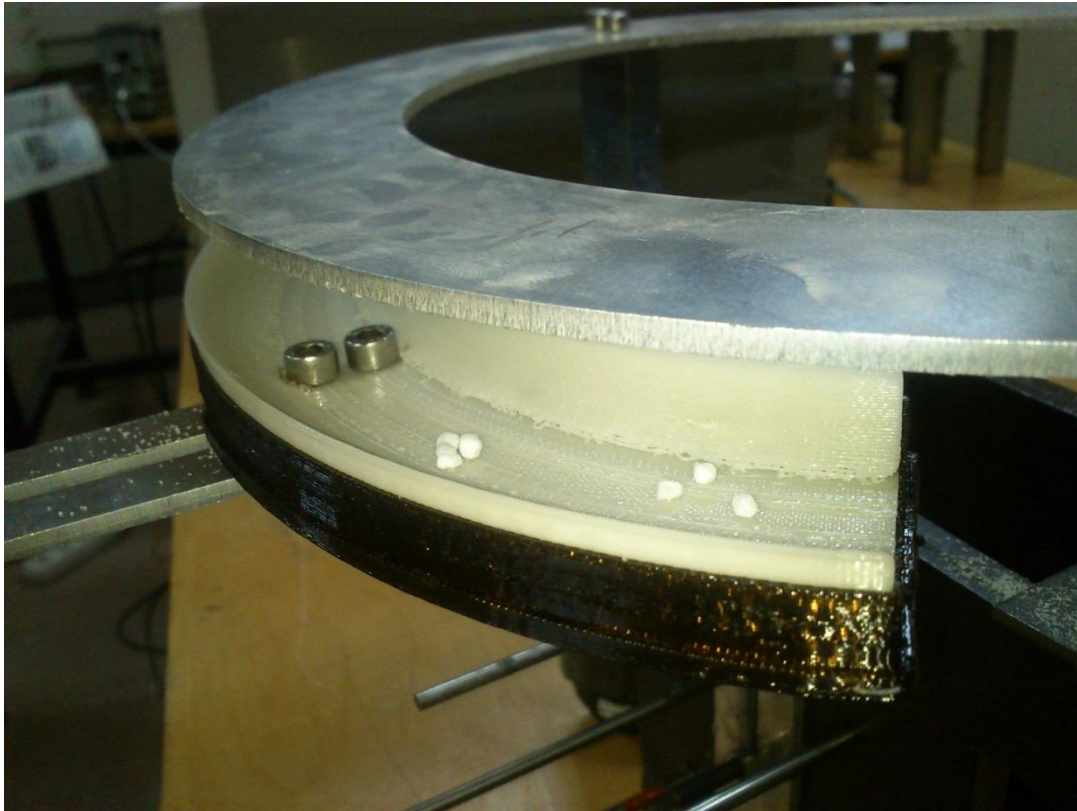
Figure 80 – Reflector and the polystyrene particles ready for experiment

The set-up is adjusted and levitation experiments are conducted. The reflector is placed using two $M5$ screws at its center. As the reflector covers a one-quarter of the set-up, 18 levitation locations are expected to be formed.

In Figure 81, a 45° section of the set-up is shown with 9 particles are successfully levitated.
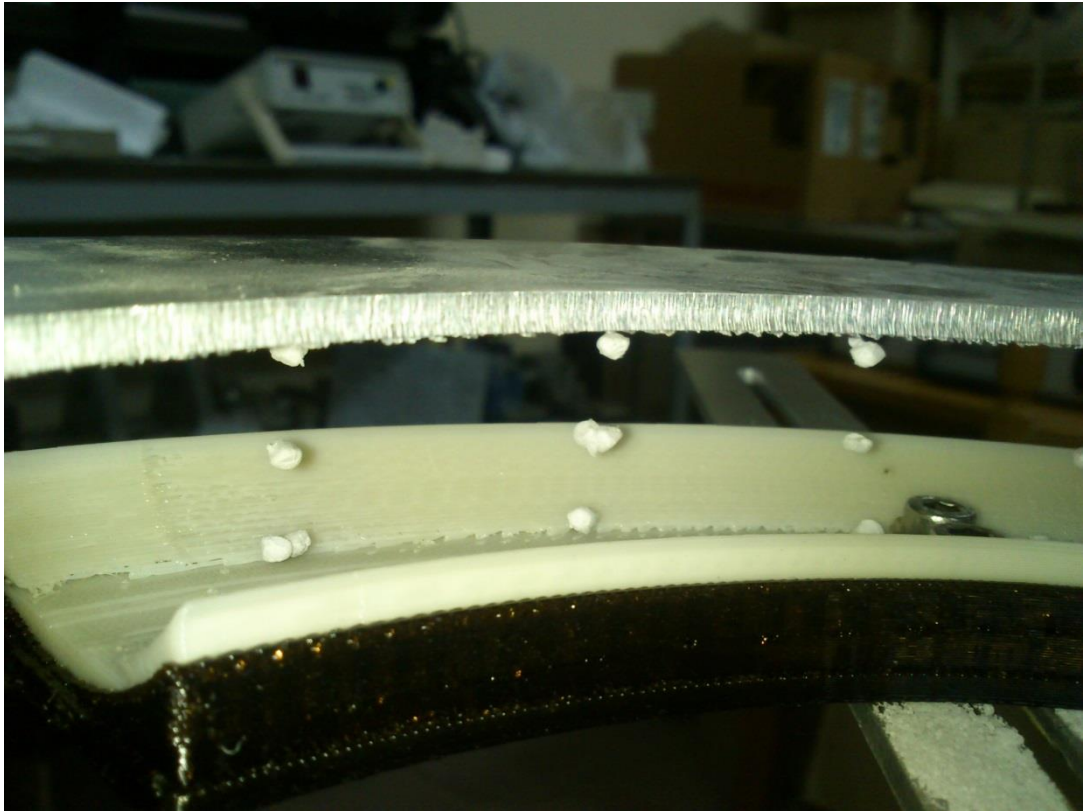
Figure 81 – Levitated particles at a one-eighth section

It is seen that the existence of the screws affects the sound field and the closest node is weaker than others. The open end at the reflector did not affect the levitation performance.

Figure 82 shows the other 45° section of the reflector whereas another figure (Figure 83) shows a wider view of the levitation.
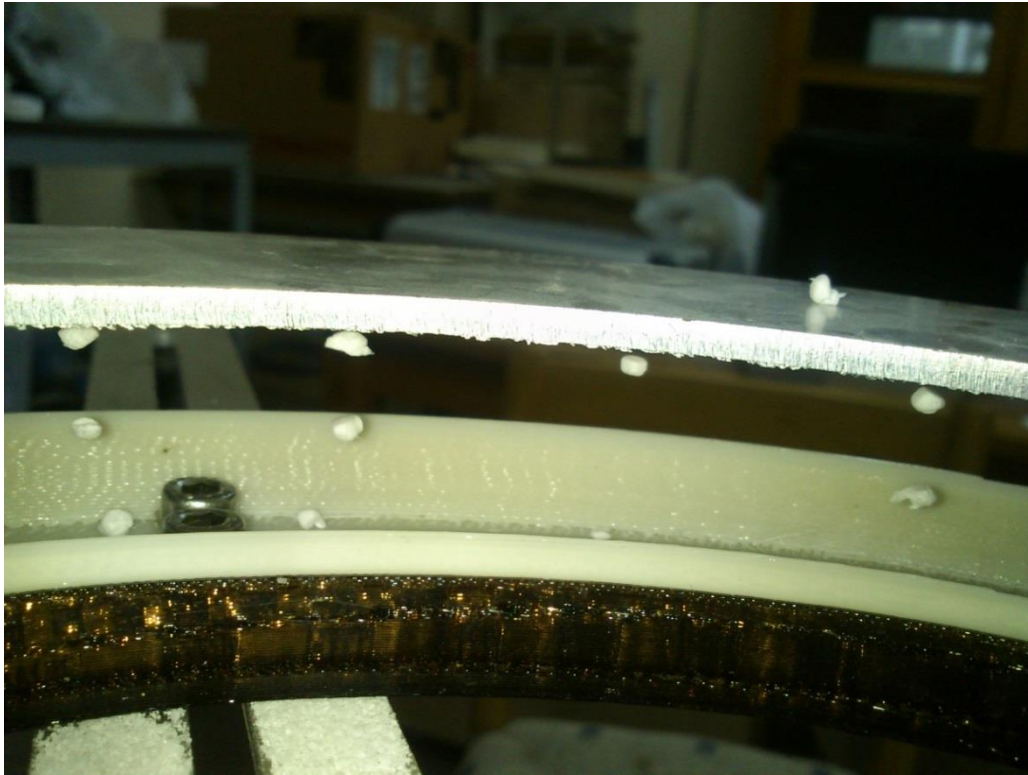
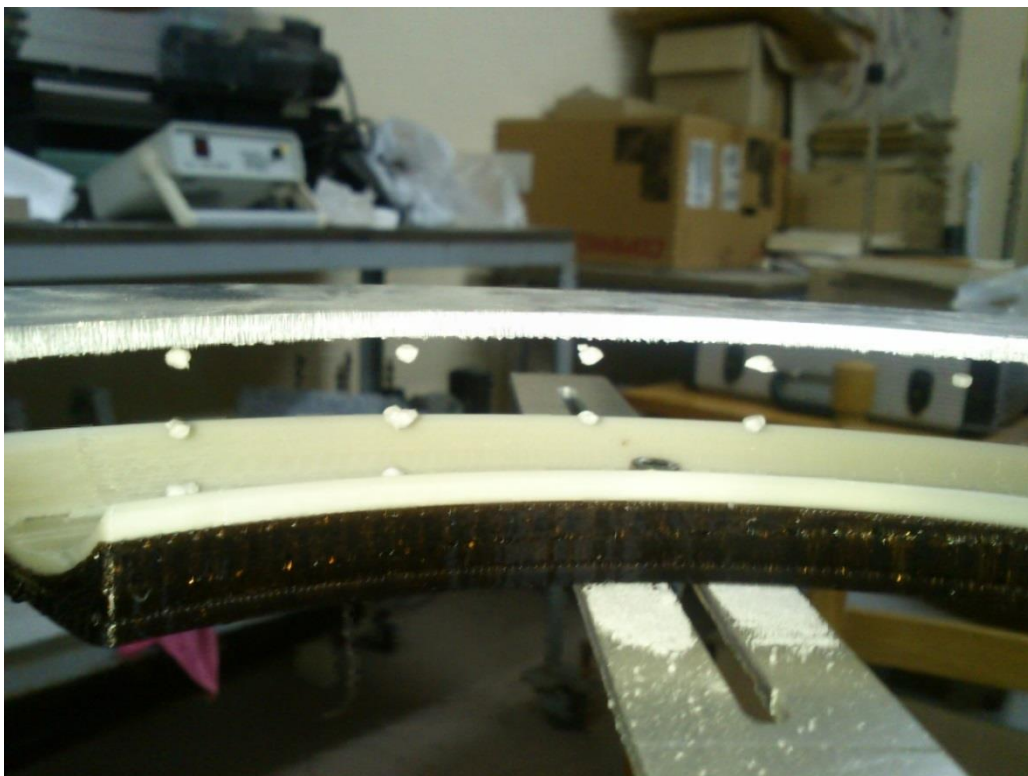Figure 82 – Levitated particles at a one-eighth section

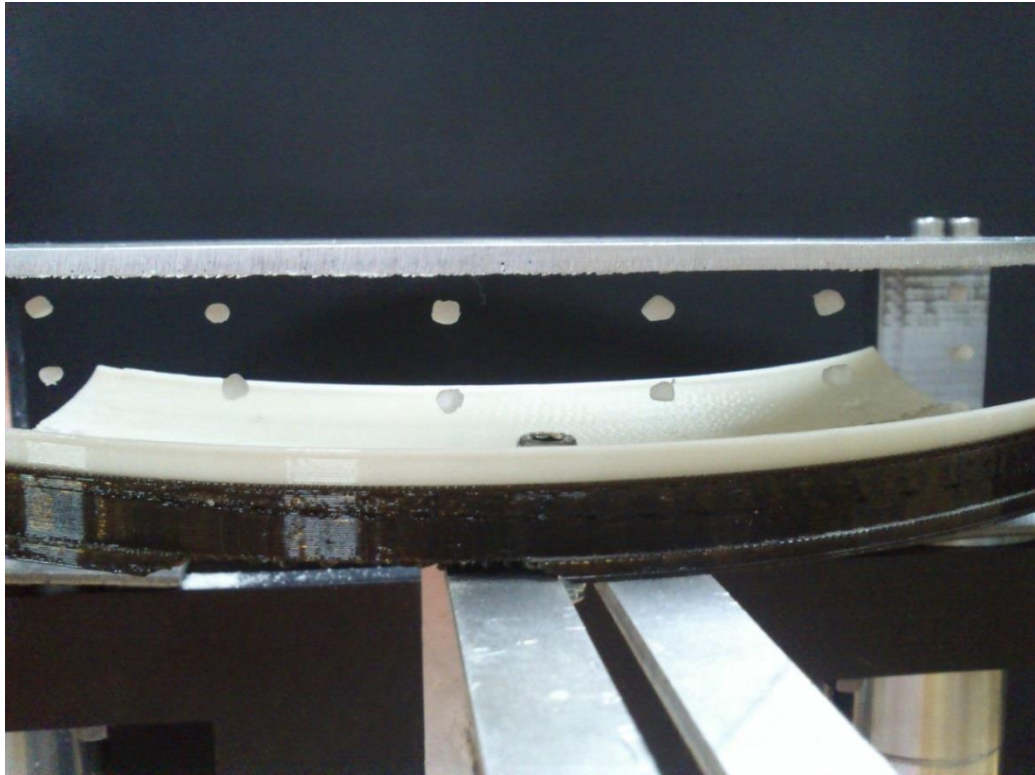Figure 83 – Wider view of the levitation
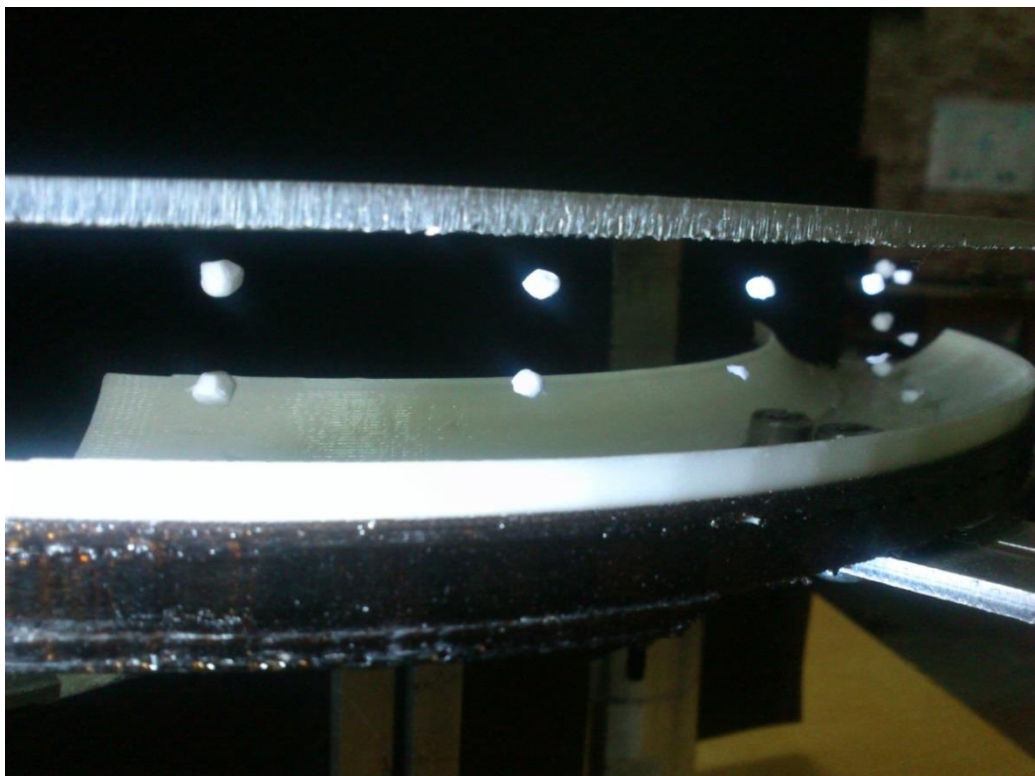
Figure 84 – Levitated view of the particles

Figure 85 – Levitated view of the particles

In the figures it is seen that the screws affect the sound field but do not cancel levitation. Some nodes are seen to be less stable than others. In general, the levitation of polystyrene particles are successfully performed.

Several other materials such as water droplets and spheres of *ABS Plus* are also tried to be levitated but none of the trials were successful. The reason behind this is that such materials are denser than polystyrene and eventually require stronger sound fields. As the available amplifier in the lab cannot deliver more than $20\ V_{PP}$, it is not possible to levitate denser materials using the same set-up. If a more powerful amplifier were available, stronger levitation forces would be obtained, making it possible to levitate higher-density materials.

During the experiments, the current on the cables are also measured. A current of $0.55\ mA$ is obtained while the set-up is fed with $7.07\ V_{rms}$. These measurements indicate the power consumed by the set-up is $3.89\ mW$.

The set-up consists of 24 possible levitation axes, 3 nodes on each axes. Levitated particles are measured in the METU Central Laboratory and in the experiments a maximum mass of $4.5\ mg$ can be levitated in each node. Considering the set-up has 72 levitation nodes, it is possible to levitate a total of $324\ mg$ in this set-up.

A one-quarter section of the reflector is used to represent the whole set-up. Assuming the set-up has a full scale reflector, the efficiency of the set-up can be calculated. The watts per levitated mass is calculated as $0.012\ W/g$.

CHAPTER 6

SUMMARY AND CONCLUSIONS

6.1 Summary

In this study, an annular acoustic levitation set-up is designed and built, and levitation experiments are conducted. Simulations carried out by finite element analysis using COMSOL Multiphysics ® software.

The annular plate has been modeled for bending vibrations and several types of modes are obtained. The vibration distributions of each type are extracted, and then simulated as a sound source. The standing wave profiles are evaluated after placing a reflecting surface at a distance away from the source. Simulations have shown that type B mode profiles are the most suitable ones. It should be noted that the maximum vibrations occur near the middle at type B modes. The transducers purchased have a working frequency range of $20 \pm 0.5 \, kHz$, thus the waveguides are designed to perform in that frequency band. The design of the waveguide involves an iterative process as it includes a flange at the middle, change of cross section at the flange and holes at both ends. Following the iterative process the waveguide is designed to have a natural frequency of $20 \, kHz$. The waveguide is excited by the transducers and in turn it excites the annular plate. Connection to the transducer is realized by a $M10$ screw and connection to the plate is realized by $M5$ screws. The assembly of plate and waveguides are also simulated and a shift in natural frequency is observed. In the simulations the transducers are not taken into account and the target type B mode is found at $20406 \, Hz$. Hence, to get a type B mode of vibration, the excitations should be given at $20406 \, Hz$. Once the frequency

of excitation is determined, the design of reflector is started. Studies for the reflector can be conducted by two different methods. The annular plate and the air gap can both be included in acoustics-solid interaction mode or the acceleration distribution can be used to represent the plate in pressure acoustics mode. Both methods are used and evaluated and it is concluded that the latter one can be used as it is more computationally effective. To represent the plate with normal acceleration, acceleration profile on the plate is expressed as a function of spatial coordinates.

A flat reflector is found to be sufficient to obtain a standing wave, but concave reflectors are known to be focusing and amplifying sound. For a specified distance to obtain three nodes in vertical direction, reflectors with different radius of concavity are simulated. The radius that results in the highest pressure without disturbing the standing wave field is selected. Supporting structures are designed and manufactured. The annular plate and waveguides are made from aluminum alloys where the reflector is made from *ABS Plus* plastic. As the vibration distribution is symmetric around the central axis of the plate and the restrictions on size of the 3d printer machine, the reflector is manufactured as a 90° section to represent the set-up.

The harmonic signals are generated using a HP dynamic signal analyzer. The signals are sent into Derritron TA300 power amplifier. Amplified signals excited the transducers and then transducers excited the annular plate.

To sum up, the set-up is designed and manufactured from the very basics. The reflector is manufactured as a one-quarter section and represented the whole set-up well. At the end, small polystyrene particles are successfully levitated but materials with higher densities cannot be levitated due to insufficiency of acoustical power.

6.2 Conclusions

Once the parts are manufactured, the set-up is assembled and tested. The type B mode of the assembled structure is found at $20400 \, Hz$. A shift in that frequency is expected, however, in this case the experiments and the simulations matched well. The main differences between the simulations and the real set-up are listed below:

- In the simulations the waveguides are fixed all around the radius. In the real set-up, they are fixed by supporting structures and the fixture does not cover the whole circumference.
- The simulations did not include the supporting structures and supporting elements such as bolts.
- The defects coming from manufacturing were present in the real set-up.
- There is nonlinearity in the real set-up due to frictional effects.

Considering the differences listed, it is concluded that they compensated for each other and at the end no significant shift is observed.

The reflector is manufactured as a one-quarter section. The vibration distribution is symmetric; therefore a one-quarter section is satisfactory to observe the levitation performance. The reflector is initially planned to be positioned above the plate, but later it is placed below the plate as the gravity shifts the levitation positions lower, resulting in better visualization when the reflector is below. Assembly of the plate and the waveguides were carried according to the initial configuration. Change of the orientation was not necessary and therefore overlooked as the reflector does not intersect with the waveguides. The distance of the reflector was set up to obtain three nodes, and in the one-quarter section, eighteen levitation locations were estimated. The reflector is placed via bolts at the middle and the sound field is affected by their presence. All of the possible nodes are utilized although some of them are weaker than others. Polystyrene particles of several millimeters in diameters (masses ranging from $0.345 \, mg$ to $4.352 \, mg$) are successfully levitated. Some denser material such as plastic or water drops are also tried but none of them could be levitated. This outcome can be attributed to the power limitations on the

amplifier. If the amplifier were able to deliver higher output, stronger sound field would be possible; enabling the levitation of denser material.

The overall conclusions can be summarized:

- The natural frequencies of the plate obtained in computer simulations and observed in experiments are expected not to match. They, however, are close to each other and this is related to all of the differences compensated for each other.
- The reflector is manufactured from ABS Plus plastic. The sound absorption coefficient of the material cannot be obtained anyhow. The reflector served well to emphasize standing waves. Levitation of heavier material could not be performed.
- The reflector is manufactured as a one-quarter section. It satisfactorily represented the whole set-up.
- The reflector is positioned below the plate. It is demonstrated that better visualization is obtained by doing so.
- The amplifier of the set-up is able to deliver $20 \ V_{pp}$ at maximum. If a more-powerful amplifier was available, denser material might be able to be levitated.

6.3 Future Work

The study is the first study of acoustic levitation in Turkey. It can as well be considered as a pilot study to serve basis for future studies.

For future work on this set-up, the following can be proposed:

- A control set-up to measure changes in the air and adjust the distance of the reflector may be built.
- Traveling waves may be excited on the plate to move levitated particles along a track.

- A stronger amplifier may help levitation of higher density materials.
- More efficient transducer-waveguide assemblies are searched for construction.

REFERENCES

Kundt, A. (1866). Ueeber eine neue Art akustischer Staubfiguren und über die Anwendung derselben zur Bestimmung der Shallgeschwindigkeit in festen Körpern und Gasen. *Annalen Der Physik un Chemie*, (4).

Bücks, K., & Müller, H. (1933). Uber einige Beobachtungen an schwingenden Piezoquarzen und ihrem Schallfeld.

Whymark, R. . R. (1975). Acoustic field positioning for containerless processing. *Ultrasonics*, (November), 251–261.

Zhuyou, C., Zhimin, L., & Shuqin, L. (1992). Development of an acoustic levitation reactor. *Powder Tehcnology*, *69*, 125–131.

Hashimoto, Y., Koike, Y., & Ueha, S. (1996). Near-field acoustic levitation of planar specimens using flexural vibration. *The Journal of the Acoustical Society of America*, *100*(4), 2057.

Hashimoto, Y. (1998). Transporting objects without contact using flexural traveling waves. *The Journal of the Acoustical Society of America*, *103*(6), 3230.

Hu, J., Nakamura, K., & Ueha, S. (1999). A noncontact ultrasonic motor with the rotor levitated by axial acoustic viscous force. *Electronics and Communications in Japan*, *82*(10).

Loh, B., & Ro, P. I. (2000). Ultrasonic Progressive Waves Generated by Two-Mode Excitation. *ieee transactions on ultrasonics, ferroelectrics, and frequency control*, *47*(4), 994–999.

Matsuo, E., Koike, Y., Nakamura, K., Ueha, S., & Hashimoto, Y. (2000). Holding characteristics of planar objects suspended by near-field acoustic levitation. *Ultrasonics*, *38*(1-8), 60–3.

Kaduchak, G., Sinha, D. N., & Lizon, D. C. (2002). Novel cylindrical, air-coupled acoustic levitation/concentration devices. *Review of Scientific Instruments*, *73*(3), 1332.

Chang, K.-T. (2004). A novel ultrasonic clutch using near-field acoustic levitation. *Ultrasonics*, *43*(1), 49–55.

Kozuka, T., Yasui, K., Tuziuti, T., Towata, A., & Aist, Y. I. (2006). non-contact acoustic manipulation in air. *Proc. Symp. Ultrason. Electron.*, *27*, 509–510.

Ide, T., Friend, J., Nakamura, K., & Ueha, S. (2007). A non-contact linear bearing and actuator via ultrasonic levitation. *Sensors and Actuators A: Physical*, *135*(2), 740–747.

Field, C. R., & Scheeline, A. (2007). Design and implementation of an efficient acoustically levitated drop reactor for in stillo measurements. *The Review of scientific instruments*, *78*(12).

Zhao, S., & Wallaschek, J. (2009). A standing wave acoustic levitation system for large planar objects. *Archive of Applied Mechanics*, *81*(2), 123–139.

Ito, Y., Koyama, D., & Nakamura, K. (2010). High-speed noncontact ultrasonic transport of small objects using acoustic traveling wave field. *Acoustical Science and Technology*, *31*(6), 420–422.

Koyama, D., & Nakamura, K. (2010). Noncontact ultrasonic transportation of small objects in a circular trajectory in air by flexural vibrations of a circular disc. *IEEE transactions on ultrasonics, ferroelectrics, and frequency control*, *57*(6), 1434–1442.

Koyama, D., & Nakamura, K. (2010). Noncontact ultrasonic transportation of small objects over long distances in air using a bending vibrator and a reflector. *IEEE transactions on ultrasonics, ferroelectrics, and frequency control*, *57*(5), 1152–1159.

Demore, C., Qiu, Y., Cochran, S., Glynne-Jones, P., Ye, C., & Hill, M. (2010). Transducer arrays for ultrasonic particle manipulation. *2010 IEEE International Ultrasonics Symposium*, (c), 412–415.

Courtney, C. R. P., Ong, C.-K., Drinkwater, B. W., Bernassau, a. L., Wilcox, P. D., & Cumming, D. R. S. (2011). Manipulation of particles in two dimensions using phase controllable ultrasonic standing waves. *Proceedings of the Royal Society A: Mathematical, Physical and Engineering Sciences*, *468*(2138), 337–360.

Takasaki, M., Terada, D., Kato, Y., Ishino, Y., & Mizuno, T. (2010). Non-contact ultrasonic support of minute objects. *Physics Procedia*, *3*(1), 1059–1065.

Baer, S., Andrade, M. a B., Esen, C., Adamowski, J. C., Schweiger, G., & Ostendorf, A. (2011). Analysis of the particle stability in a new designed ultrasonic levitation device. *The Review of scientific instruments*, *82*(10).

L.V. King. (1934). On the acoustic radiation pressure on spheres, *Proc. R. Soc. London Ser.* A 147 212–240.

Embleton, T. (1954). Mean force on a sphere in a spherical sound field. I.(Theoretical). *The Journal of the Acoustical Society of America*, *26*(1). 1

Gor'kov, L. P. (1962). On the Forces Acting on a Small Particle in an Acoustical Field in an Ideal Fluid. *Soviet Physics Doklady, Vol. 6, p.773*.

Barmatz, M., & Collas, P. (1985). Acoustic radiation potential on a sphere in plane, cylindrical, and spherical standing wave fields. *The Journal of the Acoustical Society of America*, *77*(3), 928–945.

Hatano, H. (1994). Axisymmetric analysis of a tube-type acoustic levitator by a finite element method. *IEEE transactions on ultrasonics, ferroelectrics, and frequency control*, *41*(5), 772–777.

Xie, W., & Wei, B. (2002). Dependence of acoustic levitation capabilities on geometric parameters. *Physical Review E*, *66*(2).

Nomura, H., Kamakura, T., & Matsuda, K. (2002). Theoretical and experimental examination of near-field acoustic levitation. *The Journal of the Acoustical Society of America*, *111*(4), 1578–1583.

Mitri, F. G. (2005). Acoustic radiation force acting on elastic and viscoelastic spherical shells placed in a plane standing wave field. *Ultrasonics*, *43*(8), 681–691.

Mitri, F. G. (2005). Acoustic radiation force acting on absorbing spherical shells. *Wave Motion*, *43*(1), 12–19.

Wen-Jun, X., & Bing-Bo, W. (2007). Resonance shift of single-axis acoustic levitation. *Chinese Physics Letters*, *135*(1).

Jia, B., Chen, C., & Zhao, C.-S. (2011). Study on Transient Properties of Levitated Object in Near-Field Acoustic Levitation. *Communications in Theoretical Physics*, *56*(6), 1119–1124.

Andrade, M., & Perez, N. (2011). Matrix method for acoustic levitation simulation. *ieee transactions on ultrasonics, ferroelectrics, and frequency control*, *58*(8), 1674–1683.

Cronin, J. T., & Brill, T. B. (1989). Acoustic Levitation as an IR Spectroscopy Sampling Technique. *Applied Spectroscopy*, *43*(2), 253–257.

Tian, Y., Holt, R., & Apfel, R. (1995). A new method for measuring liquid surface tension with acoustic levitation. *Review of scientific instruments*, *66*(5), 3349–3354.

Hawkes, J. J., Barrow, D., Cefai, J., & Coakley, W. T. (1998). A laminar flow expansion chamber facilitating downstream manipulation of particles concentrated using an ultrasonic standing wave. *Ultrasonics*, *36*(8), 901–903.

Cao, Y., Xie, W., Sun, J., Wei, B., & Lin, S. (2002). Preparation of epoxy blends with nanoparticles by acoustic levitation technique. *Journal of Applied Polymer Science*, *86*(1), 84–89.

Lü, Y. J., & Wei, B. (2006). Supercooling of aqueous NaCl and KCl solutions under acoustic levitation. *The Journal of chemical physics*, *125*(14).

Xie, W. J., Cao, C. D., Lü, Y. J., Hong, Z. Y., & Wei, B. (2006). Acoustic method for levitation of small living animals. *Applied Physics Letters*, *89*(21).

Leiterer, J., Grabolle, M., Rurack, K., Resch-Genger, U., Ziegler, J., Nann, T., & Panne, U. (2008). Acoustically levitated droplets: a contactless sampling method for fluorescence studies. *Annals of the New York Academy of Sciences*, *1130*, 78–84.

Dou, J., Zhang, Q., & Ji, Z. (2012). Research of Silica Particles Dispersion in Polymer Matrix Under Acoustic Levitation. *Journal of Dispersion Science and Technology*, *33*(8), 1134–1138.
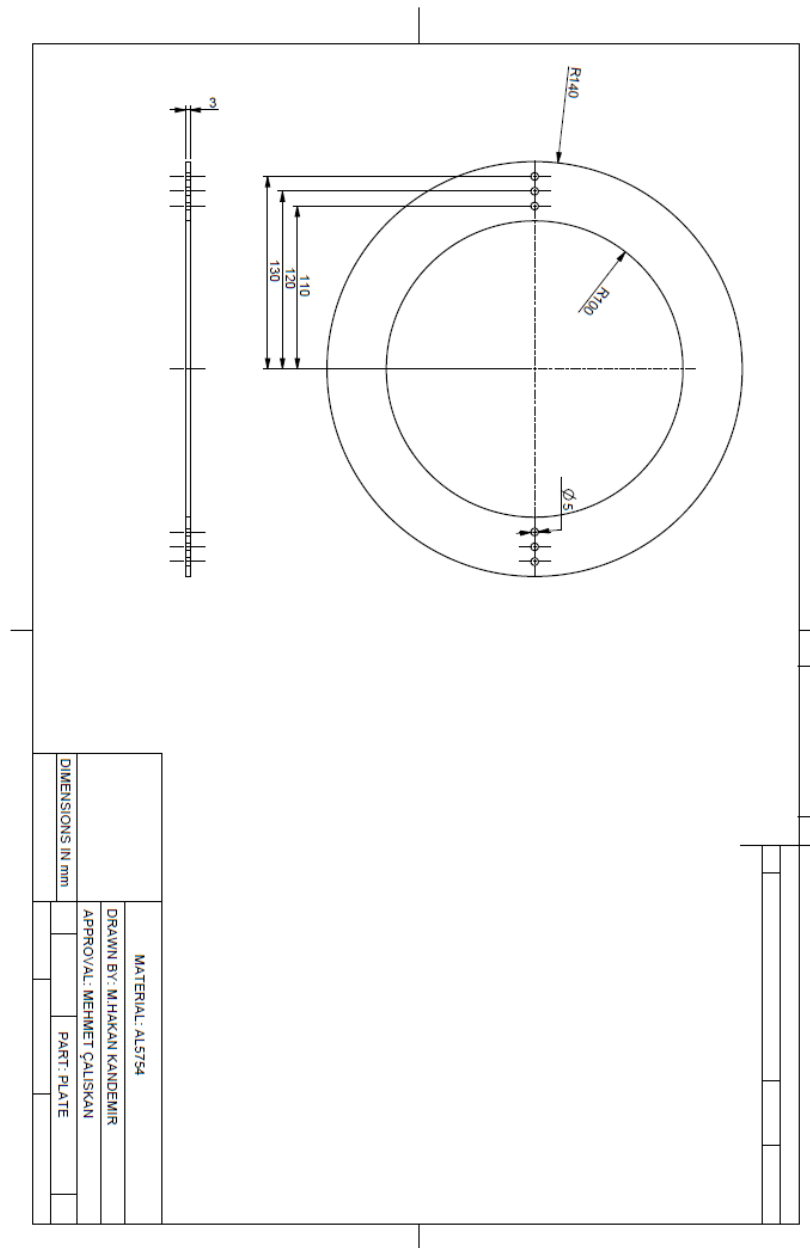
DRAWING OF THE PLATE

Figure 86 – Technical drawing of the plate
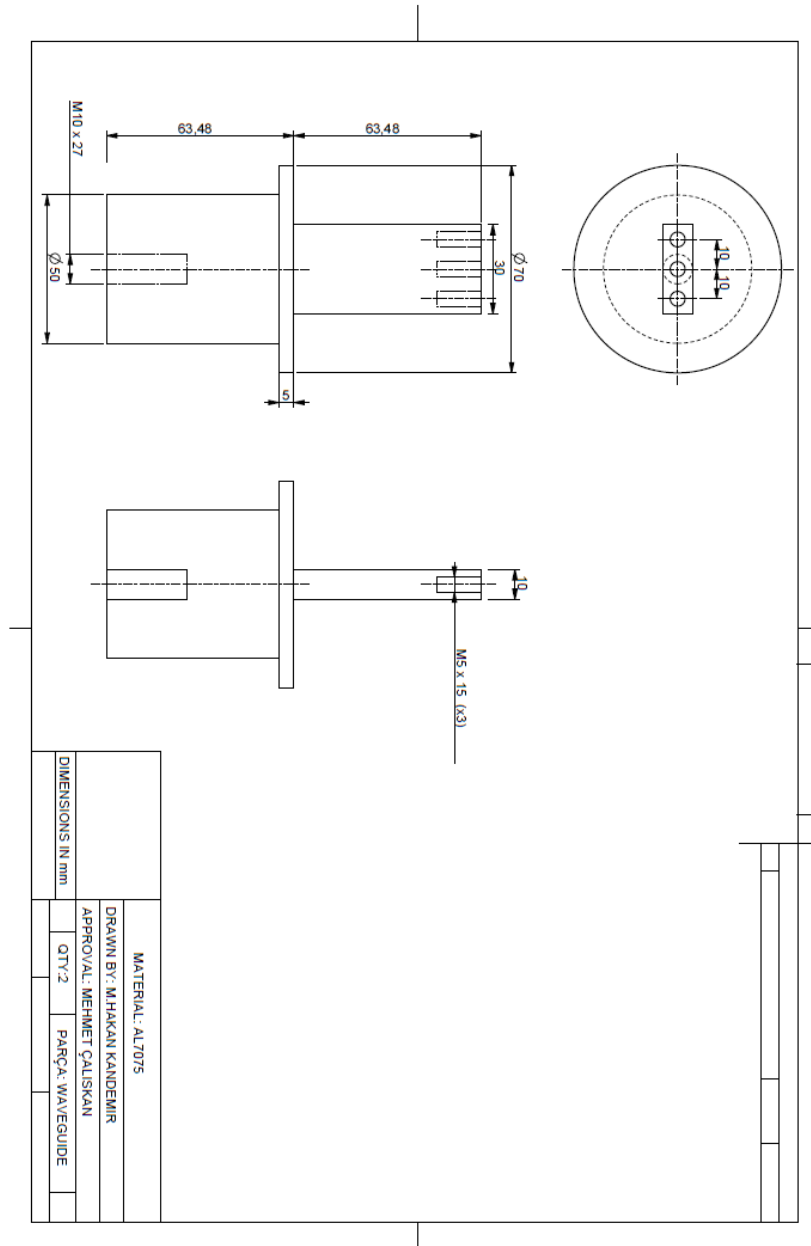
APPENDIX B

DRAWING OF THE WAVEGUIDE

Figure 87 – Technical drawing of the waveguide

APPENDIX C

DATASHEET OF THE TRANSDUCER

Type	Weight (g)	Length (mm)	Maximal-Φ /ceramic-Φ (mm)	Joint Bolt (mm)	Frequency (Fs±0.5 kHz)	Impedance min. (Ω)	Capacitance (Ct±10% pF)	Input power (W)	Front mass
MPI-5050F-20L	984	124	50/50	M20X40	20	10	15500	1200	Metal Al7075
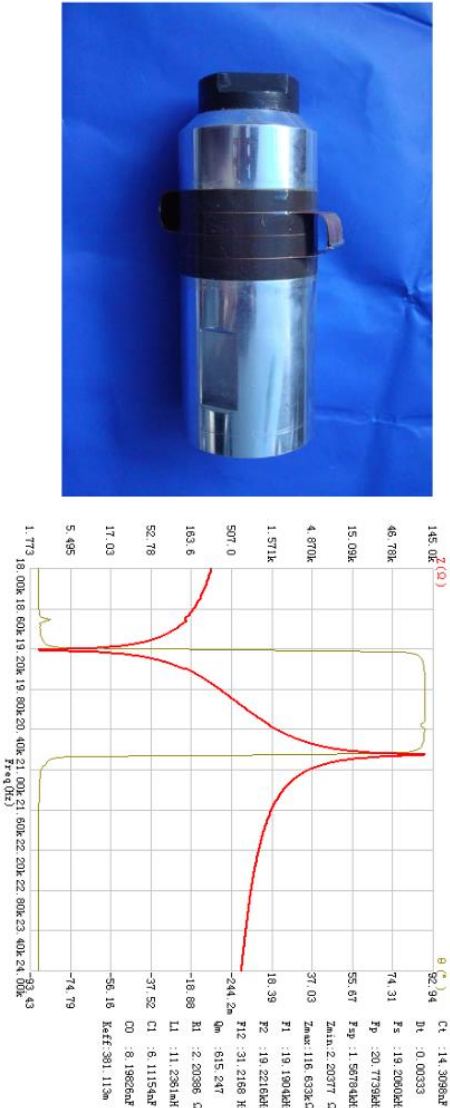
Figure 88 – Datasheet of the transducers

APPENDIX D
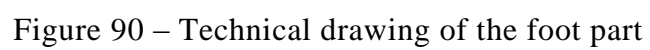
DRAWING OF THE REFLECTOR
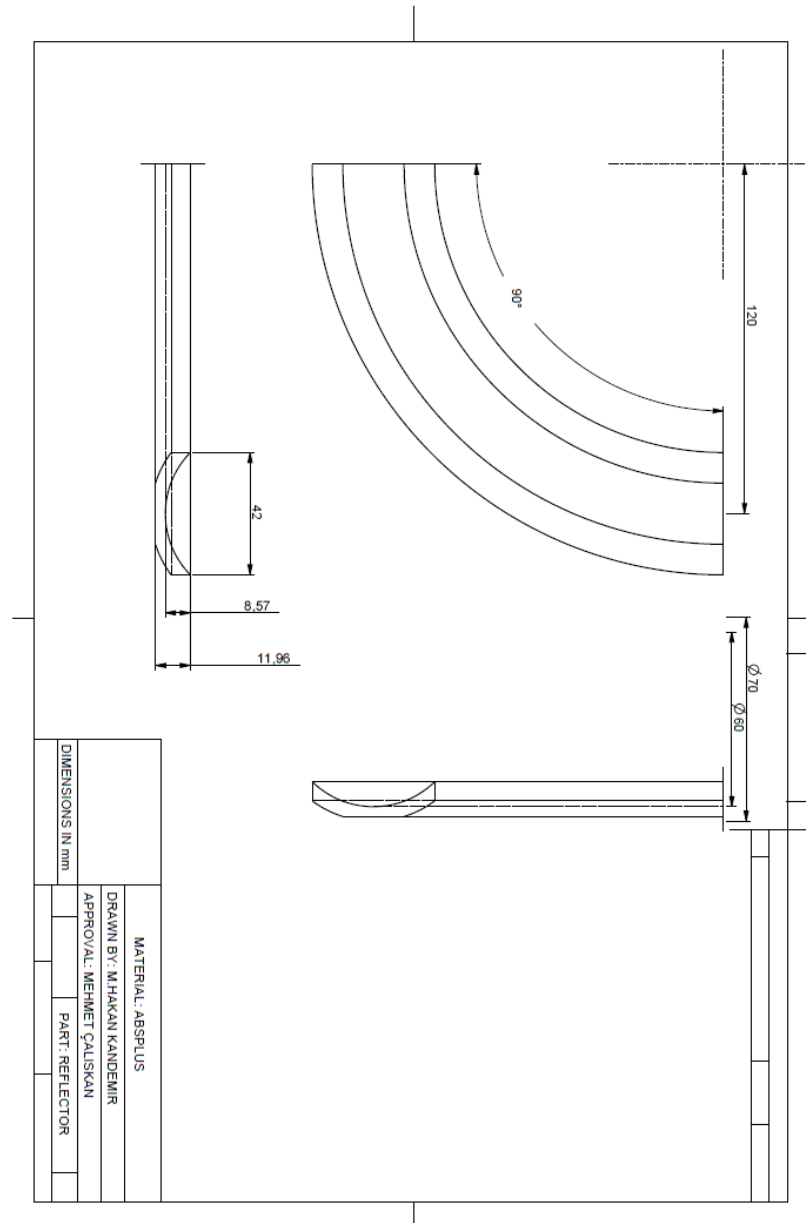
Figure 89 – Technical drawing of the reflector

APPENDIX E

DRAWINGS OF THE SUPPORTING STRUCTURES

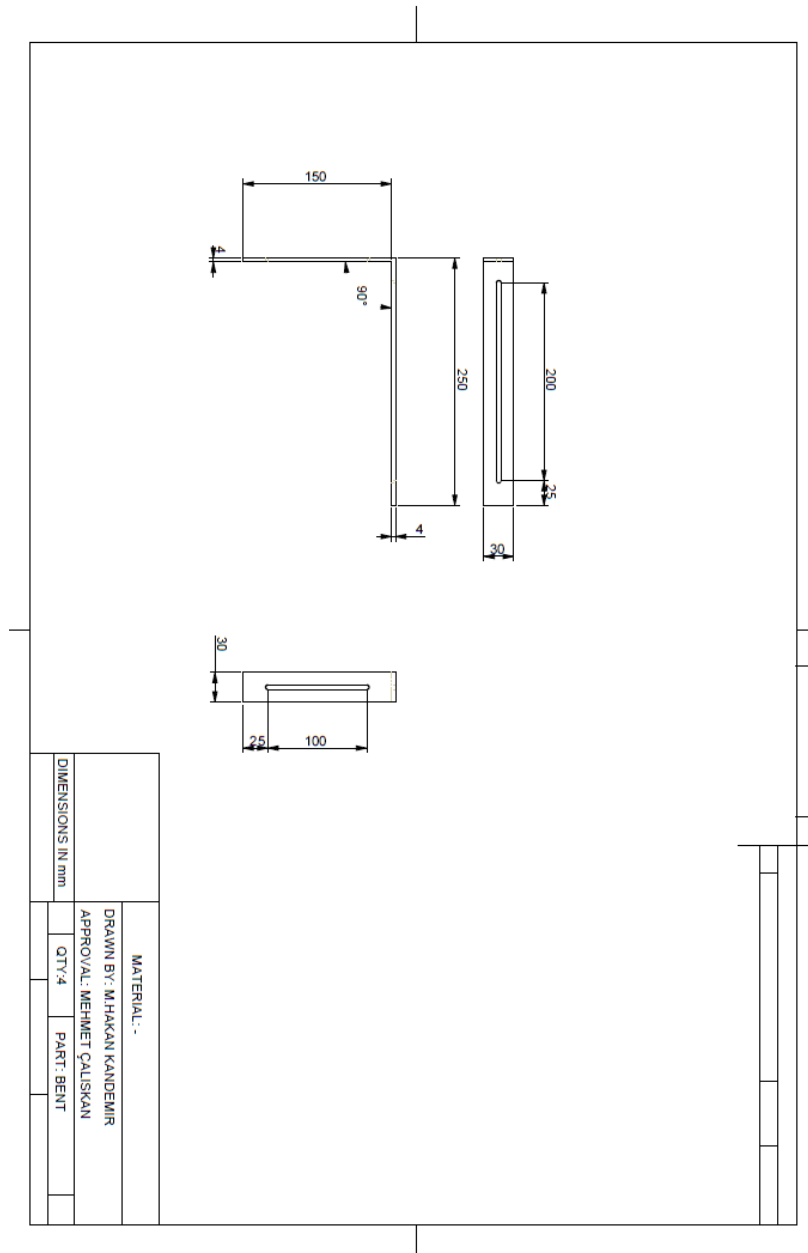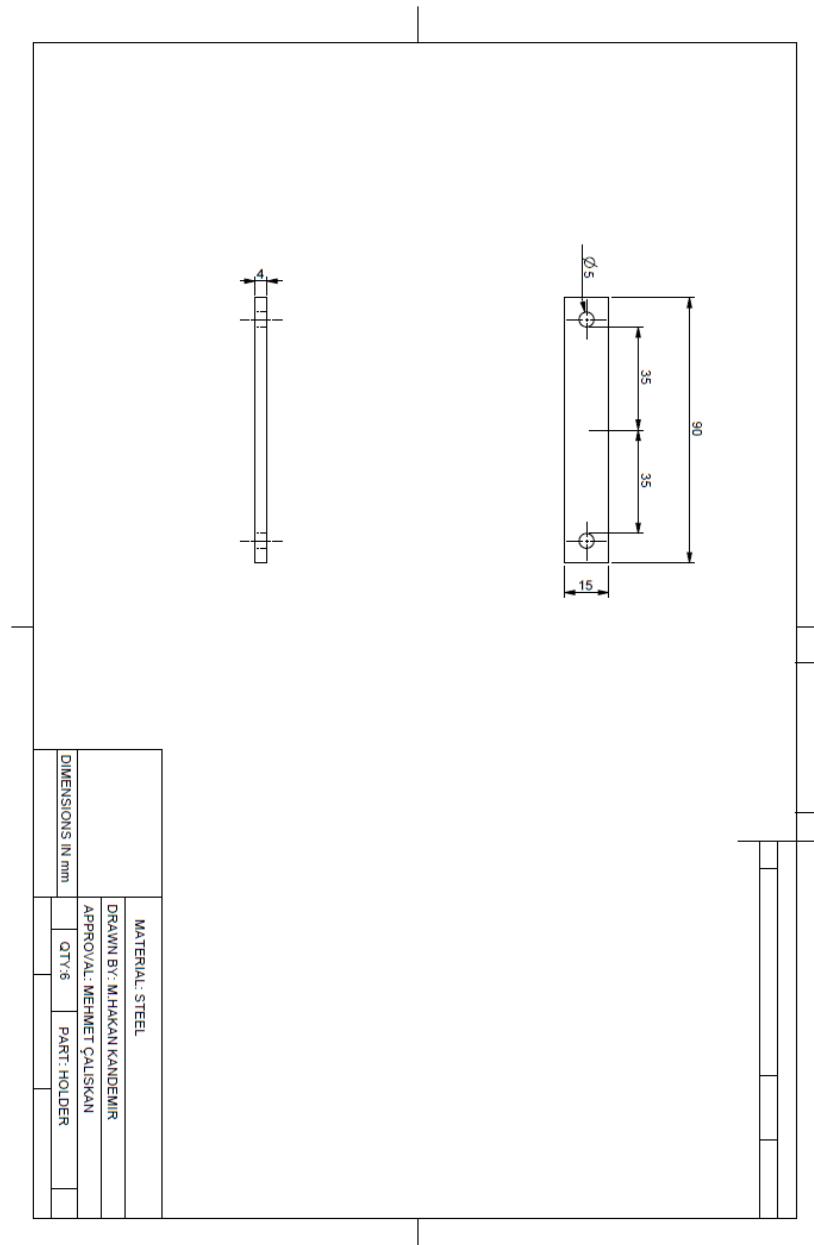Figure 90 – Technical drawing of the foot part

Figure 91 – Technical drawing of the bent part

Figure 92 – Technical drawing of the holding part